中国科学院大学
University of Chinese Academy of Sciences

博士学位论文

光学与中红外波段宁静太阳磁场诊断

作者姓名：MOHAMED SEDIK ABDULLAH AMIN

指导教师：邓元勇 研究员

白先勇 副研究员

学位类别：理学博士

学科专业：天体物理

培养单位：中国科学院国家天文台

2025 年 6 月

Diagnosis of magnetic field of Quiet Sun in optical and mid-infrared wavelength

A dissertation submitted to

University of Chinese Academy of Sciences

in partial fulfillment of the requirement

for the degree of

Doctor of Philosophy

in Astrophysics

By

MOHAMED SEDIK ABDULLAH AMIN

Supervisor: Prof. Yuanyong Deng

Dr. Xianyong Bai

National Astronomical observatories, Chinese Academy of Sciences

June, 2025

Statement of Originality

I declare that this dissertation is the result of my independent research under the instruction of my supervisor. To the best of my knowledge, this thesis/dissertation does not contain any research results that have been previously published or written by other individuals or groups, except for the citations. Other individuals and groups who have made contributions to the research have been mentioned or acknowledged in this dissertation.

Signature:

Date:

Authorization statement for thesis use

I understand and abide by the regulations of the Chinese Academy of Sciences regarding the preservation and use of the dissertation, i.e., the Chinese Academy of Sciences has the right to preserve copies of student dissertation, to allow the dissertation to be consulted, to publish the dissertation all or in part in accordance with the principles of openness in academic research and protection of intellectual property rights, and to preserve and compile the dissertation by photocopying, reprinting in a reduced format, or other means of reproduction. This statement shall apply to classified and delayed dissertation after the declassification or delay period.

Signature of the author: Signature of the supervisor:

Date: Date:

摘 要

宁静太阳占据了太阳表面的大部分区域，在全球性太阳磁活动中扮演着关键却常被忽视的角色。宁静区磁场可分为网络磁场（以强磁场持续存在为特征）和网络内磁场（以弱磁场短寿命磁元为特征）两类。网络磁场构成了太阳表面最大对流结构——超米粒组织的边界，而内网络磁场则填充超米粒的内部空间。

我们利用日本日出卫星 (Hinode) 上搭载的光谱偏振仪（SP）获得的日面中心附近可见光波段高分辨率数据，研究了宁静太阳网络内磁场的性质。通过基于响应函数的 Stokes 反演法（SIR 程序），采用物理参数随深度变化的大气模型，对 SP 数据进行了反演。为降低噪声影响，本文仅分析了 Stokes Q/U 信号大于 4.5 倍噪声的像素点。反演结果表明：网络区内磁场的强度主要表现为百高斯量级，磁倾角呈准各向同性分布。磁场强度随高度递减，上层以水平场为主。中层光球磁场强度和倾角分布与 Milne-Eddington 反演结果一致。在光学深度 $\log\tau = -1.0$ 处，横向和纵向磁通密度分别为 66 Mx cm^{-2} 和 13 Mx cm^{-2}。横向与纵向磁场分量比值随深度变化，深层约为 2.7，上层增加到 5.1。上层光球平均磁场强度超过 100 高斯，与汉勒效应研究相符。我们描述了不同光学深度下视线速度的概率分布函数，显示深层以上升流（$V_{LOS} = 1.2$ km s^{-1}）为主，上层降为 0.6 km s^{-1}。

中红外谱线具有磁场灵敏度更高的特点，当前新建和在研的地基大太阳望远镜都将中红外磁场测量设备作为焦面终端之一。Mg I 12μm 双线（12.22/12.32μm）作为发射线对，其线心形成于温度极小区，磁场灵敏度最高，是研究太阳磁场的理想探针。我们基于三维磁流体力学模型 Birforst，利用 Rybicki-Hummer（RH）代码进行了非局部热动平衡（NLTE）下 Mg I 12.32μm 谱线的 Stokes 轮廓，研究了不同空间分辨率下宁静区磁场与偏振光谱关系。计算表明 Mg I 12.32μm 谱线平均形成高度约 450 km，不同太阳特征的形成高度存在差异。对于弱磁场（< 300 G），基于 Stokes 偏振光谱的波长积分法，采用线性定标能有效标定纵向和横向磁场分量。对于网络磁场区域，在模拟中 48km（0.06″）网格分辨率下，Stokes I 轮廓显示出清晰的塞曼三重分裂。考虑不同口径望远镜的点扩散函数后，Stokes I 光谱轮廓也出现变化，模拟结果表明，如果通过直接分裂的方法观测三分裂 Stokes I 光谱，观测数据的空间分辨率至少需要 0.97″（对应 3.2 米望远镜在该波段的衍射极限）。通过模拟不同空间分辨率下的观测轮廓，为未来大口径太阳望

远镜利用 Mg I 12.32 μm 开展宁静区磁场观测设计提供了参考。

鉴于弱场近似局限性，Stokes 光谱反演方法对磁场定标精度更高、使用日面特征更多。我们也利用模拟数据检验了利用非局部热动平衡 STiC 反演代码和 Mg I 12.32 μm 谱线获取大气参数的能力。结果表明，当偏振灵敏度优于 0.1% 时 (连续谱强度信噪比大于 1000)，STiC 反演方法可以有效确定宁静区不同特征的磁场强度。相关研究对用于太阳磁场精确测量的中红外观测系统 (AIMS) 的活动区或宁静区磁场反演具有重要意义。

关键词：磁场，太阳大气，偏振，辐射传输

Abstract

The quiet Sun, which covers most of the solar surface, is thought to hold a significant amount of solar magnetic flux, playing a crucial yet often overlooked role in global solar magnetism. The quiet Sun can be divided into network areas, where strong magnetic fields persist, and internetwork (IN) regions, characterized by weaker and shorter-lived magnetic elements. Network areas define the boundaries of supergranular cells, the largest convective features on the solar surface, while internetwork regions fill the spaces within these cells.

We examined the magnetism of the IN utilizing high spatial resolution data obtained by the spectropolarimeter (SP) of the Solar Optical Telescope on the Hinode satellite near the solar disk center. The SP data were inverted utilizing the Stokes Inversion based on Response functions (SIR) inversion method, employing a single-component atmosphere with depth-dependent characteristics in the solar photosphere, while presuming gradients in physical parameters along the line of sight (LOS). To mitigate the influence of noise, only pixels exhibiting Stokes U and/or Q signals over 4.5 times the noise threshold are taken into account.

The inversion results indicate that the magnetic field of the IN mostly exhibits hectogauss field strength, with a quasi-isotropic inclination distribution at the solar surface. The field intensity diminishes with altitude and becomes primarily horizontal in the upper strata. In the mid photosphere, the distributions of magnetic field strength and inclination align with those obtained from Milne–Eddington (ME) inversion. The average transverse and longitudinal flux densities are 66 Mx cm^{-2} and 13 Mx cm^{-2} at log $\tau = -1.0$, respectively. We also examined the ratio of the transverse to longitudinal components in the IN region as a function of photospheric depth, discovering that the ratio is approximately 2.7 in the deeper layer, rising to 5.1 in the upper layer. The average magnetic field strength exceeds 100 G in the upper photosphere, aligning with findings derived from the Hanle effect. We described the LOS velocity probability distribution function for IN at various optical depths, where the distribution is mostly linked to upflow velocities of V_{LOS} =1.2 and 0.6 km s^{-1} in the deeper and higher layers,

respectively. Furthermore, a dependable inversion analysis is evident from the comparison of the observed and calculated area asymmetries in both Fe I lines.

We subsequently analyzed the properties of the Mg I 12.32 μm line as observed in the quiet Sun network. The Mg I 12 μm lines, 12.22 and 12.32 μm, constitute a pair of emission lines, with their line cores originating at the temperature minimum area. These lines demonstrate the greatest ratio of Zeeman to Doppler broadening in the infrared solar spectrum, rendering them essential for precise examination of the solar magnetic field. We synthesized the Mg I 12.32 μm Stokes profiles from a 3D magnetohydrodynamic (MHD) model and examined the efficacy of several approaches for obtaining the magnetic field. Simulations of observational profiles at several spatial resolutions were conducted, aiding in the design of future large-aperture solar observatories. We conducted non-local thermal equilibrium (NLTE) calculations for the Stokes profiles of the Mg I 12.32 μm line utilizing the Rybicki–Hummer (RH) code.

Our calculations indicated that the average formation height of the Mg I 12.32 μm line is around 450 km. The diverse solar features exhibit varying formation heights. The wavelength-integrated method is demonstrated to be effective in calibrating the integrated Stokes profiles to derive the longitudinal (B_l) and horizontal (B_H) field components for weak magnetic fields, with B_l being below 300 G. The weak field approximation (WFA) is only valid for calculating magnetic fields with $B_l \leq$150 G. The Stokes I profiles distinctly exhibit Zeeman triple splitting surrounding the magnetic flux concentration at a grid resolution of 48 km. We concluded that a resolution of $0.97''$, corresponding to the diffraction limit of a 3.2 m diameter telescope, was essential to observe the Zeeman splitting in the simulated snapshot.

Due to the limitation of WFA for determining the magnetic field, we examine the capability of non-local thermodynamic equilibrium (non-LTE) STiC inversion code to retrieving the atmospheric parameters. Our results illustrated that the inversion can accurately determine the magnetic field components for observations with noise levels up to 1×10^{-3} relative to continuum intensity. Our analysis is important for analyzing data from the Accurate Infrared Magnetic Field Measurements of the Sun (AIMS) telescope and for the development of future solar infrared telescopes.

Key Words: Magnetic fields, Solar atmosphere, Polarization, Radiative transfer

Contents

List of Figures

Figure 3-12 Top: The PDFs of asymmetries for the observed (black) and inverted (red) Stokes V spectra of Fe I 6302.5 Å (left) and Fe I 6301.5 Å (right) lines. the vertical dotted lines indicate the mean asymmetry for both Fe I lines. Bottom: Scatter plots of the observed and inverted asymmetries resulting for both Fe I lines. The bottom panel shows the linear fits (blue line) between the observed and inverted asymmetries in both Fe I lines. ·· 50

Figure 4-1 Horizontal cross sections of MHD simulation at two different geometrical heights z=0 km (left) and z=450 km (right). From top to bottom: Temperature (T), longitudinal (B_l) and horizontal (B_H) components of the magnetic field. Brown dotted lines indicate a zone that will be examined further in section 4.4. ·· 56

Figure 4-2 Maps of vertical slices Showing Temperature (T; Left), Longitudinal Field (B_l; middle), and Horizontal Field (B_H; right) Profiles, Corresponding to the dashed brown line in Figure 4-1. magenta lines indicate the heights of optical depth $\tau = 1$ for the core of the Mg I 12.32 μm line. The vertical lines represent the four atmospheric columns subjected to detailed analysis. ··· 58

Figure 4-3 Synthetic Stokes I profiles (first column) and Stokes V profiles (second column), along with the vertical distribution of magnetic field strength (B; third column) and temperature (T; fourth column) for the four vertical atmospheric columns. The line style at the top of each panel represents the respective atmosphere, as seen in Figure 4-2. The vertical dotted line in the third and fourth columns indicates the formation height at optical depth $\tau = 1$, as marked by magneta line in Figure 4-2. ····················· 59

Figure 4-4 Maps of integrated intensity (top), MCPD (middle), and MLPD (bottom) for the synthetic profiles of the Mg I 12.32 μm line. ················ 62

Figure 4-5 Scatter plots of MCPD (left panel) and MLPD (right panel) as a function of the B_l and B_H of the simulation model, respectively, at a height of 450 km. ·· 63

Figure 4-6 Maps of B_l as derived from the WFA method (left panel) and MHD simulation at a height of 450 km (right panel). Green regions mark the excluded pixels whose Stokes I profiles exhibit Zeeman splitting. ········ 64

Figure 4-7 B_l as inferred from the WFA versus the actual values in the MHD simulation model. Vertical dotted blue lines demarcate the region of validity of the WFA. ···································· 65

Figure 4-8 Maps of MCPD (first row) and MLPD (second row) for the degraded profiles of the Mg I 12.32 μm line at spatial resolutions of $0''.39$, $0''.78$, and $3''.1$, respectively, from top to bottom. ································ 67

中国科学院国家天文台 YANG Xiao 2026-04-23 10:28:48

Chapter 1 Introduction

1.1 The Sun

The Sun is a huge ball of intensely hot ionized gas, spanning a diameter of 700,000 kilometers. However, the Sun is classified as a normal star within the middle-lower part of the main sequence, characterized by its spectral type G2. It holds a unique distinction as the only star that can be spatially resolved. Additionally, the Sun serves as a colossal energy source, emitting electromagnetic radiation and undergoing mass ejections, which can be explosive during flares or more continuous and relatively calm as solar wind. It consist of six layers, each one with a different density of plasma. Furthermore, the Sun consists of six distinct layers, each exhibiting varying densities of plasma (see Figure 1-1). The three inner layers, namely the core, the radiative zone, and the convection zone, are responsible for the generation and circulation of sunlight and energy. Conversely, the three outer layers, comprising the photosphere, chromosphere, and corona, are marked by significant and dynamic activity.

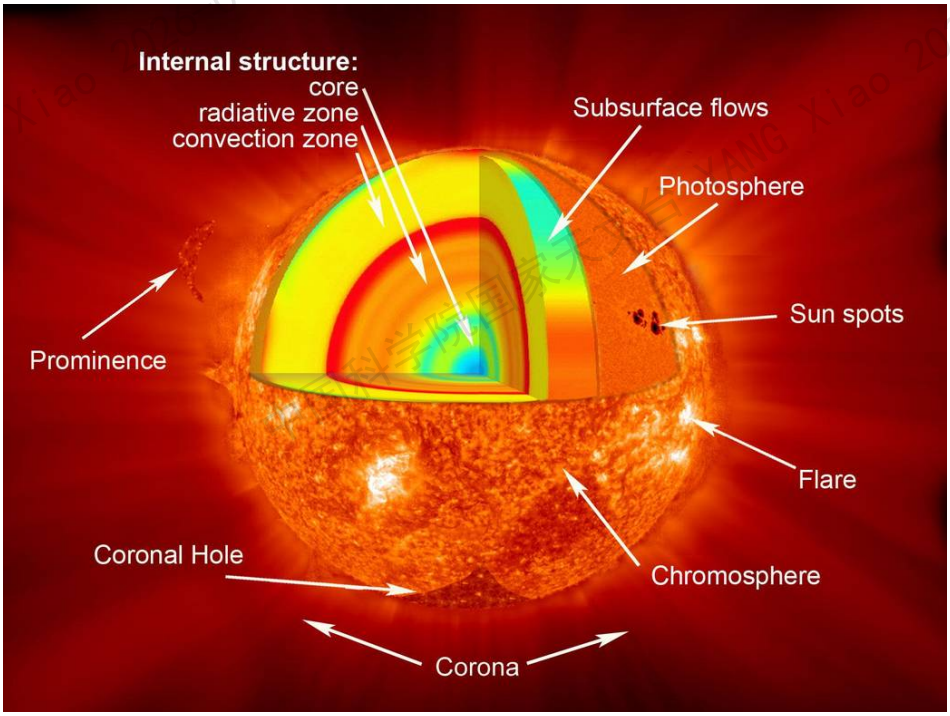

Figure 1-1 A schematic graph for the structure of Sun.

The Sun's core possesses an extremely high temperature that facilitates nuclear fusion. The energy released during this fusion process creates an outward pressure, which is counterbalanced by gravitational forces. Although the Sun is primarily composed of Hydrogen (74%) and Helium (25%), it contains trace amounts of nearly all naturally occurring elements, each with varying abundances (Asplund et al., 2009). As a result of nuclear processes, the Sun emits a continuous black-body spectrum of radiation. These emitted photons serve as fundamental diagnostic tools for investigating and comprehending the physics of processes occurring in the solar atmosphere.

The photons originating from the Sun's core undergo a stochastic random walk as they traverse the radiative zone, characterized by an exceptionally small mean free path. This occurs due to the continuous absorption and reemission of photons by atomic species within the densely packed plasma. The gravitational force acting on a unit of fully ionized plasma diminishes radially outward from the core until reaching the boundary between the radiative and convective zones. At this boundary, the inward gravitational force is balanced by outward pressure forces, establishing a state of hydrostatic equilibrium. Within the boundary between the radiative and convective zones, the temperature drops to a level where atoms can retain their electrons in orbit, leading to convection becoming a more efficient means of energy transport compared to radiative transport. The convective zone is characterized by dominant convective cells, which facilitate the upward movement of hotter material and the downward movement of cooler material through the process of convection.

The Sun's interior is not directly measurable, but by studying the modes of the Sun's vibrations, we are able to gain insight into its internal structure. These measurements play a crucial role in validating theoretical models of the Sun's composition and behavior. On the other hand, The light we observe from the Sun originates from the solar atmosphere. The convective zone is opaque due to the fact that the photon mean free path is less than the distance the photon is required to travel to escape.

The photosphere, which can be described as the surface of the Sun, acts as a boundary where visible light is able to escape from the Sun's interior. Extending from the solar surface to approximately 500 km in height, this region emits radiation that conforms to the Planck function at all wavelengths. As we move away from the Sun's core, the temperature of the plasma decreases, enabling us to determine the number density

of specific atomic species and the populations of atomic energy levels through the solution of the Saha and Boltzmann equations. Upon careful observation, the photosphere reveals distinct prominent features such as granulation, sunspots, and faculae.

The granulation is observed as a cellular pattern that envelops the entire surface of the Sun, as depicted in Figure 1-2. Numerous bright structures, referred to as granules, are surrounded by dark intergranular lanes. Bright granules are composed of hot plasma parcels that move upwards, while the darker intergranules contain cooled plasma moving downwards. These characteristics arise as a result of convective motions occurring just beneath the solar surface. The granulation pattern undergoes continuous evolution, with old granules being displaced by newly emerging ones. On average, the lifetime of a granule is approximately 6 minutes.

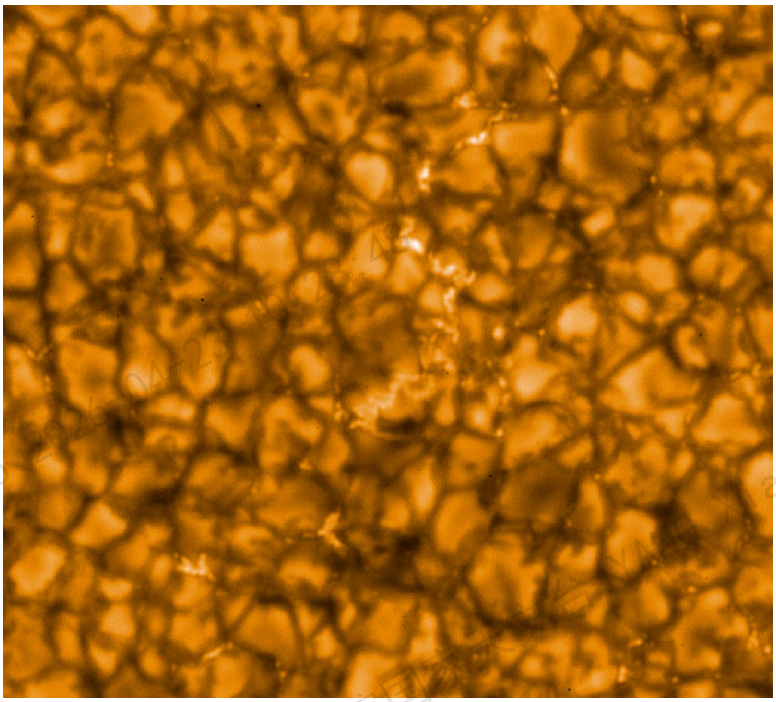

Figure 1-2 The granulation as observed by the satellite Hinode.

Sunspots are observable as dark spots on the surface of the Sun, as illustrated in Figure 1-3. These structures are characterized by a significant drop in temperature within their dark centers, reaching approximately 3700 K, in contrast to the surrounding photosphere, which maintains a temperature of about 5700 K. Sunspots can persist in the photosphere for a duration ranging from several days to a few months. Additionally, their size varies throughout their existence, with a range spanning from 1500 to 50000 km. The formation of sunspots is attributed to the presence of an intense magnetic

field and usually present in groups. Sunspots can be divided into two distinct zones known as the umbra and the penumbra. The umbra corresponds to the central region of the sunspot, characterized by its darkest appearance and the presence of a particularly strong magnetic field, exceeding 2000 G. Surrounding the umbra is the penumbra, which exhibits a brighter appearance and maintains a temperature of approximately 5500 K. The penumbra of a sunspot comprises clusters of both dark and bright filaments. These filaments are associated with a radial flow extending from the umbra towards the outer regions of the sunspot, a phenomenon known as the Evershed effect.

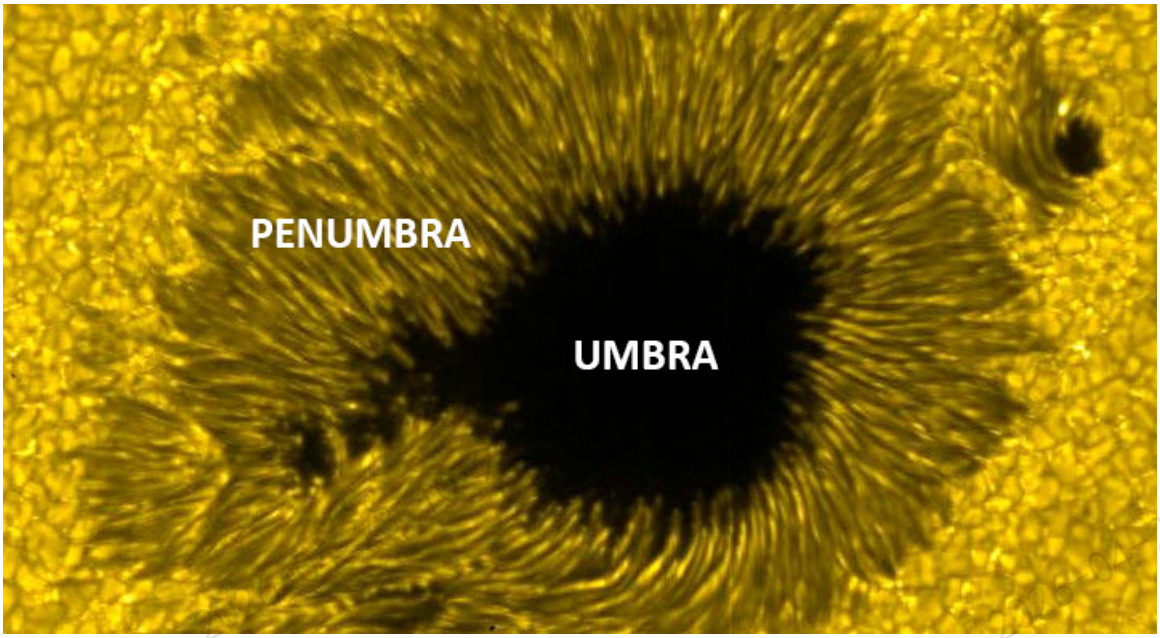

Figure 1-3 The sunspot as observed by the satellite Hinode.

1.2 Quiet Sun magnetism

In the photosphere, the magnetic fields are structured by convection flows, which cause them to be frozen in flux. The non-active regions, also known as the quiet Sun, occupy the majority of the solar surface. Consequently, they may carry a significant amount of the solar magnetic flux (Stenflo, 1982). This suggests that the quiet Sun can play a crucial role in the global solar magnetism, a factor that has not been adequately considered thus far. The convection flow has the ability to concentrate magnetic fields into extremely small magnetic fluxes and higher Reynolds numbers. Therefore, the investigations of quiet Sun magnetism require highly sensitive spectropolarimeteric observations with high spatial resolution.

The quiet Sun can be categorized into two distinct regions: network areas and internetwork regions. In network areas, we observe long-lasting patterns of kilogauss magnetic fields, while in internetwork regions, weaker and smaller-scale magnetic elements are present, with much shorter lifetimes (Zwaan, 1987). The network areas also serve as the boundary of supergranular cells, which are the largest convective patterns on the solar surface (Sheeley, 1967; Stenflo, 1973). The internetwork regions permeate the interior of these supergranular cells. It is important to note that the network areas and internetwork regions are not separate phenomena. The study conducted by Gošić et al. (2014) have provided evidence showing that up to 40% of the internetwork flux eventually becomes a part of the network areas.

Keller et al. (1994) conducted the first visible polarimetric observations of the IN regions. Their findings revealed that the magnetic fields within the IN were below kilogauss, with an upper limit of 500 gauss for the field strength. Subsequent studies on the magnetic fields of the IN have benefited from advancements in solar spectro-polarimetry instruments, leading to a better understanding of the origin of IN magnetism in the quiet Sun. These studies have identified the IN magnetic fields as short-lived, horizontally inclined structures, typically smaller than 1 arcsecond near the center of the solar disk (Lites et al., 1996), and these structures extend to a few arcseconds (De Pontieu, 2002). Nevertheless, a controversy exists regarding the distribution of the magnetic field strength within the IN, primarily due to variations in observational techniques, such as using different spectral lines and employing diverse diagnostic methods. Some studies have reported magnetic field strengths in the range of hundreds of gauss (hG) (Lites et al., 2008; Orozco Suárez et al., 2012a), while others have observed kilogauss field strengths (Socas-Navarro et al., 2002; Stenflo, 2013). Furthermore, studies utilizing the Hanle effect have identified magnetic fields within the range of tens of gauss (Bianda et al., 1999; Trujillo Bueno et al., 2004).

Significant investigations into the intergranular magnetism primarily involved two major approaches. Firstly, analyzing spectropolarimetric data obtained from various spectral regions. Secondly, conducting numerical simulations of magnetic and convective flows using magnetohydrodynamics (MHD). The latter, is able to reproduce the convective flow at the photosphere with weak fields. Notably, simulations of a localized dynamo have provided predictions that turbulent convective flows can concentrate and

consequently amplify magnetic fields within the granulation (Cattaneo, 1999; Rempel, 2014).

Currently, there is no existing meter capable of directly examining the plasma found in the photosphere and providing us with a comprehensive understanding of its physical characteristics. However, we can determine its magnetic properties by interpreting spectropolarimetric measurements. This process involves utilizing diagnostic techniques primarily centered around the radiative transfer equation. Advancements in solar physics and the discovery of new phenomena have consistently relied on our understanding of radiative transfer in stellar atmospheres. Notably, the work of Landi Degl'Innocenti et al. (2004) has emphasized the significance of this knowledge and the development of innovative instrumentation in these breakthroughs.

1.3 Zeeman effect

The Zeeman effect studies the splitting of a spectral line into several components when the source is in presence of a static magnetic field (Zeeman, 1897), as seen in Figure 1-4. The classical explanation of the Zeeman effect is the Lorentz's theory of the electron, assuming that the oscillation of an electron is perturbed in the presence of a magnetic field. The new oscillation can be represented by three independent components, two circular and one linear. The linear component keeps its natural frequency ν_0 (π-component), but the circular components oscillate perpendicular to the direction of propagation with frequencies $\nu_0 + \nu_L$ and $\nu_0 - \nu_L$ (σ-components). ν_0 is the central frequency of the transition and ν_L is the Larmor frequency which defined as:

$$\nu_L = \frac{eB}{4\pi m_e c} \tag{1-1}$$

where e is the electric charge, m_e is the electron mass, c is the velocity of light and B is the magnetic field strength.

The spectral lines result from the absorption and emission of photons when an electron undergoes a transition between two bound levels. When a magnetic field is present, these levels split into multiple sublevels with varying energies. In a classical perspective, an electron in a specific sublevel oscillates at one of the corresponding frequencies. Consequently, when a photon is emitted, it becomes circularly polarized with a

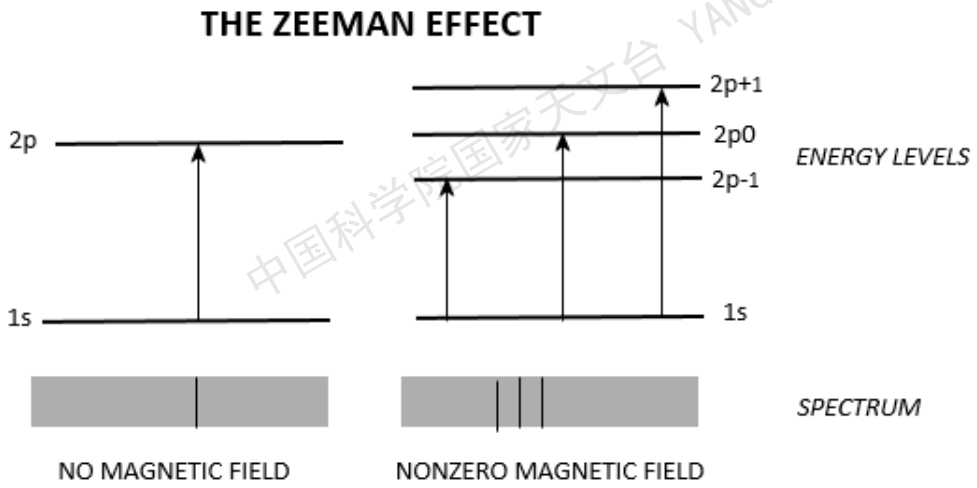

Figure 1-4 Diagram of level splitting in the present of magnetic field

frequency dependent on the energy of the sublevels. This polarization occurs in both clockwise and counterclockwise directions. Additionally, there is a linearly polarized component. This phenomenon is referred to as the normal Zeeman effect. However, some spectral lines exhibit the anomalous Zeeman effect, where, in the presence of a magnetic field, they split into four or more components. The classical theory fails to explain this effect adequately, necessitating a quantum mechanical description to understand the process of atomic absorption in such cases.

In the quantum mechanical description, the magnetic quantum numbers of the upper and lower level (M_u , M_l) takes values of $M = -J, ..., 0, ..., J$. The quantum number J describes the total angular momentum of a state, which couples the spin angular momentum (S) and the orbital angular momentum (L) of a state. the σ-components are transitions with $\Delta M = \pm 1$ and for the π-component holds $\Delta M = 0$. The splitting of each sublevel is defined as

$$\nu_M = gM\nu_L \tag{1-2}$$

For a given J value a state can split $2J + 1$ components (see Figure 1-5). Within L-S coupling, the Landé factor (g) is computed as:

$$g = \frac{3}{2} + \frac{S(S+1)-L(L+1)}{2J(J+1)} \tag{1-3}$$

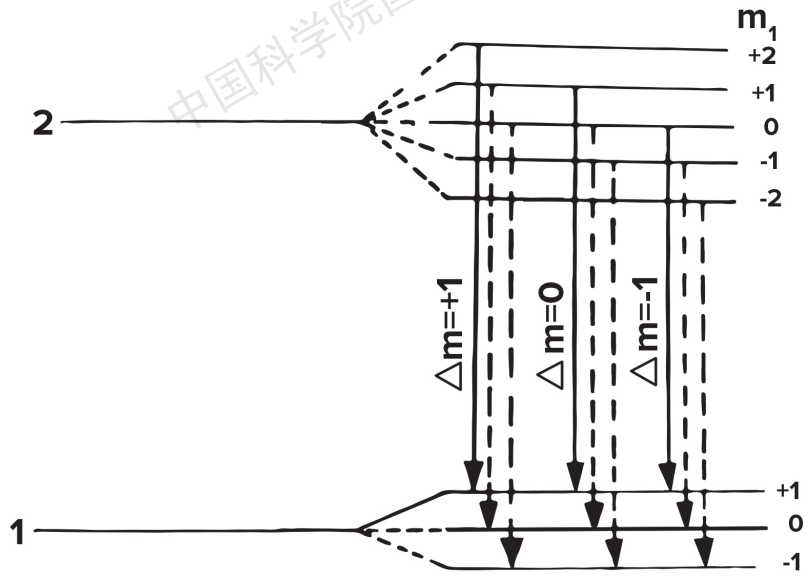

Figure 1-5 Schematic diagram for the Zeeman splitting which show the number of splitting determined by $2J + 1$**.**

From Equations 1-1 and 1-2, the displacement ($\Delta\lambda_B$) of the σ-components from the π-component can be expressed by

$$\Delta\lambda_B = \frac{e\lambda_o^2}{4\pi m_e c^2} B(g_l M_l - g_u M_u) \tag{1-4}$$

where λ_o is the central wavelength of the transition without a magnetic field. The observation of the fine structure of the Zeeman effect is challenging due to various factors that broaden the spectral lines. These factors include thermal motions of the atoms, collisions between atoms, and turbulence effects. However, we can redefine the difference between the wavelengths of components π and σ as

$$\Delta\lambda_B = 4.6685 \times 10^{10} g_{eff} \lambda_o^2 B \tag{1-5}$$

The value of the constants, $\Delta\lambda_B$ in mÅ, λ_o in Å, and B in Gauss. g_{eff} is the effective Landé factor, that indicates the sensitivity of a spectral line to the magnetic field and can

be described as

$$g_{eff} = \frac{1}{2}(g_l + g_u) + \frac{1}{4}(g_l - g_u)[J_l(J_l + 1) - J_u(J_u + 1)] \tag{1-6}$$

The Zeeman effect possesses a notable characteristic that renders it particularly valuable for studying small-scale structures on the Sun. It exhibits a distinct polarimetric signature, enhancing its usefulness in analysis. In the longitudinal case, where the line-of-sight aligns with the magnetic field direction, the σ-components of the spectral lines become circularly polarized, while the π-component remains invisible. Conversely, in the transverse case, when observing perpendicular to the magnetic field, all components become visible. During absorption, the π-component is linearly polarized in the direction perpendicular to magnetic field, while the σ-components are linearly polarized parallel to the magnetic field. This polarization behavior provides valuable insights into the nature and orientation of the magnetic field within these structures.

In the case of strong magnetic field, the peaks of the Stokes V profile undergo displacement as described by Equation 1-4. However, for the weaker fields the separation between the peaks remains constant while the amplitude of Stokes V increases. Under these circumstances, it can be observed that the Stokes V profile is primarily determined by the partial derivative of Stokes I, as follow:

$$V(\lambda) = -\Delta\lambda_B \, cos\theta \, \frac{\partial I(\lambda)}{\partial \lambda} \tag{1-7}$$

The parameter θ represent the inclination of the magnetic field with respect to the line-of-sight. It is evident that when this approximation is valid, the Stokes V parameter is directly proportional to the strength of the magnetic field B. Furthermore, a similar approximation can be made for Stokes Q and U, where the Stokes Q parameter is proportional to the square of the magnetic field B^2 (Auer et al., 1977; Jefferies et al., 1989):

$$Q(\lambda) = -\frac{1}{4}(\Delta\lambda_B)^2 \, sin^2\theta \, \frac{\partial^2 I(\lambda)}{\partial \lambda^2} \tag{1-8}$$

1.4 Polarized Light

Based on Maxwell's wave equation and when considering a solution in the form of a plane wave, we can describe light as oscillations of electromagnetic waves. These

oscillations occur in one or more directions, which are perpendicular to the direction in which the light propagates. Moreover, these oscillations can be broken down into two waves that are oriented at right angles to each other within the plane perpendicular to the direction of propagation:

$$E_x(t) = A_x e^{i(\delta_x - \omega t)}$$
$$E_y(t) = A_y e^{i(\delta_y - \omega t)} \tag{1-9}$$

where E_x and E_y represent the electric vector of x and y components, t is time, A_x and A_y are the amplitude of each component, and δ_x and δ_y are the phases of shift of each component. By considering the Poynting vector, the polarization tensor or coherency matrix (C) can be expressed as described by del Toro Iniesta (2003):

$$C = \begin{pmatrix} E_x E_x^* & E_x E_y^* \\ E_y E_x^* & E_y E_y^* \end{pmatrix} \tag{1-10}$$

where the asterisks denote the complex conjugate. At this point that one may define the Stokes parameters by considering real linear combinations of the matrix elements of C,

$$\begin{aligned} I &= k(C_{11} + C_{22}) = k\langle A_x^2 + A_y^2 \rangle \\ Q &= k(C_{11} - C_{22}) = k\langle A_x^2 - A_y^2 \rangle \\ U &= k(C_{12} + C_{21}) = 2k\langle A_x A_y cos(\delta_x - \delta_y) \rangle \\ V &= k(C_{21} - C_{12}) = 2k\langle A_x A_y sin(\delta_x - \delta_y) \rangle \end{aligned} \tag{1-11}$$

where k is a dimensionless constant. The polarized light can be described (Hecht, 1998) with the Stokes vector:

$$I = \begin{pmatrix} I \\ Q \\ U \\ V \end{pmatrix} \tag{1-12}$$

If we analyze Equations 1-11, we can deduce the relation:

$$I \geq Q + U + V \tag{1-13}$$

When equality occurs, the light beam is completely polarized light. When $Q = U = V = 0$, the light is called natural or totally unpolarized. To determine the polarization state of quasi-monochromatic light, two essential optical components are required: a linear polarizer and a linear retarder. The linear polarizer allows maximum transmission of one component of the electric field (E) and reflects or absorbs the component in the perpendicular direction. On the other hand, the linear retarder introduces a retardance (δ) to one of the Cartesian components of E. The axis on which the retardance is induced is known as the slow axis, while the orthogonal axis is referred to as the fast axis. Assuming that the fast axis is represented by x and the slow axis by y, the resulting electric field after passing through both the linear polarizer and analyzer can be considered as:

$$E_\theta = E_x cos\theta + E_y e^{i\delta} sin\theta \tag{1-14}$$

where θ is the angle between the positive x axis and E. The intensity can be understood as a linear combination of Stokes I, Q, U and V :

$$I_{meas}(\theta, \delta) = \frac{1}{2}(I + Qcos2\theta + Ucos\delta\ sin2\theta + Vsin\delta\ sin2\theta) \tag{1-15}$$

The quantity I_{meas} denotes the measured intensity. By varying θ and δ, the four-component Stokes vector can be determined. The Stokes Q and U represent the linearly polarized light, while V indicates the circularly polarized light. Additionally, the parameter I represents the overall intensity of the incoming light, providing a comprehensive description of the light's properties, so that

$$\begin{aligned} I &= I_{meas}(0,0) + I_{meas}(\pi/2,0) \\ Q &= I_{meas}(0,0) - I_{meas}(\pi/2,0) \\ U &= I_{meas}(\pi/4,0) - I_{meas}(3\pi/4,0) \\ V &= I_{meas}(\pi/4,\pi/2) - I_{meas}(3\pi/4,\pi/2) \end{aligned} \tag{1-16}$$

where I was obtained by measuring the intensity of the light beam after passing through two linear polarizers whose axes are orthogonally oriented at $\theta = 0^\circ$ and 90°, Q is the difference between linearly polarized lights at $\theta = 0^\circ$ and 90° , U is the difference between linearly polarized lights at $\theta = 45^\circ$ and 135°, and V is the difference between right-handed and left-handed circularly polarized lights and is measured by passing light through a quarter wave-plate linear analyzer and two linear polarizers at $\theta = 45^\circ$ and 135°.

Chapter 2 Synthetic and inversion methods

The primary objective of solar physics research is to determine the physical parameters that characterize the processes occurring in the solar atmosphere. The Stokes profiles obtained from the solar atmosphere and measured in polarized light can be accurately described by the Radiative Transfer Equation. This equation provides insights into how the Stokes profiles are influenced by the atmospheric conditions. To infer different physical quantities, particularly the magnetic field vector and plasma velocity, numerous techniques have been developed, and these techniques primarily rely on approximations of the RTE and exploit the distinct properties exhibited by spectral lines that are sensitive to the magnetic field.

2.1 Radiative transfer equation (RTE)

The transmission of electromagnetic energy through the atmosphere of a star presents a highly intricate and scientifically intricate problem. It involves nonlinearity, three-dimensionality, and time-dependence, encompassing the characteristics of the entire atmosphere. The behavior of matter and radiation at a particular depth is influenced by their counterparts in other layers since light emitted at one location can undergo absorption or scattering at another location, thereby releasing some or all of its energy. To comprehensively describe the entire system comprising matter and radiation, we must solve a set of interconnected equations that depict the physical state of the atomic system and the behavior of radiation as it traverses through the matter. Consequently, we need to simultaneously address the statistical equilibrium equations and the radiative transfer equation. Initially, we assume that the radiative transfer process is one-dimensional, meaning that the transfer of radiative energy perpendicular to the line of sight can be disregarded when considering the coupling between matter and radiation.

The Sun's outer layers exhibit a notable deviation from symmetry, resulting in an exponential decrease in density as we move away from its surface. Consequently, the radiation field becomes anisotropic, meaning that its properties vary depending on the direction of observation. Within this context, it is plausible for the energy levels of the

atom to be not evenly populated, and for non-zero coherences or phase relations between these levels to exist. This phenomenon is referred to as polarization, wherein the atomic system's state is most accurately described using the density operator (ρ). In the conventional representation employing eigenvectors of the total angular momentum (J^2) and its third component (J_z), the density matrix element is mathematically expressed as

$$\rho(\alpha jm, \alpha' j' m') = \langle \alpha jm \,|\rho|\, \alpha' j' m' \rangle \tag{2-1}$$

where α and α' stand for supplementary quantum numbers relative to those operators that commute with J^2 and J_z. Additionally, the diagonal matrix elements $\rho_\alpha(jm, jm) \equiv \rho(\alpha jm, \alpha jm)$ represent the populations of the magnetic sublevels and the sum, for the total population of the level characterized by the j quantum number, can be defined as

$$n_j = \sum_m \rho_\alpha(jm, jm) = \sum_{m=-j}^{j} \langle \alpha jm \,|\rho|\, \alpha jm \rangle \tag{2-2}$$

The equations governing the changes in the density matrix elements must be developed to accurately depict their temporal variations resulting from the transport of radiation and particle collisions. It is crucial to account for all interactions with light and various types of collisions. As demonstrated in the research conducted by Landi Degl'Innocenti et al. (2004), the radiative interaction equations in the magnetic field reference frame can be written as

$$\begin{aligned}
\frac{d}{dt}\rho_\alpha(jm, j'm') = & -2\pi i\, \nu_\alpha(jm, j'm')\, \rho_\alpha(jm, j'm') \\
& + \sum_{\alpha_l j_l m_l j_l' m_l'} \rho_{\alpha_l}(j_l m_l, j_l' m_l')\, T_A\,(\alpha jmj'm', \alpha_l j_l m_l j_l' m_l') \\
& + \sum_{\alpha_u j_u m_u j_u' m_u'} \rho_{\alpha_u}(j_u m_u, j_u' m_u') \Big[T_E\,(\alpha jmj'm', \alpha_u j_u m_u j_u' m_u') \\
& + T_S\,(\alpha jmj'm', \alpha_u j_u m_u j_u' m_u') \Big] \\
& - \sum_{j''m''} \Big\{ \rho_\alpha(jm, j''m'') \Big[R_A(\alpha j'm'j''m'') + R_E(\alpha j''m''j'm') \\
& + R_S(\alpha j''m''j'm') \Big] + \rho_\alpha(j''m'', j'm') \Big[R_A(\alpha j''m''jm) \\
& + R_E(\alpha jmj''m'') + R_S(\alpha jmj''m'') \Big] \Big\}
\end{aligned} \tag{2-3}$$

where $\nu_\alpha(jm, j'm')$ is the frequency difference between the two sublevels and the R's and T's are radiative rates of relaxation and coherence transfer among the sublevels, respectively. The collisional interactions give

$$\begin{aligned}\frac{d}{dt}\rho_\alpha(jm,j'm') = &\sum_{\alpha j_l m_l m_l'} C_I(\alpha_l j m m', \alpha_l j_l m_l m_l')\ \rho_{\alpha_l}(j_l m_l, j_l m_l') \\ &+ \sum_{\alpha_u j_u m_u m_u'} C_S(\alpha j m m', \alpha_u j_u m_u m_u')\ \rho_{\alpha_u}(j_u m_u, j_u m_u') \\ &+ \sum_{m'' m'''} C_E(\alpha j m m', \alpha j m'' m''')\ \rho_\alpha(jm'', jm''') \\ &- \sum_{m''}\Big[\frac{1}{2}X(\alpha j m m' m'')\ \rho_\alpha(jm, jm'') + \frac{1}{2}X(\alpha j m' m m'')^*\ \rho_\alpha(jm'', jm') \\ &- \frac{1}{2}X_E(\alpha j m m' m'')\ \rho_\alpha(jm, jm'') + \frac{1}{2}X_E(\alpha j m' m m'')^*\ \rho_\alpha(jm'', jm')\Big]\end{aligned} \tag{2-4}$$

where the X's are relaxation rates, the C's are collisional transfer rates between levels and the asterisk indicates the complex conjugate.

The RTE describes the changes in the radiation field, specifically the intensity, as it interacts with the material within a particular layer. When a magnetic field is present, modifications are necessary to account for the evolution of the Stokes vector as it passes through the layer. Therefore, the RTE can be expressed as (e.g., del Toro Iniesta, 2003)

$$\frac{d\mathbf{I}}{d\tau} = \mathbf{K}(\boldsymbol{I} - \mathbf{S}) \tag{2-5}$$

where $\mathbf{I} \equiv (I, Q, U, V)^T$ define the vector of Stokes parameters, τ is the continuum optical depth at a reference wavelength, $\mathbf{K}$ for the propagation matrix, $\mathbf{S} \equiv (B_\upsilon(T), 0, 0, 0)^T$ for the source function vector, and index T means the transpose. In local thermodynamic equilibrium (LTE), the source function vector is the Planck function ($B_\upsilon(T)$), where the radiation field is unpolarized and where the temperature is a function of height in the atmosphere.

The propagation matrix **K** of the RTE has some properties of symmetry and, with only seven independent parameters, can given by

$$\mathbf{K} = \begin{pmatrix} \eta_I & \eta_Q & \eta_U & \eta_V \\ \eta_Q & \eta_I & \rho_V & -\rho_U \\ \eta_U & -\rho_V & \eta_I & \rho_Q \\ \eta_V & \rho_U & -\rho_Q & \eta_I \end{pmatrix} \tag{2-6}$$

Here η_I describes the absorption of the radiation regardless of its polarization state. η_Q, η_U and η_V the coupling of the intensity I with the component Q, U and V due to absorption. And the terms ρ_Q, ρ_U and ρ_V the crosstalk between the polarized components Q, U and V. These elements can be expressed as (Unno, 1956; Rachkovsky, 1962)

$$\begin{aligned}
\eta_I &= 1 + \frac{\eta_0}{2}\left[\phi_p sin^2\theta + \frac{\phi_b + \phi_r}{2}(1 + cos^2\theta)\right] \\
\eta_Q &= \frac{\eta_0}{2}\left[\phi_p - \frac{\phi_b + \phi_r}{2}\right] sin^2\theta\ cos2\chi \\
\eta_U &= \frac{\eta_0}{2}\left[\phi_p - \frac{\phi_b + \phi_r}{2}\right] sin^2\theta\ sin2\chi \\
\eta_V &= \frac{\eta_0}{2}\left[\phi_r - \phi_b\right] cos\theta \\
\rho_Q &= \frac{\eta_0}{2}\left[\psi_p - \frac{\psi_b + \psi_r}{2}\right] sin^2\theta\ cos2\chi \\
\rho_U &= \frac{\eta_0}{2}\left[\psi_p - \frac{\psi_b + \psi_r}{2}\right] sin^2\theta\ sin2\chi \\
\eta_V &= \frac{\eta_0}{2}\left[\psi_r - \psi_b\right] cos\gamma
\end{aligned} \tag{2-7}$$

The variables θ and χ are the line-of-sight inclination and azimuth, respectively, and η_0 is the ratio between the line and the continuum absorption coefficients. ϕ and ψ are the absorption and dispersion profiles, and the indices p, b, r stand for the π and σ components of a Zeeman multiplet. ϕ and ψ can be expressed as

$$\phi_j = \sum_{M_l - M_u = j} S_{M_l M_u, j} \frac{1}{\sqrt{\pi}} H(\alpha, v) \tag{2-8}$$

$$\psi_j = 2\sum_{M_l - M_u = j} S_{M_l M_u, j} \frac{1}{\sqrt{\pi}} F(\alpha, \upsilon) \tag{2-9}$$

where $S_{M_l M_u, j}$ is the strength of each component, and j takes ± 1 for the σ components of the absorption line and 0 for the π component. υ stands for the wavelength shift in Doppler units, while **H** and **F** are the Voigt and Faraday-Voigt functions which can be given by

$$\mathbf{H}(\alpha, \upsilon) = \frac{a}{\pi} \int_{-\infty}^{\infty} e^{-y^2} \frac{1}{(\upsilon - y)^2 + a^2} dy \tag{2-10}$$

$$\mathbf{F}(\alpha, \upsilon) = \frac{1}{\pi} \int_{-\infty}^{\infty} e^{-y^2} \frac{\upsilon - y}{(\upsilon - y)^2 + a^2} dy \tag{2-11}$$

2.2 The solution of RTE

By using a model atmosphere, an analytical solution is found for the Radiative Transfer Equation. Such a model (x) has a number of physical parameters as a function of geometrical height (z) or optical depth of continuum (τ_c),

$$x(\tau_c) = [T(\tau_c), p_e(\tau_c), V_{mic}(\tau_c), B(\tau_c), V_{LOS}(\tau_c), \theta(\tau_c), \phi(\tau_c)] \tag{2-12}$$

where T is the temperature, p_e is the electron pressure, V_{mic} is the microturbulent velocity, B is the magnetic field strength, and V_{LOS} is the line-of-sight(LOS) velocity. Furthermore, θ is the inclination of the magnetic field with respect to LOS of the observer, and ϕ is the azimuth of the magnetic field in the plane perpendicular to LOS of the observer, as seen in Figure 2-1.

Landi Degl'Innocenti et al. (1985) achieved the initial endeavor of resolving the general Radiative Transfer Equation. They proposed that the observed Stokes profiles between two optical depths τ_0 and τ_1 can given by

$$\mathbf{I}(\tau_1) = \mathbf{O}(\tau_1, \tau_0)\mathbf{I}(\tau_0) - \int_{\tau_0}^{\tau 1} \mathbf{O}(\tau_1, \tau_0)\mathbf{K}(\tau_c)\mathbf{S}(\tau_c) d\tau_c \tag{2-13}$$

where **O** is the evolution operator, τ_0 is the observer's optical depth, and τ_1 is the optical depth of bottom of the atmosphere that is so deep that the plasma is optically thick. As no photon can escape from the bottom of atmosphere, so

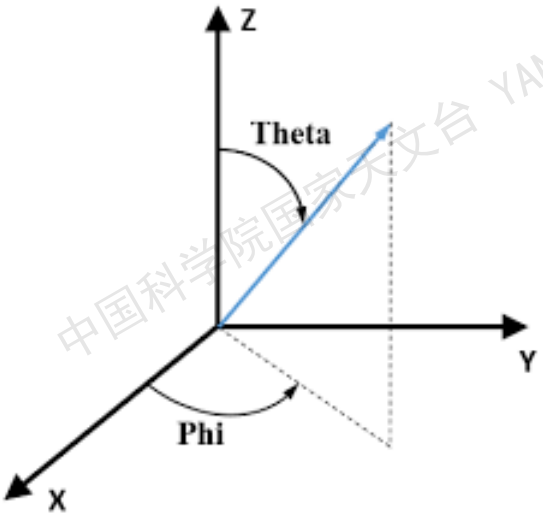

Figure 2-1 Reference frame for magnetic field vector (blue line vector). The z-axis shows the direction of the beam propagation and align with the observer' s LOS. The magnetic field vector has an inclination (θ) to the propagation direction, while the field azimuth (ϕ) measured from the axis x to B.

$$\lim_{\tau_0 \to \infty} \mathbf{O}(0, \tau_0)\mathbf{I}(\tau_0) = 0 \tag{2-14}$$

Then the solution of RTE in Equation 2-13 can be written as

$$\mathbf{I}(\tau_1) = \int_0^{\infty} \mathbf{O}(0, \tau_c)\mathbf{K}(\tau_c)\mathbf{S}(\tau_c) d\tau_c \tag{2-15}$$

This solution is called formal because it is not a real solution as long as the evolution operator, the propagation matrix, and the source function vector are not known. Unfortunately, obtaining an analytical expression for the evolution operator is generally not straightforward. However, there is a specific scenario where the RTE can be solved: the Milne-Eddington atmosphere. In this case, the properties of the model atmosphere that impact the propagation matrix can be assumed to remain constant with optical depth. For all other situations, numerical computations of the evolution operator and solutions to the transfer equation are necessary. To obtain the emergent Stokes spectrum, a three-term product integral is performed across the entire atmosphere.

2.3 The response function

The Stokes profiles are useful for inferring given physical quantities as long as they change when those physical quantities vary. To fully understand the diagnostic capabil-

ities of Stokes profiles, it is necessary to solve the RTE, as in Equation 2-15. However, we face a challenging problem where the observable properties depend on the nonlinear interaction of three unknown factors, each of which is strongly influenced by the physical quantities that define the model atmosphere. Consequently, predicting changes in the Stokes profiles becomes extremely difficult when modifications are made to the physical parameters. However, if we assume that the perturbations are sufficiently small, the changes can be approximated linearly. According to Ruiz Cobo et al. (1994); Del Toro Iniesta et al. (1996), the sensitivity of the Stokes profiles to perturbations in atmospheric physical quantities can be expressed in the form of response functions (RFs). However, A perturbation δx in an atmospheric physical parameter (x) will induce modification $\delta I(0)$ to the observed Stokes profile which can given by

$$\delta \mathbf{I}(0) = \int_0^\infty \mathbf{R}(\tau_c)\, \delta x(\tau_c)\ \ d\tau_c \tag{2-16}$$

where $\mathbf{R}(\tau_c)$ is the response function vector which expressed as

$$\mathbf{R}(\tau_c) \equiv \mathbf{O}(0, \tau_c) \left[\mathbf{K}(\tau_c) \frac{\partial \mathbf{S}}{\partial x} - \frac{\partial \mathbf{K}}{\partial x} [\mathbf{I}(\tau_c) - \mathbf{S}(\tau_c)] \right] \tag{2-17}$$

with $\mathbf{O}(0, \tau_c)$ is the evolution operator from τ_c to the surface, $\mathbf{K}(\tau_c)$ is the propagation matrix, and $\mathbf{S}(\tau_c)$ is the source function vector.

In the case of atmospheric model with constant parameters, we can say that RFs are indeed the partial derivatives of $\mathbf{I}(0)$ with respect to the atmospheric physical parameters, and they directly provide the sensitivities of the Stokes spectrum to perturbations of the physical conditions in the medium:

$$\mathbf{R}_x(\lambda) = \frac{\partial \mathbf{I}(\lambda)}{\partial x} \tag{2-18}$$

where x represents any of the atmospheric model parameters. The availability of an analytic solution for the RTE in this particular atmosphere allows for the analytical formulation of the sensitivities of spectral lines, as represented by Response Functions (RFs). These RFs can be obtained by taking partial derivatives of the aforementioned solution with respect to the model parameters. Fortunately, the shapes of RFs demonstrate relatively consistent characteristics across various models and spectral lines. The RFs prove to be valuable tools for comprehending the formation of spectral lines and

the behavior of Stokes profiles under different formation conditions. Furthermore, they offer practical guidelines for selecting appropriate spectral lines for specific purposes, as well as for selecting wavelength samples, among other applications.

2.4 Milne-Eddington inversion

The Milne-Eddington (ME) inversion is a fundamental technique in astrophysics and solar physics used to interpret spectropolarimetric observations, particularly in the context of stellar atmospheres and solar magnetic fields. This method enables researchers to derive key physical parameters of the atmosphere, such as temperature, density, and magnetic field strength, from the observed polarization states of light.

The method is named after two prominent scientists: Arthur Milne and Friedrich Eddington, who contributed to the understanding of radiative transfer in stellar atmospheres. The Milne-Eddington approximation simplifies the complex radiative transfer equations, making it feasible to analyze spectral lines in a magnetized medium.

The ME code relies on four key assumptions to solve the RTE analytically:

- Plane-parallel atmosphere: The atmosphere varies only in depth (vertical direction) and is horizontally homogeneous. This simplification allows the radiative transfer equation to be solved in 1D, making spectral inversions computationally feasible.
- Depth-independent parameters: Magnetic field strength (B), inclination (θ), azimuth (χ), Doppler width ($\Delta\lambda_D$), and line-of-sight velocity ($V_L OS$).
- Linear source function dependence on optical depth (τ):$S(\tau) = S_0 + S_1\tau$.
- Local Thermodynamic Equilibrium (LTE) for line formation.
- Optically thin medium: The method is often applied in regions where the medium does not absorb much light, which is a reasonable approximation for many astrophysical environments.

These assumptions allow analytic solutions for Stokes parameters, making ME codes computationally efficient for deriving average magnetic field and velocity values from photospheric spectral lines like Fe I 630 nm (Orozco Suárez et al., 2010). There are many inversion codes based on ME assumption, such as:

- HAO Code: Developed by Skumanich et al. (1987), optimized for photospheric line analysis

- VFISV: Designed for the Helioseismic and Magnetic Imager (HMI), uses fast Levenberg-Marquardt optimization (Borrero et al., 2011a).
- MELANIE: Supports multi-line inversions and complex profile fitting (Socas-Navarro, 2001).

While the ME inversion is a powerful tool in the analysis of spectropolarimetric data in astrophysics. Its ability to provide insights into the physical conditions of stellar and solar atmospheres makes it invaluable for advancing our understanding of celestial phenomena. ME inversion has limitations:

(1) Simplifying Assumptions: The assumptions of a plane-parallel atmosphere and constant magnetic field may not hold in more complex environments.

(2) Noise and Resolution: Observational noise and spectral resolution can significantly impact the accuracy of the inversion results.

(3) Non-unique Solutions: The inversion may yield non-unique solutions, necessitating additional constraints or prior information to achieve reliable results.

Continued advancements in observational technology and computational methods are likely to enhance the application of this technique in various fields of astrophysics.

2.5 Stokes Inversion based on Response functions

The Stokes Inversion based on Response functions (SIR; Ruiz Cobo et al., 1992) is a widely used technique for inferring the physical properties of the plasma in the solar atmosphere from the observable Stokes spectra. The method employs the solution of the RTE under local thermodynamic equilibrium (LTE) and assumes a plane-parallel atmosphere. It incorporates the depth dependence of crucial physical parameters involved in the formation of spectral lines. By introducing small perturbations $\delta x_i(\tau_c)$ to the model parameters, it accounts for slight modifications in the Stokes vector ($\delta\mathbf{I}$), source function ($\delta\mathbf{S}$), and propagation matrix ($\delta\mathbf{K}$).

$$\delta\mathbf{K} = \sum_{j=1}^{m} \frac{\partial\mathbf{K}}{\partial x_j} x_j(\tau_c) \tag{2-19}$$

$$\delta\mathbf{S} = \sum_{j=1}^{m} \frac{\partial\mathbf{S}}{\partial x_j} x_j(\tau_c) \tag{2-20}$$

where m is the model parameters. So we can rewrite the solution of RTE(Equation 2-16) in term of perturbations as:

$$\delta \mathbf{I}(0) = \sum_{j=1}^{m} \int_0^{\infty} \mathbf{R}_j(\tau_c)\, \delta x_j(\tau_c)\ d\tau_c \tag{2-21}$$

where the response function ($\mathbf{R}_j$) is a four-vector which represents different aspects of the Stokes parameters and depends on τ_c and the wavelength. The reciprocal units of the RFs correspond to the respective parameters. From Equation 2-17, RFs can be expressed using **K**, **S**, and their derivatives, allowing for analytical calculations in LTE. By solving the RTE in LTE for an initial model estimation, the SIR code generates synthetic Stokes profiles. In the context of the inversion problem, we aim to determine the relevant model parameters by minimizing the squared differences between observed (I_s^{obs}) and synthetic (I_s^{syn}) Stokes profiles. Therefore, all inversion codes rely on minimizing a merit function $\chi^2(x)$, which can be expressed as

$$\chi^2(x) = \frac{1}{N_f} \sum_{s=0}^{3} \sum_{i=1}^{N_\lambda} \left[I_s^{obs}(\lambda_i) - I_s^{syn}(\lambda_i; x) \right]^2 \omega_{s,i}^2 \tag{2-22}$$

where N_f stands for the number of degrees of freedom, s is a given Stokes parameter, N_λ is wavelength samples and $\omega_{s,i}$ is a statistical weight that may be applied to each Stokes parameter. To establish the necessary modifications to the model during each iteration, the SIR code assesses the partial derivatives of χ^2 concerning the free model parameters. Building upon the work of Ruiz Cobo et al. (1992, 1994), the SIR technique utilizes the RFs to directly obtain the first and second partial derivatives of χ^2 with respect to two specific model parameters, referred to as x_m and x_k:

$$\frac{\partial \chi^2}{\partial x_m} = \frac{2}{N_f} \sum_{s=0}^{3} \sum_{i=1}^{N_\lambda} \left[I_s^{obs}(\lambda_i) - I_s^{syn}(\lambda_i; x) \right] \omega_{s,i}^2\ R_{m,s}(\lambda_i) \tag{2-23}$$

$$\frac{\partial^2 \chi^2}{\partial x_m \partial x_k} = \frac{2}{N_f} \sum_{s=0}^{3} \sum_{i=1}^{N_\lambda} \omega_{s,i}^2 \left[R_{m,s}(\lambda_i)\ R_{k,s}(\lambda_i) \right] \tag{2-24}$$

The subsequent application of a Levenberg-Marquardt algorithm involves perturbing the initial model by adjusting a variable number of nodes at specific optical depths within a chosen set of atmospheric parameters. The final depth structure is determined using cubic splines or linear interpolation between these nodes. However, the algorithm requires an initial guess model atmosphere to initiate the process. Gradually, the model is modified iteratively to make the synthetic Stokes profiles increasingly resemble the

observed data. As we approach the minimum χ^2 solution, the Levenberg-Marquardt algorithm (e.g., Press et al., 1986) imposes certain requirements that

$$\Delta\chi^2 + \mathbf{H}\delta x = 0 \tag{2-25}$$

where the δx stand for the direction on the N-dimensional space and the modified Hessian matrix (**H**) is one half of the Hessian matrix ($H'_{mk} = \partial^2\chi^2/\partial x_m \partial x_k$) and defined as

$$2H_{mk} = \begin{cases} H'_{mk}(1+\lambda), & \text{if } m = k \\ H'_{mk}, & \text{if } m \neq k \end{cases} \tag{2-26}$$

The scaling factor λ dynamically adjusts in each iteration based on the magnitude of the χ^2 variation, indicating our proximity to the minimum. As we approach the minimum, one can get

$$\delta x = -\mathbf{H}^{-1}\Delta\chi^2 \tag{2-27}$$

The iterative process of solving the RTE and perturbing the model continues until the χ^2 value decreases to a negligible extent. To optimize computational efficiency, the SIR code significantly reduces the number of free parameters by perturbing the model only at specific points or 'nodes' in optical depth for each free parameter. To prevent singularities in **H**, a modified version of singular value decomposition (SVD) is utilized. Executing the inversion code is straightforward: inputting a set of observed Stokes profiles and an initial guess model atmosphere, the code solves the RTE and calculates the corresponding RFs, and iteratively updates the model until the best fit is achieved.

As the Hessian matrix is made up of RFs (see, Equation 2-24), one can obtain the inversion uncertainties in the physical quantities as a function of the RFs by

$$\sigma_m^2 \approx \frac{2}{np+r} \frac{\sum_{s=0}^{3}\sum_{i=1}^{N_\lambda}\left[I_s^{obs}(\lambda_i) - I_s^{syn}(\lambda_i;x)\right]^2 \omega_{s,i}^2}{\sum_{s=0}^{3}\sum_{i=1}^{N_\lambda} R_{m,s}^2(\lambda_i)\,\omega_{s,i}^2} \tag{2-28}$$

The model is represented by a vector x of $np + r$ components, where n being the number of depth grid points throughout the atmosphere, p is the number of physical

quantities varying with depth, and r is the number of quantities that are assumed constant throughout the line of sight (LOS). As the RFs became larger, the uncertainties decrease and more accurate results were obtained from the inversion. The absence of distinctiveness might become apparent when relying on the initial guess parameters. This realization has been acknowledged by the scientific community for quite some time, and extensive testing of the SIR codes has demonstrated their robust to various initializations (Ruiz Cobo et al., 1992). However, this robustness could still vary depending on the specific Stokes profiles and atmospheric model being used. Therefore, it is advisable to employ multiple different initial guesses when uncertainty arises, in order to estimate the uncertainties associated with each physical quantity in the results. Numerous attempts have also been made to discover an optimal initial guess for initialization.

2.5.1 Two-component model atmospheres

SIR utilizes a model atmosphere that is defined by the parameters described in Equation 2-12. These parameters depend on optical depth τ_c , but there are other additional parameters required by SIR. One of the parameter addresses SIR's ability to represent sub-structures within the resolution element. In any two-component model atmosphere, it is assumed that within the resolution element, two distinct atmospheres coexist: a first magnetic atmosphere occupying a fraction (f_1) of the surface and a second magnetic atmosphere occupying the remaining fraction (f_2), with $f_1 + f_2 = 1$. If we denote the Stokes profile vector emerging from the first atmosphere as $\mathbf{I}_1$ and the vector from the second atmosphere as $\mathbf{I}_2$, the resulting Stokes vector, $\mathbf{I}$, can be expressed as

$$\mathbf{I} = f_1\mathbf{I}_1 + f_2\mathbf{I}_2 \tag{2-29}$$

The code incorporates the impact of straylight caused by the instrument. To account for straylight, we employ an averaging method on the incoming Stokes I profiles from the surrounding regions that lack magnetization.This averaged profile is then utilized in conjunction with the SIR code. The straylight portion is characterized by a single free parameter (α), where α was the fitted straylight fraction retrieved from the SIR. The final Stokes vector is expressed as follows:

$$\mathbf{I} = \alpha \mathbf{I}_{stray} + (1 - \alpha)\mathbf{I}_m \tag{2-30}$$

where $\mathbf{I}_m$ denotes the magnetic component and $\mathbf{I}_{stray}$ represents the straylight component. In this case, the stray light may be interpreted as a non-magnetized component, which is equivalent to a two-component atmosphere. One component is assumed to have an embedded magnetic field, and the others do not. The magnetic filling factor, denoted as f, is calculated as $f = 1 - \alpha$ to quantify the proportion of magnetization.

One can incorporate an extra broadening of the spectral lines caused by the macro-turbulent velocity (v_{mac}). This factor takes into consideration the turbulent motions that remain unresolved because they occur on a scale larger than the mean free path of the observed photons. To achieve this, each Stokes parameter is convolved with a Gaussian function

$$G_{mac}(\lambda) = \frac{1}{\sqrt{2\pi}\sigma} e^{-\frac{1}{2}\left(\frac{\lambda-\lambda_o}{\sigma}\right)} \tag{2-31}$$

and the parameter σ is given by

$$\sigma = \frac{\lambda_o v_{mac}}{c} \tag{2-32}$$

where λ_o is the central wavelength of the transition and c is the speed of the light.

2.5.2 The nodes selection

SIR employs a comprehensive approach to stratify the parameters of the model. By evaluating perturbations at specific depth grid points known as nodes, the total number of free parameters is reduced. Each physical quantity within the atmosphere is represented by its own set of nodes. The selection of nodes determines the optical depths where perturbations of the physical parameters will be sought. For instance, if two nodes are specified, perturbations will be sought at $log\tau = -5.0$ and $log\tau = 2.0$. When three nodes are chosen, perturbations will be sought at $log\tau = -5.0$, $log\tau = -1.5$, and $log\tau = 2.0$ (see Figure 2-2). The perturbations at the remaining grid points are estimated through linear or cubic-spline interpolation based on the perturbations at the nodes. For example, using a single node results in a constant modification across the entire atmosphere, while two nodes lead to a straight line perturbation passing through

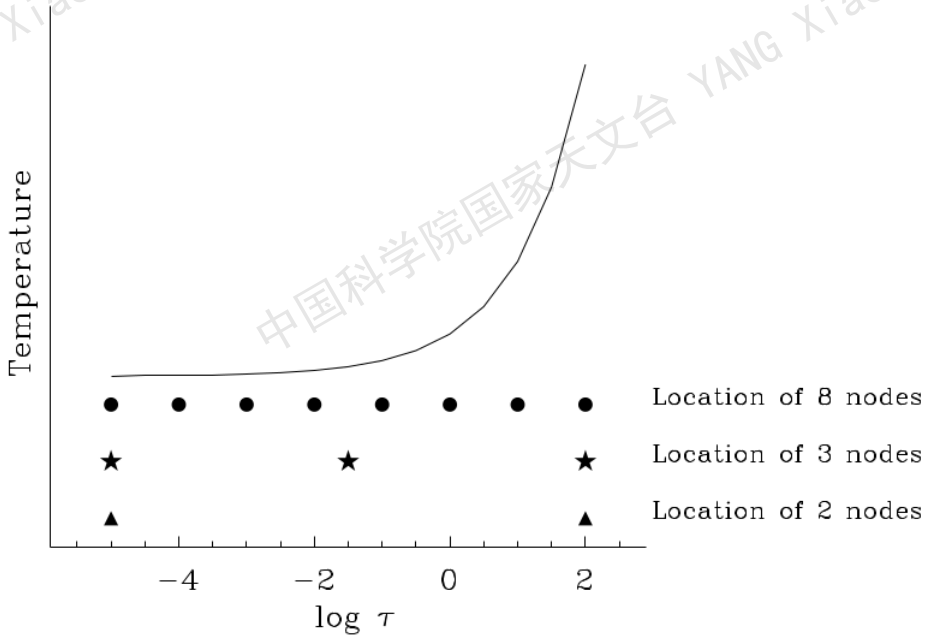

Figure 2-2 Schematic graph which show the location of the different number of nodes as specified by SIR code.

the nodes. With three nodes, the perturbation takes a parabolic shape, and so on. Note that the number of free parameters equals the sum of the number of nodes adopted for the various physical quantities.

The current version of SIR incorporates an algorithm that automatically selects a suitable number of nodes for each parameter in every iteration. This algorithm is based on finding the roots or zeros of the partial derivative of χ^2 with respect to each parameter, as described in Equation 2-23. Let's consider a specific atmospheric quantity, denoted as "a", which varies with optical depth, and let "a_p" represent its value at τ_p. In other words, "a_p" is one of the elements in the model atmosphere. We define "d_{a_p}" as the partial derivative ($\partial\chi^2/\partial a_p$). Assuming that we are analyzing the intensity profile of a single spectral line and that, at a particular iterative step, the observed intensity (I_{obs}) is greater than the synthetic intensity (I_{syn}) for all wavelengths. If the quantity $R_{p,0}(\lambda_i)$ is positive across all wavelengths and optical depths, it becomes evident that "d_{a_p}" will also be positive at all depths. Therefore, to achieve a better fit, we need to increase "a" everywhere, and a single node might suffice. Based on this reasoning, we can conclude that the number of nodes for a given physical quantity should be related to the number of times the derivative "d_a" changes its sign over the range of optical depths. However, since the derivative is influenced by noise present in the observational data, spurious ze-

ros must be eliminated. Consequently, the algorithm determines the number of nodes by identifying positive relative maxima and negative relative minima that exceed a certain threshold in absolute value.

2.6 STockholm inversion Code

STockholm inversion Code (STiC) is a powerful tool used in solar physics for modeling and analyzing the polarization signals of spectral lines emitted by the Sun (de la Cruz Rodríguez et al., 2016, 2019). This code is specifically designed to handle non-LTE (non-local thermodynamic equilibrium) conditions and partial redistribution (PRD) effects, allowing for a more accurate representation of the physical processes happening in the solar atmosphere.

The STiC code incorporates a sophisticated non-LTE radiative transfer solver based on the widely-used RH code (Uitenbroek, 2001). The RH code enables the calculation of spectral line profiles, taking into account the non-equilibrium conditions prevalent in the solar atmosphere. Moreover, it can simultaneously solve the non-LTE problem for multiple atomic lines, considering the stratification of temperature, hydrogen populations, electron density, vertical velocity, and microturbulence as a function of optical depth. the STiC code incorporates PRD effects in strong resonance lines, including a fast approximation for angle-dependent PRD (Leenaarts et al., 2012). The PRD accounts for the scattering of photons within the line profile, which can significantly affect the emergent spectrum.

To create a realistic representation of the solar atmosphere, the STiC code begins by defining the temperature, velocity, and microturbulence profiles at different depths within the atmosphere. These profiles are expressed as functions of optical depth, which measures how opaque the atmosphere is at a given point. The code then calculates the hydrogen and electron densities, as well as the height scale of the atmosphere, using an LTE equation of state (Piskunov et al., 2017) and the principle of hydrostatic equilibrium. This ensures that the model atmosphere is consistent with the physical laws governing the Sun, resulting in a more accurate representation of the solar environment.

The STiC code can perform inversions in both full-Stokes mode and intensity-only mode. In full-Stokes mode, all four Stokes parameters (I, Q, U, and V) are considered, allowing for the analysis of polarized light. When mixing spectral regions with and

without polarization, the code operates in full-Stokes mode, assigning zero weight to the unpolarized regions in Stokes Q, U, and V. This ensures that the inversion process accurately accounts for the polarization properties of the observed spectrum.

The STiC code utilizes a simplified approach, known as the 1.5D approximation, to solve the equations governing the equilibrium of atoms within the solar atmosphere. This approach assumes a plane-parallel geometry, meaning that the atmosphere is treated as a series of flat layers stacked on top of each other. The code processes the atmosphere column by column, calculating the population densities of different atoms within each column.

Once these population densities are determined, a final calculation is performed to determine the emergent spectrum at the observed heliocentric angle. However, due to computational limitations, the code does not account for horizontal radiative transfer. This means that the code does not consider how light interacts with the atmosphere in directions perpendicular to the line of sight. The complexity of incorporating horizontal radiative transfer stems from the need to calculate the derivatives of the intensity vector with respect to each physical parameter, which is computationally expensive. Additionally, accounting for radiative coupling between different pixels would introduce further challenges.

2.6.1 The node parameterization

The STiC code employs a depth-stratified inversion technique based on nodes, building upon the work of Ruiz Cobo et al. (1992). These nodes represent the free parameters of our model atmosphere, defining the structure of the atmosphere at specific depths. During the inversion process, the code iteratively adjusts the values of these nodes, effectively refining the structure of the model atmosphere. This refined model, representing a more accurate representation of the real solar atmosphere, is then used to solve the polarized radiative transfer equation.

In the Ruiz Cobo et al. (1992) approach, the nodes represent corrections that are interpolated and added to an existing input model atmosphere, while the implementation of the nodes approach in STiC differs as they directly represent the actual values of the model atmosphere, which are then interpolated onto a finer depth grid. The Ruiz Cobo

et al. (1992) approach is advantageous when the input model atmosphere is already close to the final solution. However, if the input model has a complex structure that differs significantly from the true atmospheric profiles, this approach may struggle to remove these initial biases, even with a large number of nodes. On the other hand, the STiC approach offers a more robust solution by directly defining the depth complexity of the model atmosphere through the number of nodes.

STiC allows the user to choose from four types of non-overshooting interpolants: straight segments, quadratic Bezier splines, cubic Bezier splines, and discontinuous grid-centered interpolation with linear slope delimiters. This flexibility allows for different levels of smoothness and complexity in the interpolated profiles. Furthermore, the code implement node parameterization for temperature, line-of-sight velocity, microturbulence, and the magnetic field vector (B_l, B_T, B_χ), where B_l is the longitudinal component, B_T is the transverse component and B_χ is azimuth of the transverse component. This enables the code to effectively invert these key atmospheric parameters, providing a more comprehensive understanding of the physical conditions in the solar atmosphere.

2.6.2 The regularization

The Levenberg–Marquardt (LM) algorithm serves as a powerful tool for optimizing nonlinear least-squares fitting processes by aligning guess model with observational data. the LM methodically adjusts model parameters to narrow the gap between synthetic and actual data points. Within the STiC code, a regularized LM algorithm has been employed to counteract oscillations in the derived parameters, ensuring stable solutions even in contexts with numerous free parameters crucial for accurate observational fitting. Regularization methods offer a built-in mechanism to discourage specific solution types by incorporating a penalty function r($\boldsymbol{p}$) into the merit function χ^2 definition as:

$$\chi^2(\boldsymbol{p},\boldsymbol{x}) = \frac{1}{N_{dat}} \sum_{k=1}^{N_{dat}} \left[\frac{o_k - s_k(\boldsymbol{p},x_k)}{\sigma_k} \right]^2 + \sum_{n=1}^{N_{pen}} \alpha_n \, r_n(\boldsymbol{p})^2 \tag{2-33}$$

where the variable s_k is the k-th synthetic data point, corresponding to the k-th measured data point o_k and the k-th error σ_k. N_{pen} represents the number of the distinct

penalty functions that may vary based on different combinations of parameters within the vector $\boldsymbol{p}$, where $\boldsymbol{p}$ encompasses the model parameters. Moreover, α_n is the weight of regularization term.

Selecting the appropriate regularization weights (α_n) in this method poses a significant challenge. Excessive weighting can compromise fit quality by overshadowing the actual problem with penalty terms, while insufficient regularization fails to resolve potential solution ambiguities. Kochukhov (2017) offers a pragmatic insight into selecting regularization weights, advocating the utilization of the L-curvature approach (Hansen et al., 1993). This method involves plotting the square of the residual $||o - s||^2$ against the penalty term $||r||^2$ on a log-log scale for varied α values. Typically, when the penalty term's magnitude approaches that of $||o - s||^2$, fit quality starts deteriorating rapidly. The objective is to identify an α value near this pivotal point to achieve optimal results.

Chapter 3 Inferring magnetic field of quiet Sun internetwork

3.1 Introduction

The Sun was considered non magnetic everywhere outside active regions (e.g., sunspot and plage) until the analysis performed by Livingston et al. (1975), who firstly discover internetwork magnetic fields from the direct observations. The IN corresponds closely to the interior of supergranular cells (Sheeley, 1967), and these magnetic fields manifest as individual flux concentrations that exhibit radial trajectories influenced by the local granulation pattern. The presence of magnetic fields in the quiet Sun internetwork is of great importance for energy and mass transport, as well as the formation and evolution of various structures in the solar atmosphere. Covering a significant portion of the solar surface, the IN magnetic fields contribute approximately 26 Mx cm^{-2} per day to the solar magnetic flux (Zhou et al., 2013), which is over four orders of magnitude higher than the contribution from active regions.

Early investigations into the topology of IN magnetic fields revealed their characteristics, including weaker fields, smaller sizes, and shorter lifetimes (Lites et al., 1996; De Pontieu, 2002). Some of these structures are observed between two patches with opposite polarities and are interpreted as low-lying magnetic loops (Martínez González et al., 2007; Gömöry et al., 2010), where the circular patches represent the foot-points of the loop, while the linear patch corresponds to the loop's apex. Harvey et al. (2007) conducted observations and discovered that the magnetic fields exhibit seething patterns characterized by varying spatial and temporal scales. Furthermore, they found that the nearly horizontal component of these magnetic fields demonstrates an average linear polarization signal of approximately 10^{-3} relative to the unit of Stokes I continuum (I_c). About 23 % of these loops extend to the chromosphere, potentially supplying a substantial amount of energy to the upper layers of the solar atmosphere.

Understanding the nature of IN magnetism remains a challenge due to the weak signals and complexity, necessitating advanced optics instrumentation and analysis techniques. Over the past decade, there has been significant progress in accurately studying the characteristics of internetwork horizontal fields through high-resolution observa-

tions conducted with advanced instruments such as the VTT (Beck et al., 2009; Khomenko et al., 2003), Hinode (Lites et al., 2008; Jin et al., 2009), and SUNRISE/IMaX (Danilovic et al., 2010). These comprehensive investigations have provided further validation of the temporary nature of linear polarization features characterized by magnetic strengths of 100-200 G. These features display temporal and spatial scales comparable to granular cells, as observed by Ishikawa et al. (2010, 2011).

The Hinode satellite, launched in 2006, has played a significant role in advancing our understanding of the quiet Sun's magnetic field topology in the photosphere. The Hinode spectropolarimeter (SP: Lites et al., 2013) provides high-sensitivity data for the full Stokes profiles (I, Q, U, and V) with a spatial resolution of $0.3''$ in the pair of neutral iron lines (Fe I) at 6301.5 and 6302.5 . Observations from Hinode SP have been used to study the orientations of internetwork fields, with some analyses indicating predominantly horizontal fields (Orozco Suárez et al., 2007a; Ishikawa et al., 2009; Orozco Suárez et al., 2012a; Lites et al., 2017), while others suggest isotropic distributions (Asensio Ramos, 2009). Ground-based spectropolarimetric observations analyzed by Stenflo (2013) indicated a mostly vertical internetwork field. It's important to note that some of these studies employed Stokes inversion techniques, which have been shown to be influenced by observational noise, as detailed by Borrero et al. (2011b). In this study, we consider the effect of noise on the SP data and focus on analyzing the inclination distribution based on linear polarization signals above 4.5 times the noise level to ensure reliable results.

The Stokes V profiles, obtained by Hinode SP, present significant asymmetries from large to small degree (Viticchié et al., 2011) and contain great information about the physical stratification of the atmospheric parameters in the photosphere (see Figure 3-1). The asymmetries in the observed Stokes profiles were generated by gradients of magnetic field vector and flow velocity along the line-of-sight. The Milne–Eddington (ME) inversions have been used to determine the magnetic field vector, but they could not reproduce the observed asymmetries because that inversion method assumes that the magnetic field parameters are independent of height. In this paper, we applied the SIR inversion taking into account the gradients of atmospheric parameters, a technique that not only reproduces the observed asymmetries, but also has a precise ability to obtain more information about the magnetic field configurations at various heights.

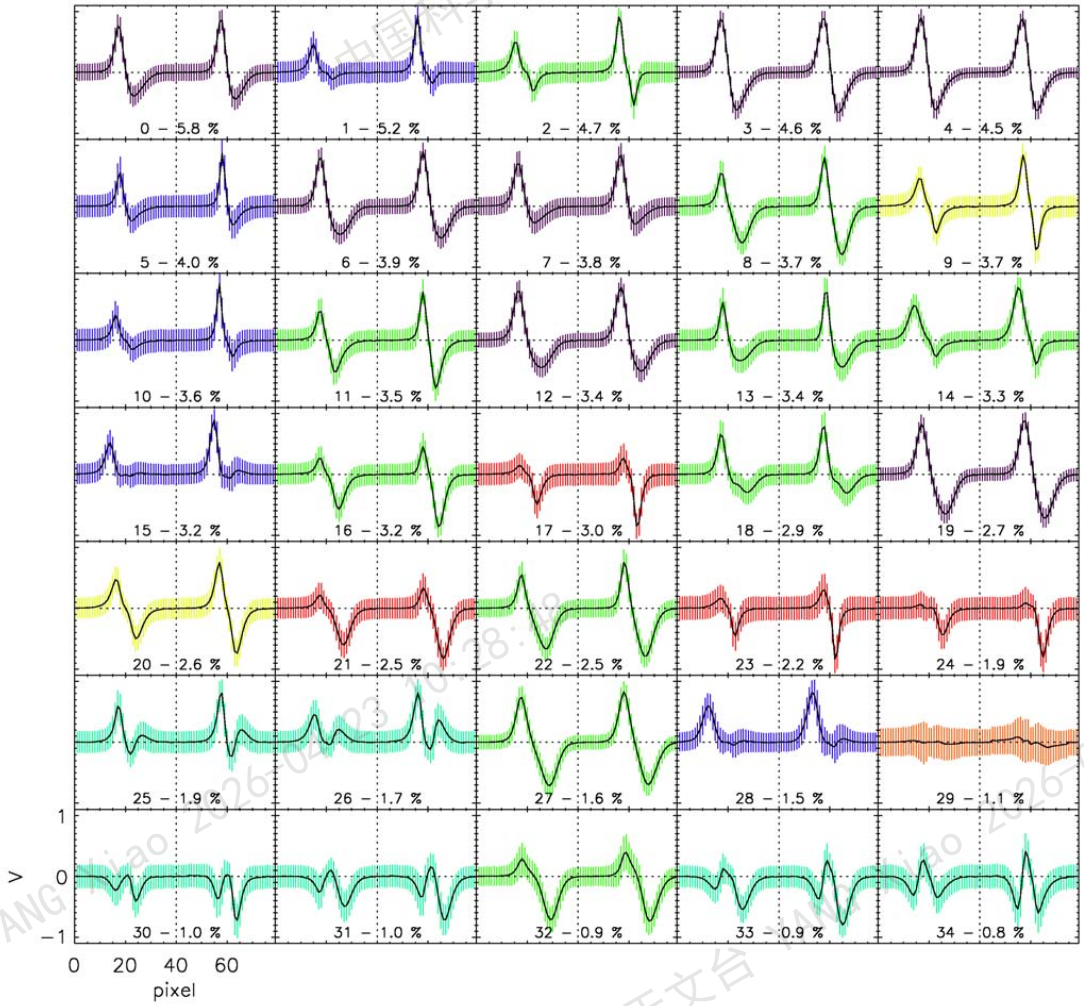

Figure 3-1 The classification of Stokes V profiles of Fe I 6301.5 Å (left side in each panel) and Fe I 6302.5 Å (right side in each panel) in the quiet Sun. Each panel presenting the average profile (solid lines) and the standard deviation (colored error bars) of profiles within every class. The vertical dotted line separates the two spectral lines. Each plot indicates the class number and the percentage of profiles assigned to that class. The classes colors represent different profile types: network (purple), blue-lobe (blue), red-lobe (red), Q-like (sky-blue), asymmetric (green), antisymmetric (yellow), and fake (orange). Image was produced by Viticchié et al. (2011).

3.2 Observations

We investigate a high signal-noise ratio deep mode data observed by the spectropolarimeter (SP; Lites et al., 2013) of the Solar Optical Telescope (SOT; Tsuneta et al., 2008; Suematsu et al., 2008; Ichimoto et al., 2008; Shimizu et al., 2008) onboard the Hinode spacecraft (Kosugi et al., 2007). Specifically, the SP data consists of four Stokes (I, Q, U and V) profiles of the Fe I lines at 6301.5 Å (effective Landé factor (g) = 1.67) and 6302.5 Å (g = 2.5), with a spectral sampling of 2.15 pm per pixel and with an exposure time of 9.6 sec. The deep mode observations were obtained in a time series measurements at a single slit position. The time series of dataset was completed in one hour and 51 minutes. The noise level of data was $8.0\times10^{-4} I_c$, where I_c is the continuum intensity of the quiet Sun.

The observational data was obtained on 2007 February 7 for a quiet Sun region at the disk center. The data were corrected for dark current, flat-field, and instrumental cross-talk by using the IDL routine **SP_PREP** (Lites et al., 2013), which is a standard calibration procedure available under the Solar SoftWare (SSW) package. In fact, this SP data has been analyzed in various contributions (Lites et al., 2007, 2008; Borrero et al., 2011b; Orozco Suárez et al., 2012a). Figure 3-2 displays the maps of normalized continuum intensity, total circular polarization (TCP) and total linear polarization (TLP) of the quiet Sun data. The TCP and TLP have been determined as

$$TCP = \frac{\int |V| d\lambda}{I_c \int d\lambda} \tag{3-1}$$

$$LCP = \frac{\int \sqrt{Q^2+U^2} d\lambda}{I_c \int d\lambda} \tag{3-2}$$

whereas the numerical integration was performed by using 21 wavelength points around the central wavelength of the Fe I 6302.5 Å absorption line.

The continuum intensity map provides a visual representation of the granulation's evolution along the x-axis. Bright fringes in the map indicate the presence of single granules, while darker areas correspond to intergranular lanes. The slit intersects a supergranular cell at the y-coordinate position of $60''$, a network patch is visible in the maps. The linear polarization map displays notable signals, thanks to the higher signal-to-noise ratio. These maps illustrate the temporal changes in internetwork magnetic

features. It is worth noting that the average size of circular polarization features in the horizontal direction (over time) is larger compared to that of the linear signals.

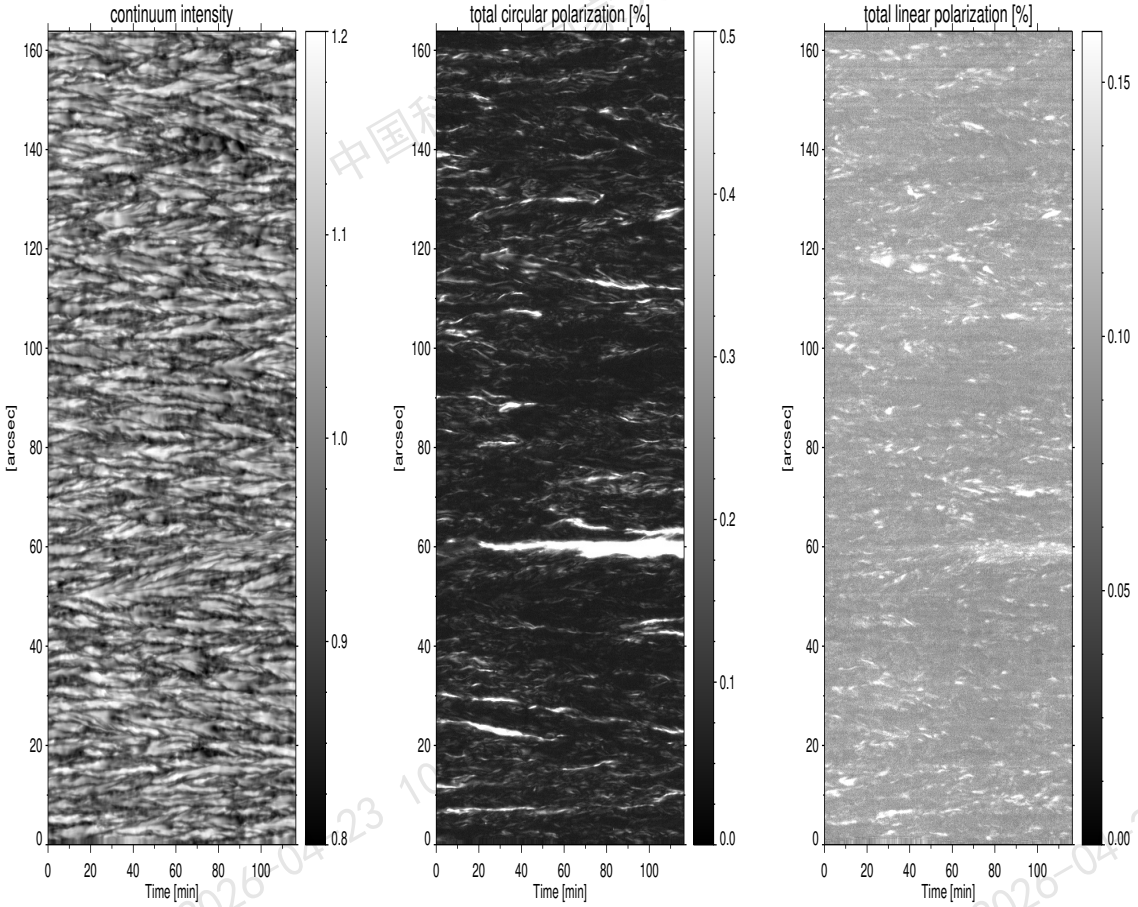

Figure 3-2 Maps of continuum normalized intensity (left), total circular polarization (middle) and total linear polarization (right) for the quiet Sun region of Hinode SOT-SP deep mode scan. The x-axis represents time series [in minutes] and the y-axis is the position along the slit [in arcsec].

The analysis of Hinode SP data involved two different integration times, similar to previous studies conducted by Lites et al. (2008) and Bellot Rubio et al. (2012). Lites et al. (2008) utilized a 1.1-minute exposure time, while Bellot Rubio et al. (2012) opted for a longer 6.1-minute exposure time. For our investigation, we examined the magnetic field vector in the quiet Sun using both 1.1 minute and 6.1 minute exposure times. We obtained an average of seven consecutive slit scan positions, revealing a noise level of $3.0 \times 10^{-4} I_c$. Additionally, by binning 38 consecutive slit scan positions, similar to Bellot Rubio et al. (2012), we achieved a lower noise level of $1.3 \times 10^{-4} I_c$. Figure 3-3 demonstrates the improvement in signal-to-noise ratio across all Stokes parameters for integration times of 9.6 seconds, 1.1 minutes, and 6.1 minutes. Notably, the less noisy

spectra (on the right) reveal polarization signals that are also present in the other panels but obscured by higher noise levels. Consequently, increasing the exposure time allows the observation of previously undetectable weak signals. 72% and 93% of pixels exhibit Stokes Q, U or V amplitudes above 4.5σ noise level of SP data for the effective exposure time 1.1 min and 6.1 min, respectively. Moreover, pixels with Stokes Q and/or U amplitudes surpassing the 4.5σ threshold account for 27% and 56% respectively, aligning well with the findings of Lites et al. (2008) and Bellot Rubio et al. (2012). In this study, we employ inversion analysis for the two integrated spectra over time intervals: 1.1 min and 6.1 min of deep mode data in the quiet Sun.

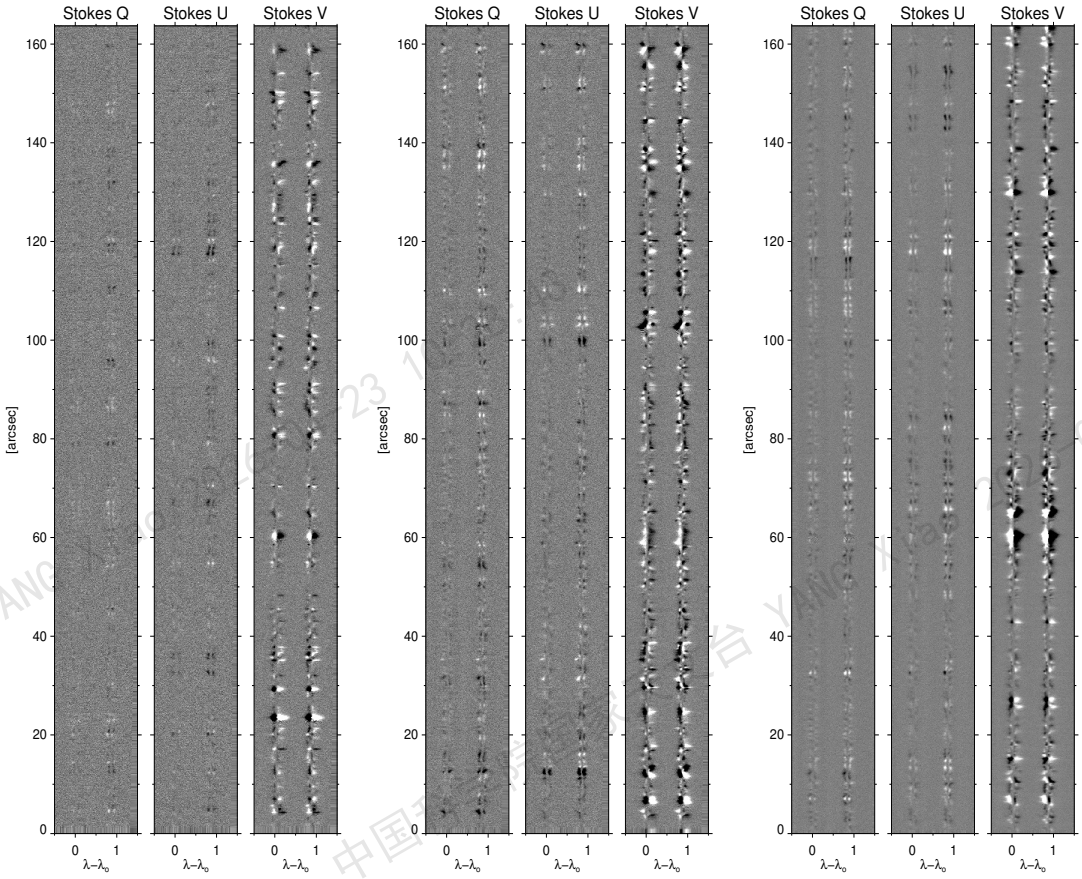

Figure 3-3 the Stokes Q, U, and V spectra captured along a single slit using three different integration times of 9.6 second (left), 1.1 minutes (middle), and 6.1 minutes (right).

3.3 Inversion strategy

The SP data was inverted with the Stokes Inversion based on Response functions (SIR; Ruiz Cobo et al., 1992) to infer the vector magnetic field of the internetwork regions. For

a case study, we adopt only a single-component model atmosphere, where the physical quantities are varied with the optical depth along the line-of-sight. In particular, the Harvard Smithsonian Reference Atmosphere (HSRA; Gingerich et al., 1971) was used as an initial guess model atmosphere for the SIR inversion. An atmospheric gradient of physical quantities was allowed to reproduce the asymmetries of observed profiles, which reveals more information about the magnetic field vector. We employed in the SIR inversion three nodes for the temperature, field strength, field inclination and the line-of-sight velocity, while the field azimuth has only two nodes. Also microturbulence and macroturbulence velocities were assumed with a single node of depth-independent parameters. In addition, the straylight was also a free parameter and the total number of free parameters is 18.

Our study focused on mitigating the impact of straylight contamination, which arises from non-magnetic elements and leads to a reduction in polarization signals. To address this issue, we took into account the local straylight profile, considering the telescope diffraction which mixes light from nearby pixels rather than far away ones. To calculate this profile, we determined the average Stokes I (total intensity) along 1″ (equivalent to 7 pixels in width and length) of the slit centered around each pixel. This approach allowed for a pixel-by-pixel variation in the straylight during the inversion process. Although our treatment of telescope diffraction simplifies the unpolarized straylight contamination, it is evident that diffraction also affects the mixing of polarization signals.

This method for treatment of straylight was previously proposed by Orozco Suárez et al. (2012a) for analyzing deep mode Hinode SP data of the quiet Sun. By incorporating the local straylight profile into the inversion process, we achieved a reliable best-fit to both the observed intensity and polarization spectra. Additionally, we assumed a one-component inversion model, where the straylight component was characterized by a single free parameter (α). The magnetic filling factor (f) was then calculated as $f = 1 - \alpha$, with α representing the fitted straylight fraction obtained from the SIR inversion. The magnetic filling factor conceptually corresponds to a multi-component atmosphere, where one component is assumed to contain an embedded magnetic field while the others do not.

3.4 Inversion results

Figure 3-4 shows maps of the magnetic field strength (B), field inclination (θ) and field azimuth (ϕ) at different optical depths of $\log \tau = [0, -0.5, -1.0]$, as retrieved from the SIR inversion of high signal-noise ratio data with an effective exposure time of 1.1 min. The inversion results reveal more reliable magnetic properties of the quiet Sun, where most of pixels exhibit more inclined magnetic fields with weak strengths in order of hG at $\log \tau = 0$. On the other hand, a few patches display strong magnetic strengths of B $\geq$1 kG with vertical orientations, such a strong field can be seen at the slit position y = $60''$ (see, Figure 3-2 and 3-4). The strong vertical fields represent the quiet sun network (Solanki et al., 1987; Sanchez Almeida et al., 1994). The retrieved field inclinations of this particular network element are close to the LOS at the center of the network patch. The field strength decreases rapidly with the optical depth and it significantly exhibits smaller field strengths (B $\approx$ 100 G) at the higher layer ($\log \tau = -1.0$). The field azimuth inferred from the inversion is mostly randomly distributed spatially and usually shows only small changes with the height. Note the small scale structures in form of $0.5'' - 1''$ parches in the azimuth map and it exhibits consistent patterns over the space and time directions.

The field inclination can not be reliably constrained when the polarization signals are extremely weak and highly contaminated by noise. As the Stokes Q or U profiles do not exhibit prominent distinctions above the noise level, the SIR inversion attempts to fit the signal noise found in the Stokes Q and U profiles (Borrero et al., 2011b). To take into account the impact of highly noise-contaminated polarization signals, we exclusively consider all pixels with Stokes Q or U amplitudes exceeding 4.5σ threshold level.

At this point, we have separated the quiet Sun internetwork, as described by Lites et al. (2017). To avoiding the strong flux concentrations of the network, we excluded the pixels in the field of view, with apparent longitudinal and/or transverse flux density exceeded 100 Mx cm^{-2} and 170 Mx cm^{-2}, respectively.

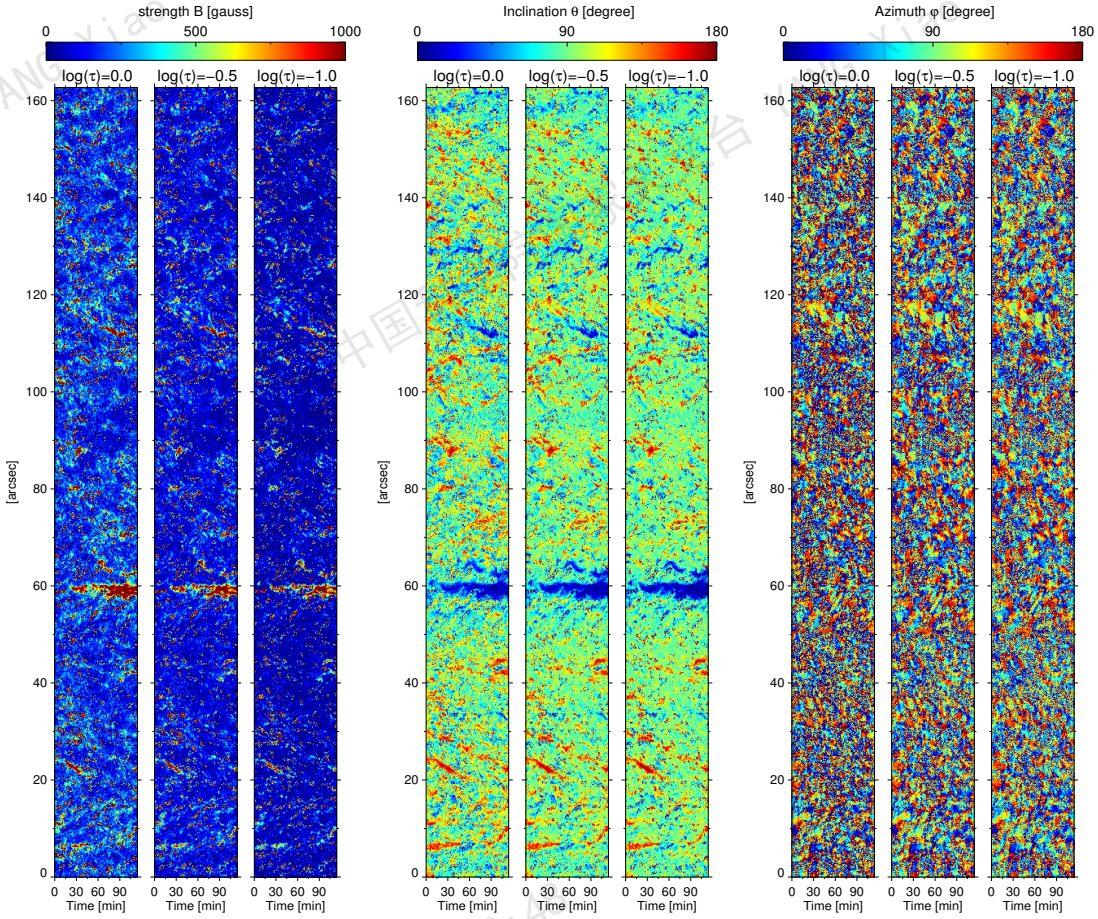

Figure 3-4 The results of SIR inversion for integrating deep mode data of effective exposure time 1.1 min. From the left to right: magnetic field strength (B), field inclination (θ) and field azimuth (ϕ). These physical parameters are presented at various optical depths of log $\tau = [0, -0.5, -1.0]$. The x-axis represents time [in minutes] and the y-axis is the position along the slit [in arcsec].

3.4.1 Fitting of Profiles

We chose a pixel in the IN for 1.1 min data, whose linear polarization signal above 4.5σ, and present the best-fit spectra as well as the inferred physical parameters from the SIR inversion (see, Figure 3-5). The best-fit spectra (black) is successfully reproduced the observed Stokes profiles (gray), as found in the first and second columns. The horizontal dashed lines indicate 4.5σ threshold level. The third and fourth columns display the field strength (top, left), field inclination (top, right), field azimuth (lower, left) and LOS velocity (lower, right) as a function of the optical depth.

At optical depth of log $\tau = 0$, the magnetic field has a values of B =124 G, field inclination $\theta = 72^{\circ}$ and field azimuth $\phi = 9^{\circ}$. In the upper photosphere (log $\tau = -1.0$), the field strength is about 92 G with $\theta = 85^{\circ}$ and $\phi = 21^{\circ}$. The atmosphere shows a high upflow velocity of V_{LOS} =-2.1 km sec^{-1} at the solar surface which decreases with

height, reaching about V_{LOS} =-0.6 km sec^{-1} at log $\tau = -1.0$.

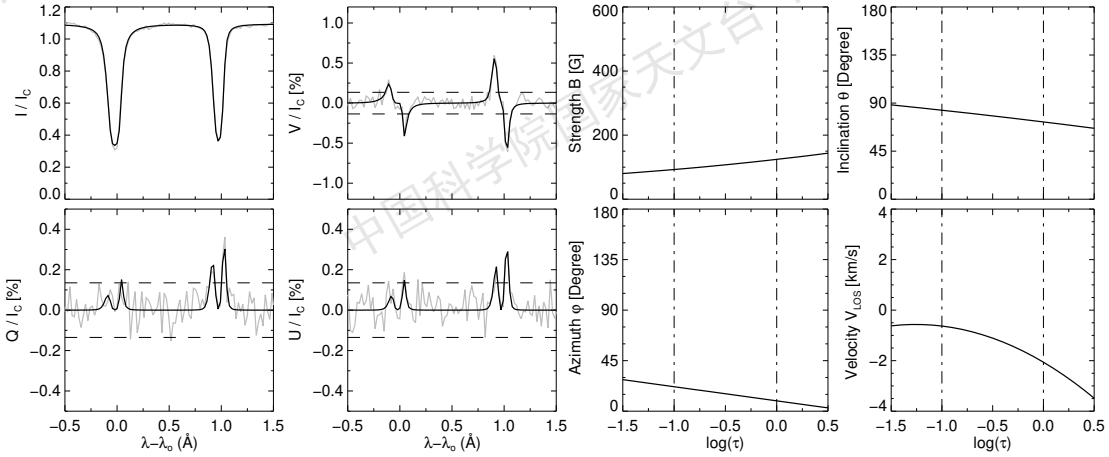

Figure 3-5 The inversion results for a pixel in the IN of 1.1 min integrated data, whose linear polarization above 4.5σ. The first and 2nd columns present the full Stokes profiles in both Fe I 6300 Å lines for the observed (gray) and inverted (black) profiles as resulting from the SIR inversion. The wavelengths are measured relative to the wavelength λ_o = 6301.5 Å. The horizontal dashed lines represent the threshold level 4.5σ. The 3rd and 4th columns display the field strength, inclination, azimuth and LOS velocity as a function of the optical depth. The two vertical dotted-dashed lines indicate the optical depth levels (log $\tau = 0$ and log $\tau = -1.0$), see the corresponding results as given in the main text.

Figure 3-6 shows the inversion results for another pixel in 6.1 min time series, which demonstrates the observed and best-fit spectra as well as the corresponding atmospheric parameters. At log $\tau = 0$, the magnetic field parameters are B =215 G, $\theta = 118^{\circ}$ and $\phi = 136^{\circ}$, while these parameters became B =89 G, $\theta = 97^{\circ}$ and $\phi = 122^{\circ}$ at log $\tau = -1.0$.

These inferences of physical quantities within an internetwork region via SIR inversion demonstrate a physically plausible depth dependence as illustrated in Figures 3-5 and 3-6 and witnessed by the good fits to all four Stokes profiles in each case.

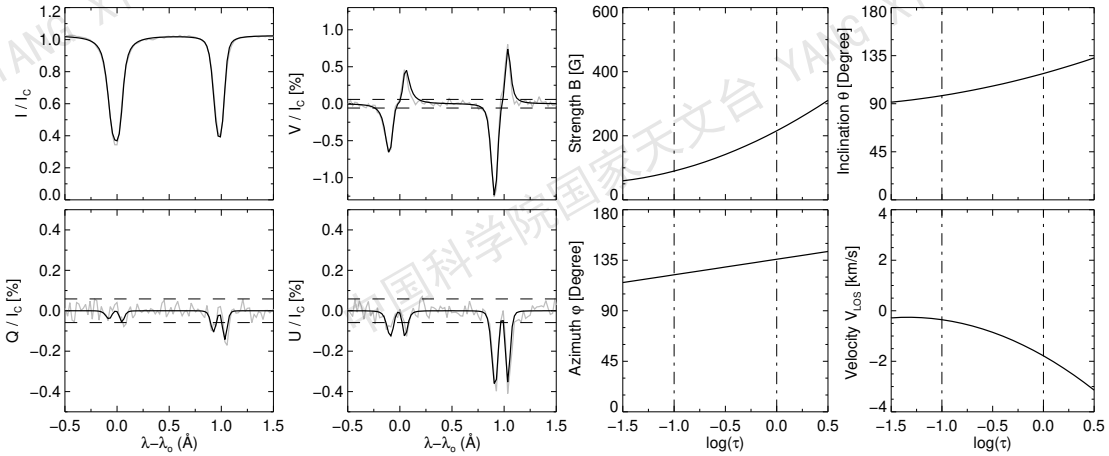

Figure 3-6 Same as figure 3-5, but the inversion results are for pixel of 6.1 min integrated data.

3.4.2 Distribution of magnetic field vector

Figure 3-7 displays the probability distribution functions (PDFs) of magnetic field strength (B) and field inclination (θ) in the IN regions. The PDFs are based on deep mode observations with effective exposure times of 1.1 min (solid line) and 6.1 min (dashed line) and are shown as a function of optical depth at $\log \tau = [0, -0.5, -1.0]$. These PDFs are derived from pixels with Stokes Q and/or U amplitudes above 4.5σ.

While the distributions of inclination for both 1.1 min and 6.1 min time series are similar at all atmospheric depths, there are noticeable differences in the distribution of magnetic field strength. For the 6.1 min integrated time series, the PDFs of field strength exhibit a different distribution, with the peak slightly shifted towards weaker fields compared to the 1.1 min integrated time series. This shift in peak strength is attributed to the reduction in polarimetric signal amplitudes as the integration time increases beyond the evolution time scale of the solar scene (2-3 min), and then a decrease in the inferred magnetic field strength was obtained (Danilovic et al., 2016). Furthermore, longer integration time, such as 6.1 min, allow some strong magnetic flux concentrations to persist in the data, resulting in a higher frequency of strong magnetic fields (Lites et al., 2017). To mitigate this effect, further analysis primarily focuses on inversion results from observational data with an integration time of 1.1 min.

The field strength distribution peaks at approximately $B = 220$ G at the solar surface, as derived from inversion of 1.1 min integrated data. Similar results were obtained from the analysis of deep photosperic infrared Fe I 15.6 μm lines (Beck et al., 2009; Martínez

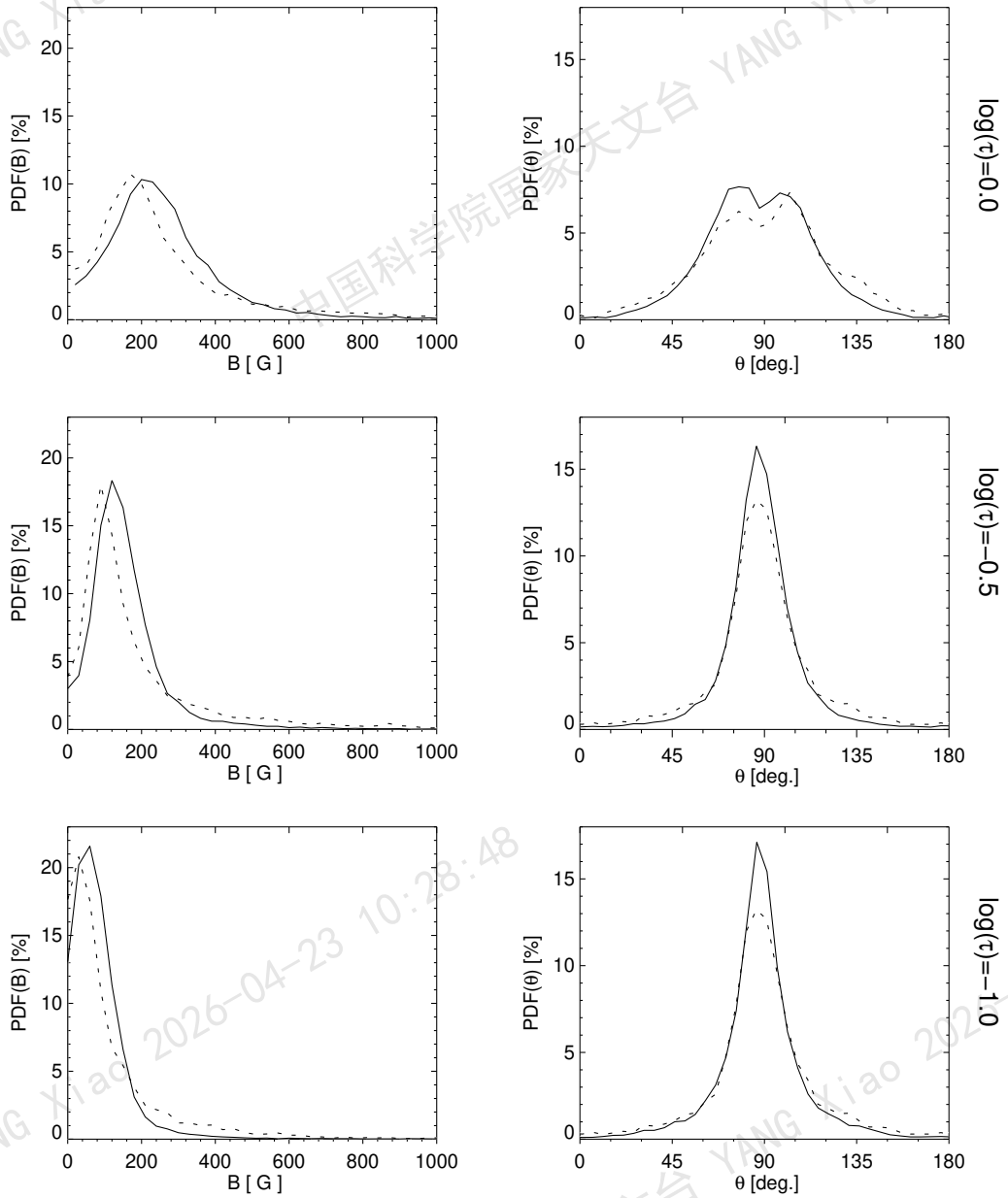

Figure 3-7 The PDFs of magnetic field parameters in the IN regions, as retrieved from the inversion of integrated high S/N time series of effective exposure time 1.1 min (solid) and 6.1 min (dashed). Left: the distribution of the magnetic field strength (B). Right: the distribution of field inclination (θ). From top to bottom, the magnetic field parameters are presented at various optical depths log $\tau = 0$, -0.5 and -1.0, respectively.

González et al., 2016). They found a peak field strength of about $B = 250$ G. It is noted that peak of field strength occur at magnetic strength slightly weaker than that obtained from the Fe I 15.6 μm lines. The distribution peak of field strength at log $\tau = -0.5$ is around $B = 100$ G, as also found by Orozco Suárez et al. (2007a), Orozco Suárez et al. (2012a) and Bellot Rubio et al. (2012).

Additionally, The inclination distribution is quasi-isotropic at the deep layer (log $\tau = 0$), consistent with the results reported by Asensio Ramos et al. (2014). However, at the upper photosphere the distributions become mainly horizontal, and in fact similar results were obtained by previous studies (Orozco Suárez et al., 2007b; Ishikawa et al., 2009; Orozco Suárez et al., 2012a; Lites et al., 2017).

We study the PDFs of the field azimuth (ϕ) and line-of-sight velocity (V_{LOS}) at various optical depths, as depicted in Figure 3-8. Positive (negative) velocities indicate downward (upward) flows in this study. The PDFs of ϕ and V_{LOS} for both 1.1 min and 6.1 min time series are similar at all atmospheric depths. We derived multiple velocity distributions and determined the average line-of-sight velocity to be $\langle V_{LOS} \rangle$ = -1.2 km sec^{-1} at log $\tau = 0$. At the upper photosphere, we measured average values of $\langle V_{LOS} \rangle$ = -0.8 km sec^{-1} and $\langle V_{LOS} \rangle$ = -0.6 km sec^{-1} at log $\tau = -0.5$ and log $\tau = -1.0$, respectively, as shown in the right panel of Figure 3-8. Notably, the velocity distributions primarily exhibited upflows in the internetwork regions, which consistent with the granulation pattern observed by Jin et al. (2009). Moreover, we observed a uniformly distributed field azimuth, which is necessary to explain the absence of Stokes U signals in Hanle-effect observations of spectral lines near the edge of the Sun's disk (Stenflo, 1982).

We conducted a detailed analysis of the PDFs for field strength, inclination, azimuth, and line-of-sight velocity across different atmospheric layers, yielding new distributions along the formation height. These findings offer a promising opportunity for a new interpretation of the magnetic field vector and flow velocity in the quiet Sun region. We obtained a reliable results consistent with other studies at a specific height, which these previous analyses were used a ME inversion of homogeneous atmosphere.

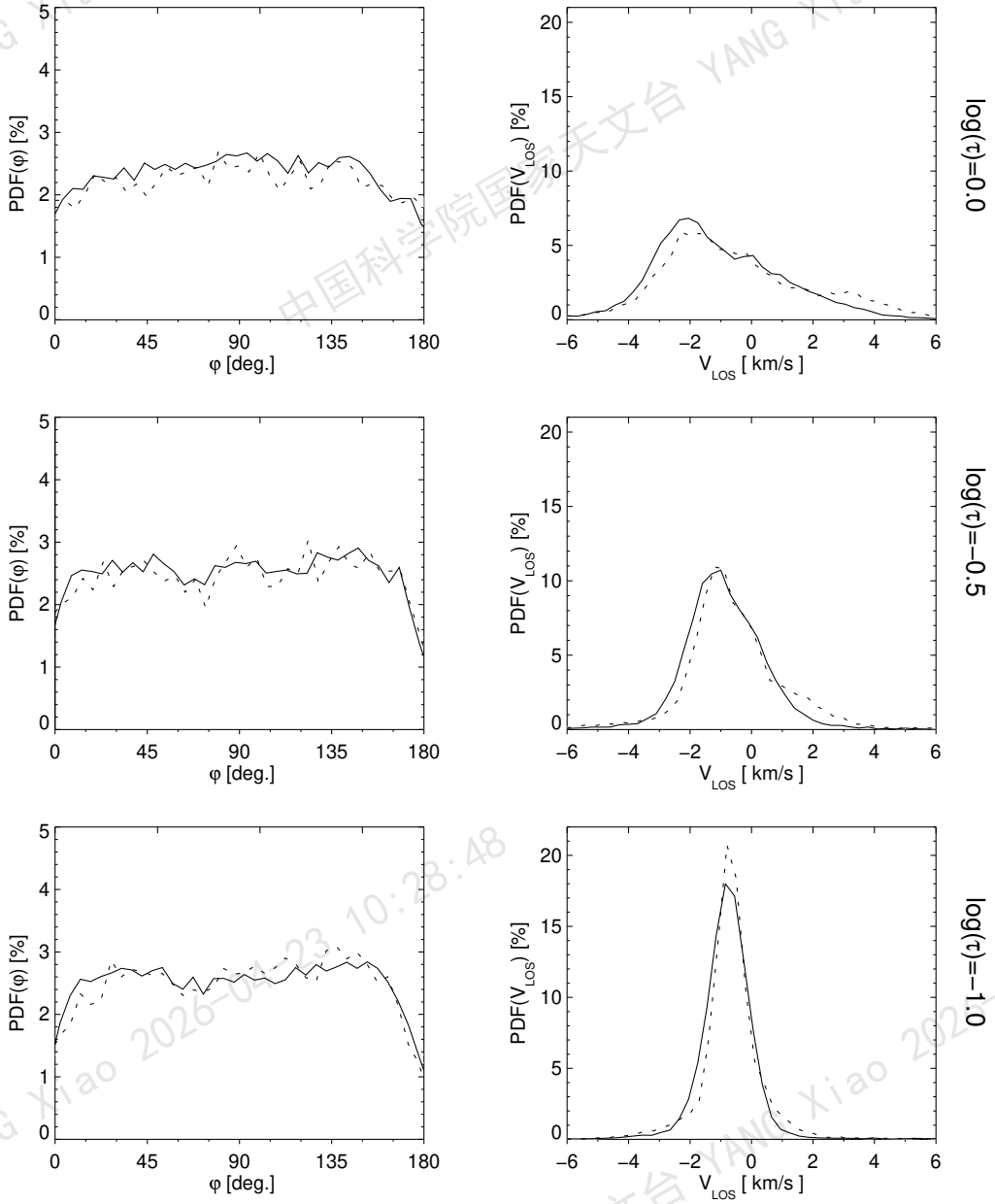

Figure 3-8 The PDFs of field azimuth (ϕ; left) and LOS velocity (V_{LOS}; right) in the IN regions, as retrieved from the inversion of integrated high S/N time series of effective exposure time 1.1 min (solid) and 6.1 min (dashed). From top to bottom, these parameters are presented at various optical depths log $\tau = 0$, -0.5 and -1.0, respectively. Positive (negative) velocities indicate downflow (upflow).

3.4.3 Correlation of field inclination with field strength and LOS velocity

The joint probability distribution functions (JPDFs; Cheung et al., 2007) depicted in Figure 3-9, provide a scientific representation of the correlation between the inclination and strength of magnetic fields as well as the inclination and LOS velocity within the IN regions at different optical depths of log $\tau = 0$, log $\tau = -0.5$ and log $\tau = -1.0$. Our analysis reveals that the IN region primarily consists of inclined magnetic fields with

strengths around several hundred Gauss at log $\tau = 0$. As we move to higher layers, these fields predominantly align horizontally with strengths of approximately B< 400 G.

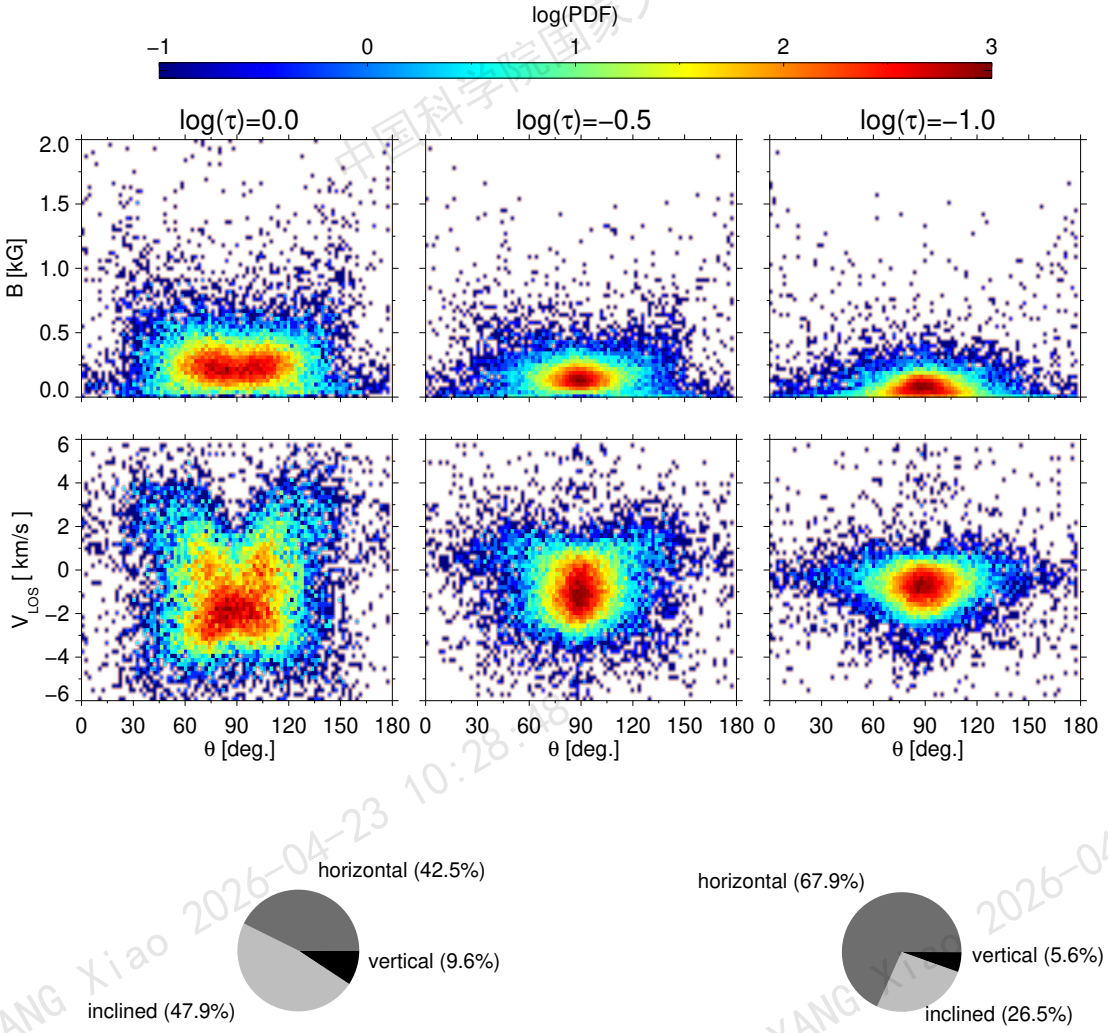

Figure 3-9 Top panel: the JPDFs between the field inclination & field strength (top) and the field inclination & LOS velocity (bottom) in IN regions at log $\tau = (0, -0.5, -1.0)$. The JPDFs present the magnetic field parameters as function of the optical depth along pixels whose Stokes Q and/or U amplitudes above threshold of 4.5σ. Bottom panel: the ratios of the vertical, inclined and horizontal fields in the IN regions at log $\tau = 0$ (left) and log $\tau = -1.0$ (right).

The horizontal fields are typically associated with negative velocities (upflow) ranging from 1.0 to 2.0 km sec^{-1}, which consists with the characteristics of granular upflow as previously reported (Jin et al., 2009). The majority of vertical fields exhibit weak strengths, typically B<250 G, and are predominantly located in intergranular lanes, which are regions of downflow. These weak horizontal and vertical fields likely repre-

sent the crests and footpoints of small magnetic loops, consistent with previous studies by Lites et al. (1996) and De Pontieu (2002). However, a small fraction of pixels exhibit strong vertical fields with strengths exceeding 500 G, similar to what has been observed in magneto-convection simulations (Vögler, 2003; Cheung et al., 2007).

Overall, our results demonstrate that the majority of pixels in IN regions correspond to weak, horizontal fields, as indicated by the linear polarization signals surpassing a 4.5σ threshold. Nevertheless, a significant proportion of pixels are associated with inclined fields, while vertical fields are less common. To further characterize the inclination properties of the magnetic fields, we classify them as vertical ($\theta \leq 45^{\circ}$ or $\theta \geq 135^{\circ}$), horizontal ($80^{\circ} \leq \theta \leq 100^{\circ}$), or inclined ($45^{\circ} < \theta < 80^{\circ}$ or $100^{\circ} < \theta < 135^{\circ}$), and the field orientation distributions are presented in the lower panel of Figure 3-9.

Our findings strongly suggest that the magnetic fields in the IN region predominantly manifest as small-scale loops and transient Horizontal Internetwork Fields (HIF), consistent with previous reports by (Lites et al., 1996, 2008; De Pontieu, 2002; Centeno et al., 2007; Jin et al., 2009; Ishikawa et al., 2010; Orozco Suárez et al., 2012b).

3.4.4 Stratification of field vector components

Figure 3-10 presents the variations of the average field strength $\langle B \rangle$, the average unsigned vertical component $\langle |B_Z| \rangle$ and the average horizontal component $\langle B_H \rangle$ as functions of the optical depth in the IN regions, as retrieved from the inversion of 1.1 min time series. These parameters were calculated as

$$\langle B \rangle = \frac{\sum_{i=1}^{N} B_i}{N} \tag{3-3}$$

$$\langle |B_z| \rangle = \frac{\sum_{i=1}^{N} |B_i \, cos\theta_i|}{N} \tag{3-4}$$

$$\langle B_H \rangle = \frac{\sum_{i=1}^{N} B_i \, sin\theta_i}{N} \tag{3-5}$$

where N is the number of pixels, using pixels with Stokes Q and/U amplitudes above 4.5 times the noise level.

The results show that the average strength of the magnetic field on the surface of Sun is 293 G. As we move higher above the surface, the field strength decreases rapidly. at $\log \tau = -0.5$ and $\log \tau = -1.0$, the mean field strengths are approximately 180 G and 104 G, respectively. The vertical and horizontal components of the magnetic field also show significant variations with height.

At $\log \tau = 0$, the values for the average vertical component $\langle |B_Z| \rangle$ and the average horizontal component $\langle B_H \rangle$ are approximately 112 G and 253 G, respectively. In the upper layers, at $\log \tau = -0.5$, the derived values for $\langle |B_Z| \rangle$ and $\langle B_H \rangle$ are 52 G and 162 G, respectively, while at $\log \tau = -1.0$, the values are 28 G and 92 G, respectively. These findings provide insights into the depth-dependent characteristics of the magnetic field in the quiet Sun region and represent new information about its magnetic properties.

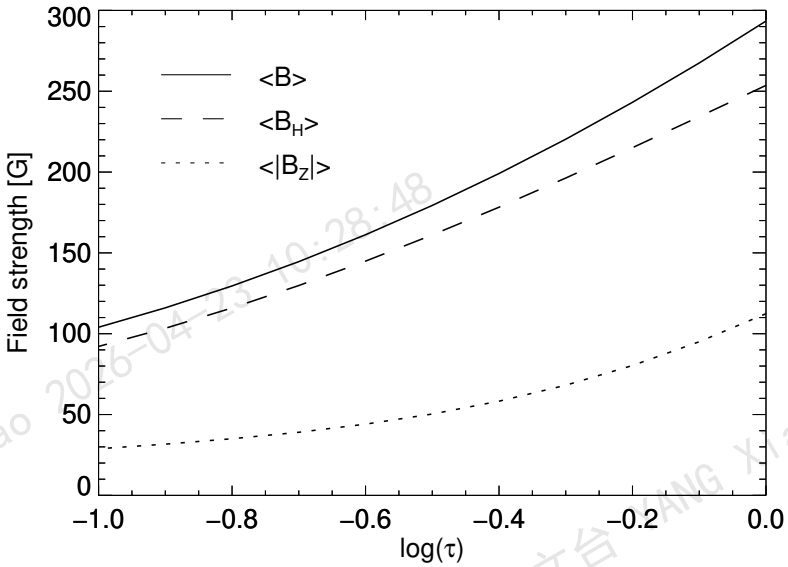

Figure 3-10 The variations of the average field strength $\langle B \rangle$ (solid), the average unsigned vertical component $\langle |B_Z| \rangle$ (dotted) and the average horizontal component $\langle B_H \rangle$ (dashed) component as a function of the optical depth in the IN regions where pixels of Stokes Q and/or U exceed threshold of 4.5σ.

We study the variation in the ratio between the horizontal and vertical components as we move from deeper to higher layers. This ratio, $\langle B_H \rangle / \langle |B_Z| \rangle$, changes from 2.2 to 3.2 at $\log \tau = 0$ and $\log \tau = -1.0$, respectively. the ratio of $\langle B_H \rangle / \langle |B_Z| \rangle$ is approximately 3.1 at $\log \tau = -0.5$, in agreement with the previous study conducted by Orozco Suárez et al. (2012a). They reported slightly higher values for $\langle B \rangle$, $\langle |B_Z| \rangle$ and $\langle B_H \rangle$, specifically 220 G, 64 G and 198 G, respectively.

Our results confirm that the average magnetic field strength in the upper photosphere exceeds 100 G, which supports the conclusions drawn from the Hanle depolarization measurements (Trujillo Bueno et al., 2004; Shchukina et al., 2011). Rempel (2014) conducted multiple simulations of magneto-convection with a small-scale dynamo effect, and the most magnetized model exhibited $\langle B \rangle = 160$ G, $\langle |B_Z| \rangle = 85$ G and $\langle B_H \rangle = 120$ at solar surface. Furthermore, del Pino Alemán et al. (2018) proposed scaling the magnetized model developed by Rempel (2014) by a factor of 3/2 to generate Hanle depolarization signals of Sr I 4607 Å. Notice that this scaled simulation closely matches our findings at $\log \tau = 0$.

3.4.5 Stratification of longitudinal and transverse flux densities

We study the average longitudinal $\langle |f B_Z| \rangle$ and transverse $\langle f B_H \rangle$ flux densities as a function of optical depth, ranging from $\log \tau = 0$ to $\log \tau = -1.0$, as illustrated in Figure 3-11. The magnetic filling factor (f) was calculated as $f = 1-\alpha$, where straylight factor (α) was obtained through the SIR inversion of the 1.1 minute time series for pixels with Stokes Q and/or U amplitudes exceeding 4.5σ.

Our results indicate that the $\langle |f B_Z| \rangle$ at the solar surface is 70 Mx cm^{-2}, while the $\langle f B_H \rangle$ is 194 Mx cm^{-2}. At $\log \tau = -0.5$, we obtained values of 26 Mx cm^{-2} and 120 Mx cm^{-2} for the longitudinal and transverse flux densities, respectively. Interestingly, our measured value of 26 Mx cm^{-2} for the longitudinal flux density at $\log \tau = -0.5$ agrees with the results of previous studies by Beck et al. (2009), Jin et al. (2009) and Orozco Suárez et al. (2012b), where they reported longitudinal flux densities of 26 Mx cm^{-2}, 28 Mx cm^{-2}, and 27 Mx cm^{-2}, respectively.

In the upper layer at $\log \tau = -1.0$, we observed longitudinal and transverse flux densities of approximately 13 Mx cm^{-2} and 66 Mx cm^{-2}, respectively, with a ratio of $\langle f B_H \rangle$ / $\langle |f B_Z| \rangle$ approximately equal to 5.1 (see Figure 3-11). Our findings are consistent with the analysis conducted by Lites et al. (2008), who also reported a ratio of around 5, although their longitudinal and transverse flux densities were slightly smaller with values of 11 Mx cm^{-2} and 55 Mx cm^{-2}, respectively.

The inferred transverse flux density of 66 Mx cm^{-2} agrees with the results obtained from the Hanle effect measurements by Trujillo Bueno et al. (2004), who measured a flux density of 60 Mx cm^{-2} in the upper layers of the photosphere. Additionally, we

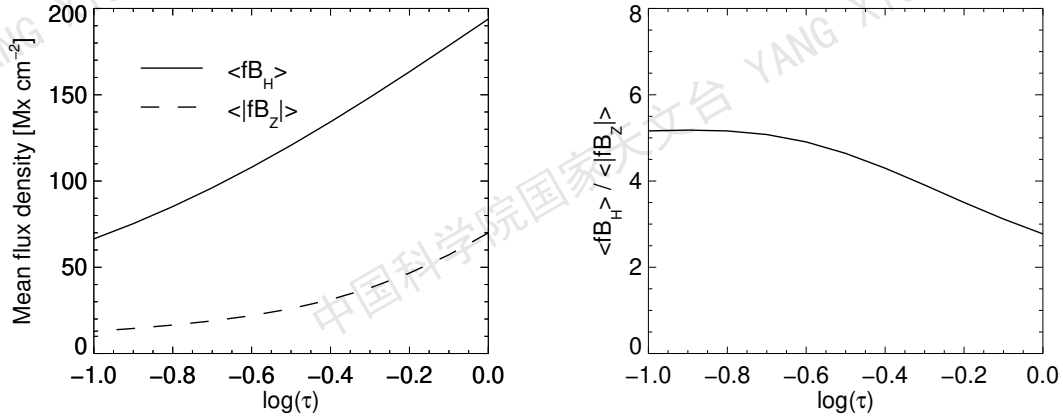

Figure 3-11 Left: The variations of the mean longitudinal $\langle |f B_Z| \rangle$ and transverse $\langle f B_H \rangle$ flux density, as functions of optical depth from log $\tau = 0$ to log $\tau = -1.0$, in the IN regions. Right: the variation of the ratio between $\langle |f B_Z| \rangle$ and $\langle f B_H \rangle$ with the height. we take into account pixels with Stokes Q and/or U amplitude above 4.5σ.

determined net longitudinal flux values of -0.4 Mx cm^{-2} and -0.7 Mx cm^{-2} at log $\tau = 0$ and log $\tau = -1.0$, respectively.

3.4.6 The Stokes V area asymmetry

We investigated the Stokes V asymmetries using the Hinode SP deep mode in internetwork regions. The asymmetry of spectral lines, referred to as δa, was calculated based on previous studies by Borrero et al. (2004), Kiess et al. (2018) and Abdelkawy et al. (2023) as follows:

$$\delta a = \frac{\int_{\lambda_a}^{\lambda_b} V(\lambda) d(\lambda)}{\int_{\lambda_a}^{\lambda_b} |V(\lambda)| d(\lambda)} \tag{3-6}$$

where the numerical integration for the Fe I 6301.5 Å line was conducted from $\lambda_a = 6301.24$ Å to $\lambda_b = 6301.67$ Å, while for the Fe I 6302.5 Å line, the integration limits were set from $\lambda_a = 6302.25$ Å to $\lambda_b = 6302.72$ Å.

The observed asymmetry in the pair of Fe I 6300 Å lines is a result of variations in the magnetic field and velocity along the line of sight. Previous studies utilizing inversion techniques with height-independent magnetic field and line-of-sight velocity failed to reproduce the observed asymmetry in Stokes V profiles. To address this issue, we employed an inversion technique that considers the gradients of the magnetic field and velocity, enabling us to derive the Stokes V asymmetries of observed profiles.

In Figure 3-12, we present the PDFs of area asymmetries for both the observed and inverted Stokes V profiles in the internetwork regions. These distributions exhibit significant variability within the range of $\delta a = [-1, 1]$. The mean observed and inverted asymmetries for both Fe I lines are close to zero but positive, with large standard deviations of approximately 49%.

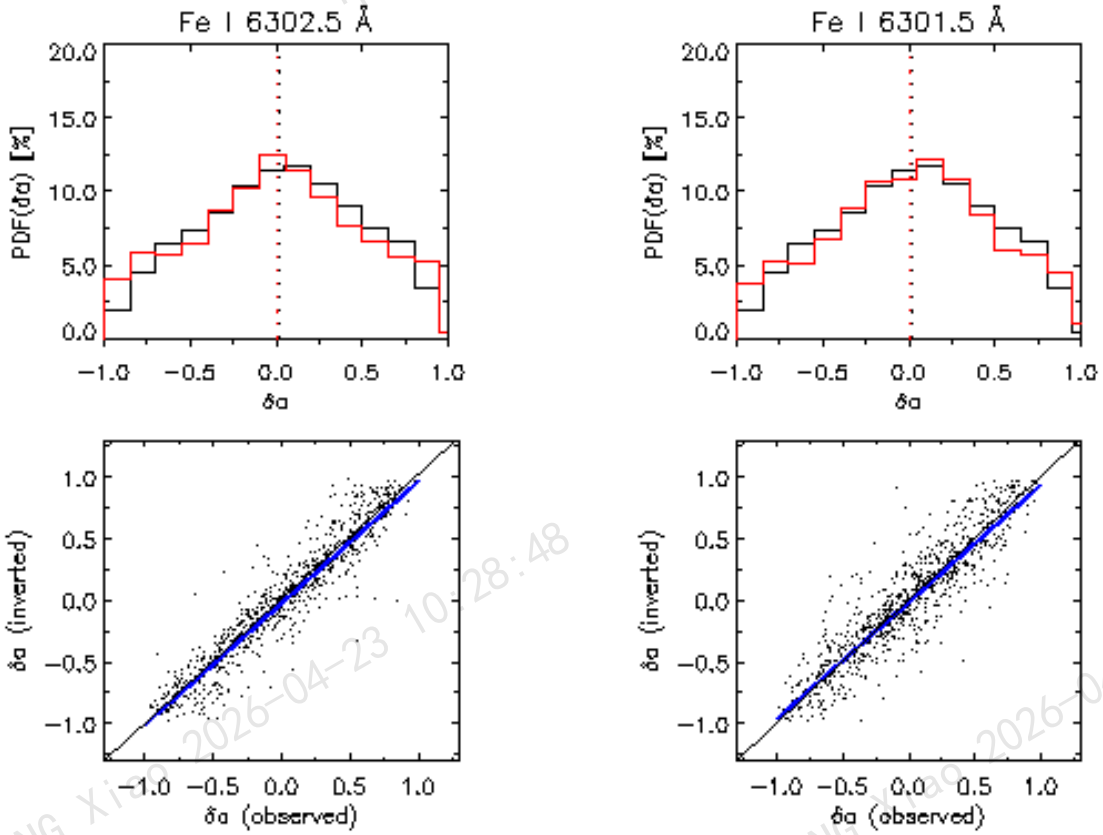

Figure 3-12 Top: The PDFs of asymmetries for the observed (black) and inverted (red) Stokes V spectra of Fe I 6302.5 Å (left) and Fe I 6301.5 Å (right) lines. the vertical dotted lines indicate the mean asymmetry for both Fe I lines. Bottom: Scatter plots of the observed and inverted asymmetries resulting for both Fe I lines. The bottom panel shows the linear fits (blue line) between the observed and inverted asymmetries in both Fe I lines.

The wide range of observed asymmetries can be attributed to the formation of the Fe I 6300 Å lines across a broad height range, where gradients in the magnetic field and velocity strongly influence the Stokes V spectra. These findings agree with the analyses conducted by Khomenko et al. (2005) and López Ariste et al. (2012). Scatter plots and linear fitting indicate a good fit between the observed and inverted asymmetries of both lines (see the bottom panel in Figure 3-12).

Overall, our results demonstrate a consistent pattern of asymmetries in the pair of Fe I 6300 Å lines. The asymmetries of spectral lines in the Hinode data are crucial for interpreting magnetic properties and plasma flows in the quiet Sun, particularly in internetwork regions. By comparing the observed and inverted asymmetry values, we can determine possible gradients in other physical parameters, which enhances our confidence in the obtained results for the magnetic field vector and LOS velocity through the SIR inversion method.

3.5 Conclusion

We conducted a detailed analysis of highly sensitive spectropolarimetric measurements obtained by the deep-mode Hinode SOT/SP. These measurements were taken with a high spatial resolution of $0.3''$ and an exposure time of 9.6 seconds in the quiet Sun near the center of the solar disk. The Hinode SP instrument has a low noise level of 8.0×10^{-4} relative to the continuum intensity (I_c).

To further enhance the quality of the data, we employed a binning technique for 7 and 38 consecutive slit positions, resulting in a reduced noise level of $3.0 \times 10^{-4} I_c$ and $1.3 \times 10^{-4} I_c$, respectively. Additionally, the effective exposure times were increased to 1.1 and 6.1 minutes, respectively, through this binning process. After analyzing the binned data, we found that 27% and 56% of the pixels exhibited linear polarization signals above 4.5 times the noise level (4.5σ) in the 1.1-minute and 6.1-minute integrated time series, respectively.

To determine the atmospheric parameters from the observational data, we utilized the SIR inversion technique with a model atmosphere that assumes gradients in atmospheric parameters along the line of sight. This inversion approach allowed us to accurately fit the asymmetries in the Stokes V profiles, which provide valuable information about the stratification of atmospheric parameters in the photosphere. We performed the inversion for both the 1.1-minute and 6.1-minute integrated datasets, considering only those pixels with Stokes Q and/or U amplitudes above 4.5σ to minimize the influence of noise on the inferred atmospheric parameters, particularly the magnetic field inclination. The scatter plot in Figure 3-12 demonstrates that the inversion code successfully reproduced the observed asymmetries.

The distributions of the magnetic field parameters obtained from the inversion of the 1.1-minute and 6.1-minute integrated observations in the internetwork region exhibited a high degree of similarity. However, some differences were observed in the distribution of field strength (refer to Figure 3-7). We noted that longer integration times, beyond the evolution period of the solar scene (1-2 minutes), resulted in a reduction of the polarization signals and inferred field strengths. Contrary to previous reports by Danilovic et al. (2016), the distribution of field strengths did not exhibit a monotonically increasing trend from stronger to weaker fields. Instead, it displayed a peak in the hG range, as noted by Orozco Suárez et al. (2007a).

The probability distribution function of the field inclination was found to be quasi-isotropic at the solar surface and predominantly horizontal in the upper layers, consistent with the findings of Lites et al. (2017). The results obtained from a Milne-Eddington approach, which represent average values over the formation region, were in agreement with our study at the mid-photosphere of $\log \tau = -0.5$ (e.g., Orozco Suárez et al., 2007a, 2012a; Bellot Rubio et al., 2012).

The mean longitudinal flux density, $\langle |f B_Z| \rangle$, and transverse flux density, $\langle f B_H \rangle$, were determined to be 13 and 66 Mx cm^{-2} at $\log \tau = -1.0$, respectively, with a ratio of $\langle f B_H \rangle / \langle |f B_Z| \rangle$ approximately equal to 5.1. This ratio was also observed by Lites et al. (2008) who reported apparent longitudinal and transverse flux densities of approximately 11 and 55 Mx cm^{-2}, respectively. The average magnetic field strength ($\langle B \rangle$) was found to be 293 and 104 G at $\log \tau = 0$ and $\log \tau = -1.0$, respectively. These findings are consistent with studies based on the Hanle effect (Trujillo Bueno et al., 2004; Shchukina et al., 2011), which indicated a mean magnetic field strength greater than 100 G in the upper photosphere.

Chapter 4 Synthesis of the Mg I 12.32 μm line from a 3D simulation of quiet Sun network

4.1 Introduction

In solar physics, magnetic fields wield significant influence across various solar phenomena. Infrared Stokes polarimetry has emerged as a valuable tool for precise magnetic field determination, given the heightened magnetic sensitivity of infrared solar lines. Instruments like the Cryogenic Infrared Spectrograph (Cao et al., 2010) at the Big Bear Solar Observatory and the Cryogenic Near-Infrared SpectroPolarimeter (Woeger, 2016) at the Daniel K. Inouye Solar Telescope have been engineered to measure solar magnetic fields within the 1–5μm infrared spectrum, showcasing a special focus on the magnetic sensitivity of the Mg I emission lines at 12 μm.

The emission line of Mg I at 12.32 μm showcase exceptional characteristics, boasting a heightened sensitivity to magnetic fields, thus playing a pivotal role in solar physics investigations. This infrared line stand out for its substantial Zeeman split-to-Doppler broadening ratio, showcasing the most substantial Zeeman split ever documented in the solar spectrum. The Mg I 12.32 μm line was initially uncovered by Murcray et al. (1981), and then it was later recognized by Chang et al. (1983) as transitions occurring between high Rydberg levels within the Mg I atom.

Observations of the Mg I 12.32 μm line have unveiled intriguing attributes. Typically, this line exhibit both an emission peak and an absorption trough at the center of the solar disk. Notably, at the solar limb, the absorption trough diminishes, while the emission peak intensifies, manifesting distinct Zeeman splitting even when subjected to weak magnetic fields (Brault et al., 1983). The Mg I line are notably present in sunspot penumbrae and plages but conspicuously absent in sunspot umbrae (Zirin et al., 1989; Moran et al., 2007; Li et al., 2021).

The formation of the Mg I 12.32 μm line was scrutinized by Carlsson et al. (1992), revealing its origin in the upper photosphere. By assuming nonlocal thermodynamic equilibrium (NLTE), synthesized line profiles aligned closely with observational data. Furthermore, investigations by Bruls et al. (1995) highlighted the sensitivity of this line

to magnetic fields in sunspots and plages.

Previous studies have primarily focused on synthesizing the Mg I 12.32 μm line utilizing 1D atmospheric models (e.g., Hong et al., 2020; Li et al., 2021), neglecting the potential insights that 3D atmospheric models could offer. Such examinations are crucial for comprehending and interpreting observations made by modern solar telescopes operating within the infrared spectrum, such as the Infrared System for the Accurate Measurement of Solar Magnetic Field (AIMS; Deng et al., 2016).

In this chapter, we have generated synthetic Stokes profiles of the Mg I 12.32 μm line using a 3D magnetohydrodynamic (MHD) model. By simulating observational profiles at various spatial resolutions, we have provided invaluable insights for the advancement of future solar telescopes. Moreover we studied the validity of different methods for extracting the magnetic field. Three primary methods exist for deriving magnetic fields, each with its challenges and advantages. Direct calculation from Zeeman splitting may be hindered when components aren't fully separated, thus necessitating alternate approaches like the weak field approximation and the inversion of magnetic fields from Stokes profiles based on radiative transfer theory.

4.2 Magnetohydrodynamic simulation

The simulation discussed here was conducted using the three-dimensional radiation magnetohydrodynamic (RMHD) code Bifrost, renowned for its adaptability and scalability. Detailed in Gudiksen et al. (2011), Bifrost operates by solving magnetohydrodynamic equations on a staggered grid employing a 5th/6th order compact finite difference technique. This versatile tool accounts for radiation effects in the energy balance by addressing radiative transfer equations along rays throughout the computational domain using a short-characteristic approach and multi-group opacities, as outlined in Nordlund (1982) with adaptations for scattering effects (Skartlien, 2000). For a comprehensive understanding of radiative transfer treatment, refer to Hayek et al. (2010).

We utilized a 3D MHD simulation that depicts an enhanced network area characterized by two opposite magnetic polarities (Carlsson et al., 2016). This simulation consists of multiple snapshots, with a specific focus on snapshot 385, corresponding to a simulation time of 3850 seconds. The simulation covers a horizontal domain of 24×24 Mm, with a consistent grid spacing of 48 km, comprising 504×504 grid cells. Vertically, the

simulation extends from the upper convection zone at -2.4 Mm to the corona at 14.4 Mm. The reference point $z = 0$ aligns with the average height in the simulation where optical depth is unity at 500 nm. The vertical grid spacing varies, with 19 km within the range of -1 Mm $< z < 5$ Mm, gradually increasing to around 100 km at the upper boundary.

This simulation employs an extensive array of physical principles and mathematical formulations to precisely replicate the behavior of plasma within the sun's atmosphere. With its capacity for high-definition simulations, it facilitates the examination of intricate patterns and movements on a fine scale. The precision of its spatial layout is paramount for capturing the elaborate intricacies of magnetic field configurations and plasma activities. This specific simulation has served as a cornerstone in various research endeavors, aiding in the synthesis of diverse spectral lines like Mg II h&k (Leenaarts et al., 2013), Ca II 8542 Å (Quintero Noda et al., 2016), Lyman β, and O I 1027 & 1028 Å (Hasegawa et al., 2020), contributing significantly to the advancement of solar physics.

The physical parameters provided by the MHD simulation are summarized as follow: temperature T (K), velocity components $V_{x,y,z}$ ($m\,s^{-1}$), magnetic field components $B_{x,y,z}$ ($T = 10^4$ G), electron density n_e (m^{-3}), gas pressure P_g ($N\,m^{-2}$), density ρ (kg m^{-3}) and hydrogen populations n (m^{-3}). Figure 4-1 illustrates horizontal slices of temperature (T), longitudinal (B_l), and horizontal ($B_H = \sqrt{B_x^2 + B_y^2}$) components of magnetic field as captured in the Bifrost snapshot at two distinct geometrical heights ($z = 0$ km and 450 km).

At the surface level $z = 0$ km (left column), the temperature mapping showcases a distinct granular layout, with wider granules exhibiting higher temperatures compared to the narrower intergranular spaces. The magnetic fields are predominantly oriented vertically, clustering within the intergranular regions due to convective movements and field buoyancy. As we ascend to higher altitudes $z = 450$ km (right column), a phenomenon known as reverse granulation emerges: the granules start to cool relative to the intergranular areas at the same height. Furthermore, the magnetic field strength diminishes, shifting towards a more horizontal alignment. These alterations stem from decreased gas pressure and the magnetic field's expansion within the upper atmosphere, marking a pivotal transition in atmospheric dynamics and magnetic field behavior.

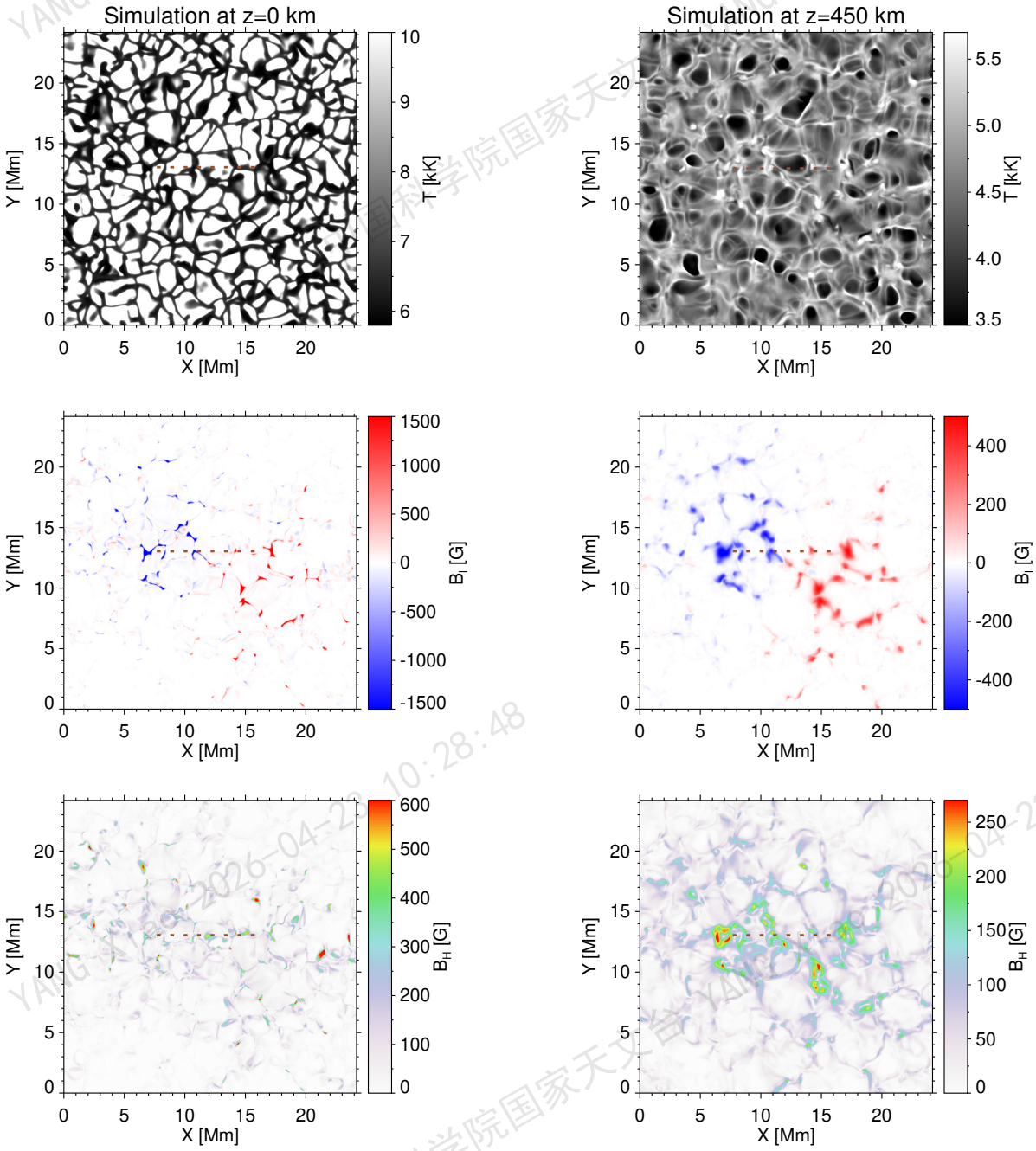

Figure 4-1 Horizontal cross sections of MHD simulation at two different geometrical heights z=0 km (left) and z=450 km (right). From top to bottom: Temperature (T), longitudinal (B_l) and horizontal (B_H) components of the magnetic field. Brown dotted lines indicate a zone that will be examined further in section 4.4.

4.3 Spectral synthesis of Stokes profiles

We utilized the Rybicki–Hummer (RH) code (Uitenbroek, 2001; Pereira et al., 2015) to synthesize the Stokes profiles of the Mg I 12.32 μm line for a line of sight charac-

terized by $\mu = 1$ (where $\mu = cos\theta$, with θ representing the heliocentric angle). The RH code stands as a pivotal tool in astrophysics for solving intricate radiative transfer equations, offering a robust framework for understanding the propagation of radiation through various mediums. Moreover, this code has been extensively utilized in numerous studies across astrophysics, shedding light on fundamental processes such as stellar atmospheres, spectral line formation, and the interaction of radiation with matter in stellar environments.

The synthesis of Stokes profiles was carried out using the vertical domain of the 3D Bifrost model spanning the height range from −0.5 to 1.2 Mm. This specific range was selected due to the Mg I 12.32 μm line's sensitivity in the photosphere and lower chromosphere, as well as to optimize computational efficiency. Each vertical slice of the model was treated as an independent 1D atmosphere, effectively representing a plane-parallel atmosphere (referred to as the 1.5D approximation).

The atomic model utilized, MgI_66.atom, was adapted from the model in Carlsson et al. (1992) and incorporated into the RH code package. Updates to the energy levels were based on the analysis by Kaufman et al. (1991), while the oscillator strength of the Mg I 12.32 μm line was calibrated to match the value reported by Zhao et al. (1998). This atomic structure encompasses 315 line transitions and 65 bound-free transitions originating from 66 levels, including the fundamental level of Mg II. Initially identified by Chang et al. (1983), the Mg I 12.32 μm line depicts a transition between highly excited states of Mg I $3s7i^{1,3}I \longrightarrow 3s6h^{1,3}H^o$. The Landé g factor for the Mg I 12.32 μm line, denoting its sensitivity to magnetic fields, is unity, as indicated by studies conducted by Chang (1987) and Lemoine et al. (1988).

4.4 Formation height

Figure 4-2 illustrates the vertical cross sections of the Bifrost atmosphere, corresponding to the dashed brown line in Figure 4-1. Our observations revealed that the B_l (middle panel) displayed a concentrated distribution in the lower photosphere within the flux tubes. However, it expanded in the higher atmospheric layers, where the B_H component took precedence. To ascertain the formation height, we computed the height at which the optical depth reaches unity for the core of the Mg I 12.32 μm line.

We notice that the formation height varied across the chosen section, particularly in regions housing moderate to strong vertical magnetic field zones, where the formation height peaked at 340 and 160 km, respectively. In these areas, the optical depth shifted towards lower geometric heights, a phenomenon commonly known as the Wilson depression. On the whole, the average formation height of the Mg I 12.32 μm line was determined to be 450 km in the upper photosphere. These results align with prior investigations based on 1D semi-empirical atmospheric models (Carlsson et al., 1992; Li et al., 2021), underscoring the consistency of our findings with existing literature.

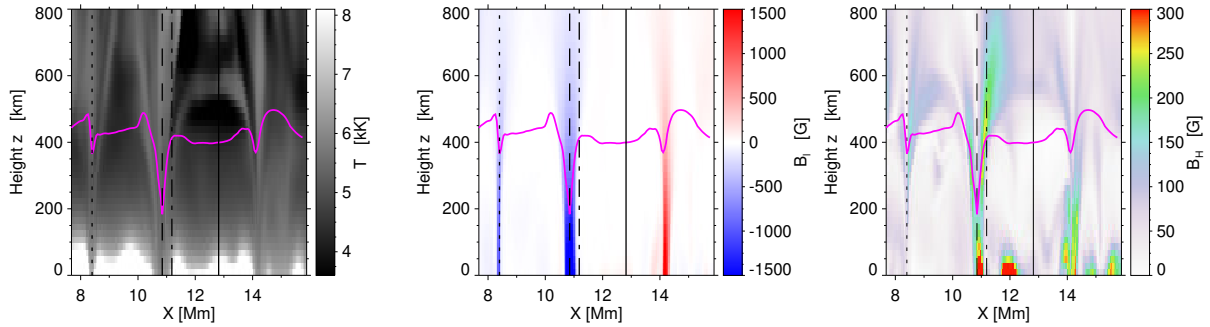

Figure 4-2 Maps of vertical slices Showing Temperature (T; Left), Longitudinal Field (B_l; middle), and Horizontal Field (B_H; right) Profiles, Corresponding to the dashed brown line in Figure 4-1. magenta lines indicate the heights of optical depth $\tau = 1$ for the core of the Mg I 12.32 μm line. The vertical lines represent the four atmospheric columns subjected to detailed analysis.

4.5 Stokes I and V profiles at various features

We investigated the characteristics of synthetic Stokes I and V profiles generated by the RH code at various spatial positions. In Figure 4-2, four pixels are identified along vertical lines, representing two magnetic concentrations (comprising strong and moderate field strengths), the boundary of a magnetic concentration, and a region with weak magnetic fields. Figure 4-3 illustrates the synthetic Stokes I and V profiles alongside the vertical distribution of temperature and magnetic field strength for these selected pixels, with each row corresponding to a distinct pixel.

In the initial two rows, corresponding to the centers of the magnetic concentrations, the intensity profiles distinctly show Zeeman splitting. The Stokes I splitting is more pronounced in the strong magnetic concentration (first row) compared to the relatively weaker one (second row). The broader line profile in the first row compared to the

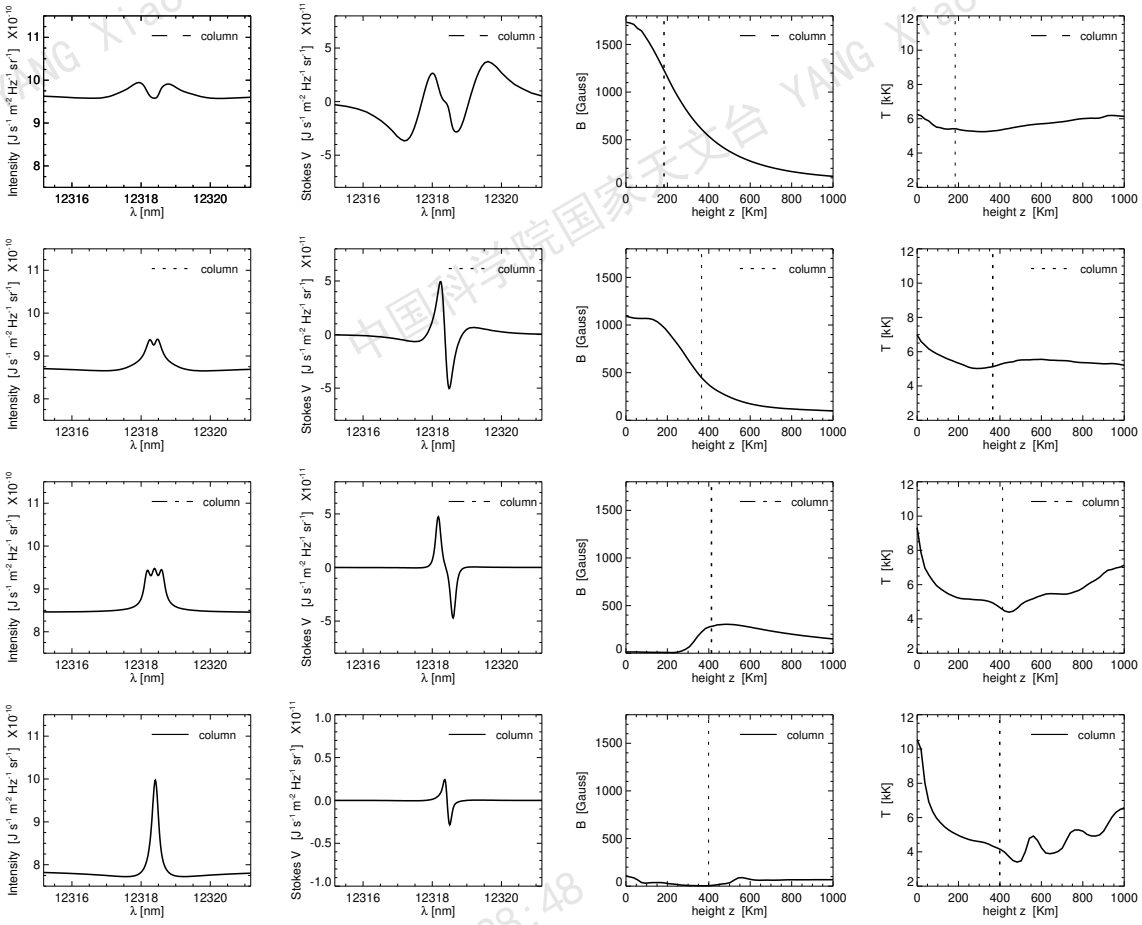

Figure 4-3 Synthetic Stokes I profiles (first column) and Stokes V profiles (second column), along with the vertical distribution of magnetic field strength (B; third column) and temperature (T; fourth column) for the four vertical atmospheric columns. The line style at the top of each panel represents the respective atmosphere, as seen in Figure 4-2. The vertical dotted line in the third and fourth columns indicates the formation height at optical depth $\tau = 1$, as marked by magneta line in Figure 4-2.

second row can be attributed to two factors: the formation of the Mg I 12.32 μm line at a lower height within the strong magnetic concentration's core and the shallower temperature gradient.

The third row exhibits the Stokes I profile for a region situated at the edge of the magnetic concentration, where the magnetic field transitions to a more horizontal orientation. This profile displays two σ components and one π component, accompanied by noticeable absorption troughs. The synthetic Stokes I profiles at the core and periphery of the magnetic concentrations align with observations of strong magnetic field solar features (Hewagama et al., 1993; Zirin et al., 1989; Moran et al., 2000). In the weak field region (fourth row), the Stokes I profile features an emission peak flanked by broad absorption troughs, consistent with quiet-Sun observations and numerical simulations based on

semi-empirical atmospheric models (Carlsson et al., 1992; Zhao et al., 1998; Li et al., 2021).

Notably, within the magnetic concentrations, the Stokes I profiles exhibit the highest continuum intensity, with intensity enhancements near the magnetic concentration regions (bright points), as seen in the top panel of Figure 4-4. The second column of Figure 4-3 demonstrates that the synthetic Stokes V profiles exhibit distinctive splitting and absorption trough characteristics, which become less pronounced as the magnetic field weakens. Interestingly, some Stokes V profiles in our simulations display four lobes, primarily observed at the centers of strong magnetic concentrations, consistent with findings in solar flares from both observations and simulations (Jennings et al., 2002; Hong et al., 2020). Additionally, the Mg I 12.32 μm line predominantly forms at heights near the temperature minimum, evident from the vertical temperature distribution in the fourth column of Figure 4-3.

4.6 Inferring magnetic field components

When the Zeeman triple components are not fully resolved, determining the magnetic field strength directly from Stokes I using the Zeeman-splitting formula becomes challenging. In such cases, polarization spectra are essential for accurate inference. The presence of incomplete separation of Zeeman components underscores the necessity of leveraging polarization information to unravel the intricate details of the magnetic field's strength and configuration.

4.6.1 Wavelength-integrated method

The wavelength-integrated method provides a comprehensive approach to deducing magnetic field components (B_l and B_H) from Stokes profiles. By integrating the spectral line over its entire wavelength range, this method captures the collective influence of all magnetic field strengths along the line of sight and perpendicular it. However, We conducted an integration of the synthetic Stokes profiles, leading to the computation of the mean circular polarization degree (MCPD) and mean linear polarization degree (MLPD), as reported by Sainz Dalda et al. (2012):

$$MCPD = \left(\int_{\lambda_a}^{\lambda_b} \frac{|V(\lambda)|}{I(\lambda)} d(\lambda) \right) / (\lambda_b - \lambda_a) \tag{4-1}$$

$$MLPD = \left(\int_{\lambda_a}^{\lambda_b} \frac{\sqrt{Q^2(\lambda) + U^2(\lambda)}}{I(\lambda)} d(\lambda) \right) / (\lambda_b - \lambda_a), \tag{4-2}$$

where the numerical integration is carried out within the range of wavelengths from $\lambda_a = 12315.182$ nm to $\lambda_b = 12321.169$ nm.

The MCPD and MLPD are important in evaluating the magnetic field strength at the specific formation height of the spectral line, presenting valuable diagnostic tools for magnetic field analysis.

Fig. 4-4 illustrates maps showcasing the integrated intensity, MCPD, and MLPD. A comparison between the right column in Figure 4-1 and Figure 4-4 reveals that the integrated intensity map mirrors the temperature distribution at a geometrical height of $z = 450$ km, displaying a distinct reverse granulation pattern where granular regions appear cooler than the intergranular lanes. Notably, the integrated intensity map reveals bright points corresponding to concentrated magnetic flux areas exhibiting strong vertical magnetic fields.

The MCPD and MLPD maps demonstrate a notable correlation with the B_l and B_H components of the magnetic field, respectively, at $z = 450$ km. Regions with elevated MCPD values align with the core of intense magnetic flux concentrations, indicative of strong vertical magnetic fields. Conversely, areas with heightened MLPD values are situated at the peripheries of flux concentrations, where magnetic field lines incline and disperse outward from the flux tube with increasing altitude. These findings decisively indicate that the formation height of the Mg I 12.32 μm line lies within the 450 km range in the Bifrost simulation, solidifying our understanding of the magnetic field dynamics within this specific atmospheric layer.

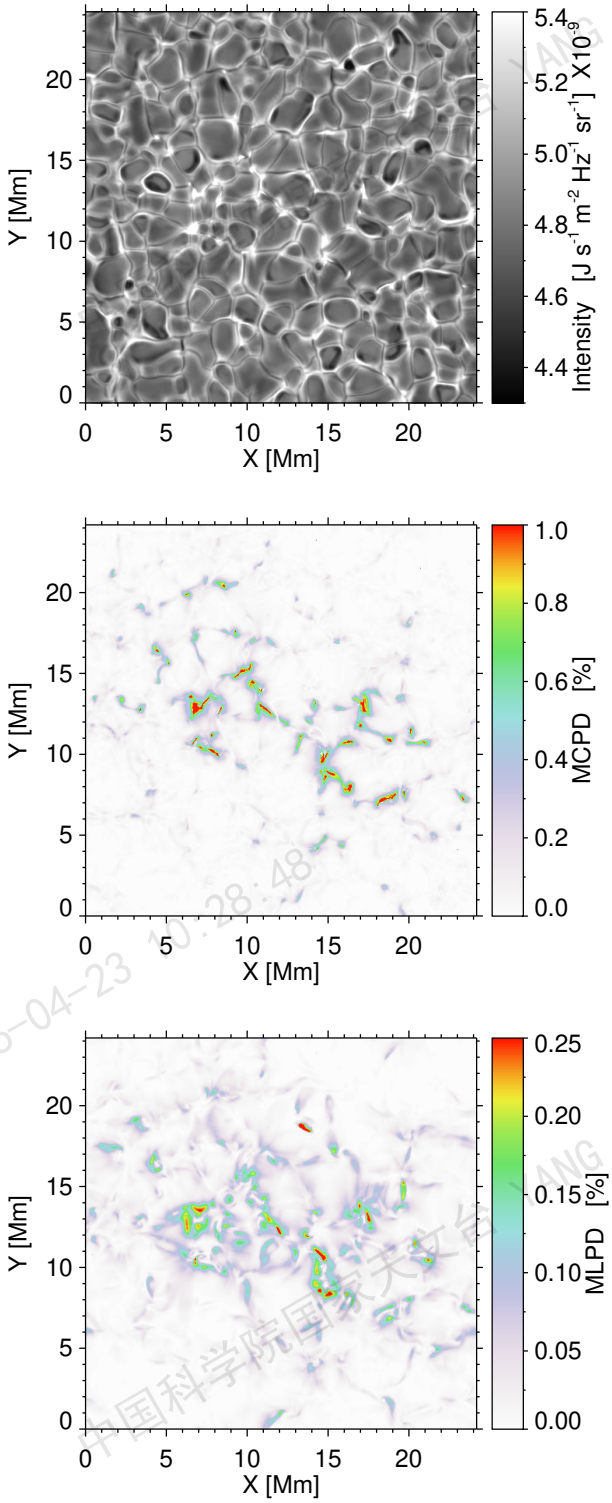

Figure 4-4 Maps of integrated intensity (top), MCPD (middle), and MLPD (bottom) for the synthetic profiles of the Mg I 12.32 μm line.

Figure 4-5 illustrates the relationship between the MCPD and B_l in the left panel, and between the MLPD and B_H in the right panel, derived from the simulation model at a geometrical height of $z = 450$ km. These associations can be viewed as a means of

converting the MCPD (MLPD) values into corresponding B_l (B_H) measurements. A linear correlation is observed between the MCPD and B_l within the range of $0-300$ G, while the MLPD and B_H exhibit linearity across the entire B_H range of $0-325$ G. In terms of the MCPD and B_l relationship, the scatter plots reveal a wider dispersion for B_l values exceeding 150 G, indicating a higher error in the linear calibration method due to the unvalidated of this method for strong fields. These results align with those reported by Li et al. (2021) using a 1D model atmosphere, endorsing the efficacy of the wavelength-integrated method for calibrating B_l and B_H, particularly when $B_l < 300$ G and $B_H < 500$ G. However, owing to limitations in the simulation model, the highest B_H recorded at the formation height of 450 km is 325 G, preventing the determination of the saturation limit of B_H through this approach.

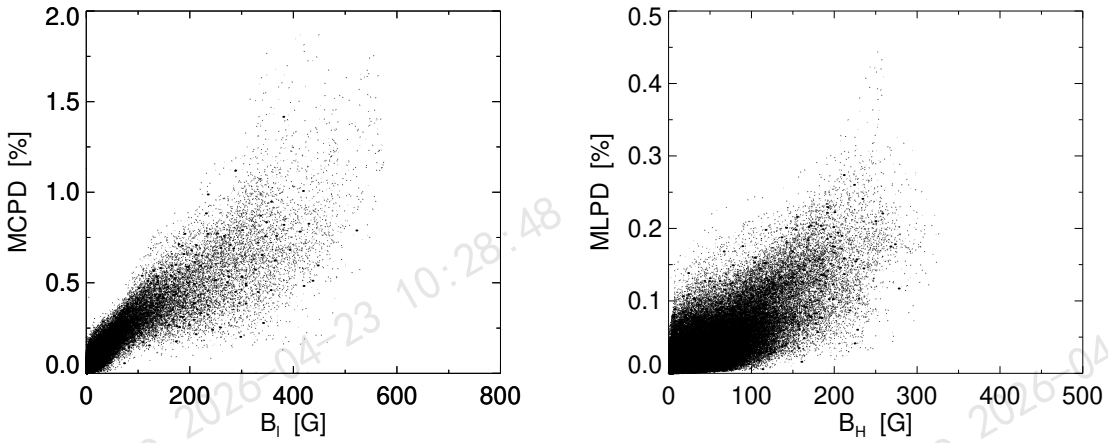

Figure 4-5 Scatter plots of MCPD (left panel) and MLPD (right panel) as a function of the B_l and B_H of the simulation model, respectively, at a height of 450 km.

4.6.2 Weak field approximation method

The Zeeman effect refers to the splitting of spectral lines in the presence of a magnetic field. This splitting, denoted as ($\Delta\lambda_B$), occurs when the magnetic field interacts with the quantum properties of the atoms or molecules emitting the light. When ($\Delta\lambda_B$) is significantly smaller than the natural width of the spectral line, represented as $\Delta\lambda_D$, it indicates a scenario where the influence of the magnetic field is relatively weak compared to other broadening mechanisms. In such cases, the Weak Field Approximation (WFA) method can be utilized to effectively determine the line-of-sight component of the magnetic field vector(B_{LOS}).

By substituting Equation 1-5 in Equation 1-7, we can derive B_{LOS} from the Stokes V profiles (e.g., Landi Degl'Innocenti, 1992)

$$V(\lambda) = -CB_{LOS}\frac{\partial I(\lambda)}{\partial \lambda} \tag{4-3}$$

where $B_{LOS} = Bcos\theta$ and the constant, C, is determined by the effective Landé factor ($\bar{g}$) and the central wavelength (λ_o) of the spectral line in as: $C = 4.6686 \times 10^{-13}\bar{g}\lambda_o^2$. According to the findings of Martínez González et al. (2009), conducting a linear least squares fit of both sides of Equation 4-3 enables the derivation of the B_{LOS} from the Stokes I and Stokes V spectral profiles:

$$B_{LOS} = -\frac{\sum_\lambda \frac{\partial I(\lambda)}{\partial \lambda} V(\lambda)}{C\sum_\lambda \left(\frac{\partial I(\lambda)}{\partial \lambda}\right)^2} \tag{4-4}$$

The syntheses of the spectral profiles were performed at disk center ($\mu = 1$), so $B_{LOS} = B_l$. The process of linear regression encompassed the entirety of the wavelength spectrum within the Stokes profiles, spanning from 12315.182 nm to 12321.169 nm. Figure 4-6 depicts the B_l derived through the WFA method in the left panel, alongside the actual magnetic field from the MHD simulation at geometrical height of 450 km in the right panel.

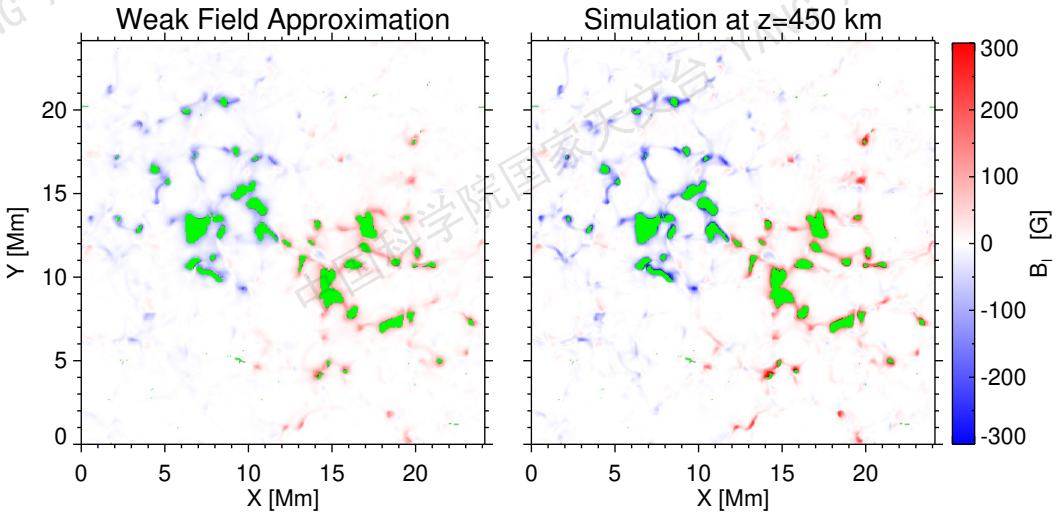

Figure 4-6 Maps of B_l as derived from the WFA method (left panel) and MHD simulation at a height of 450 km (right panel). Green regions mark the excluded pixels whose Stokes I profiles exhibit Zeeman splitting.

Remarkable similarities are observed between the maps of the B_l obtained via the WFA technique and the magnetic field values from the simulation. Additionally, a comparison was made between the B_l values in the simulation model and those calculated using the WFA method, as illustrated in Figure 4-7. Notably, for B_l values below 150 G, the WFA derived values exhibit greater accuracy and closely align with the model results. This consistency is supported by the relationship between the MCPD and B_l shown in Figure 4-5. This assessment underscores the utility of the WFA approach in interpreting observations made by instruments like AIMS and forthcoming mid-infrared solar telescopes focused on quiet-Sun regions of weak magnetic fields.

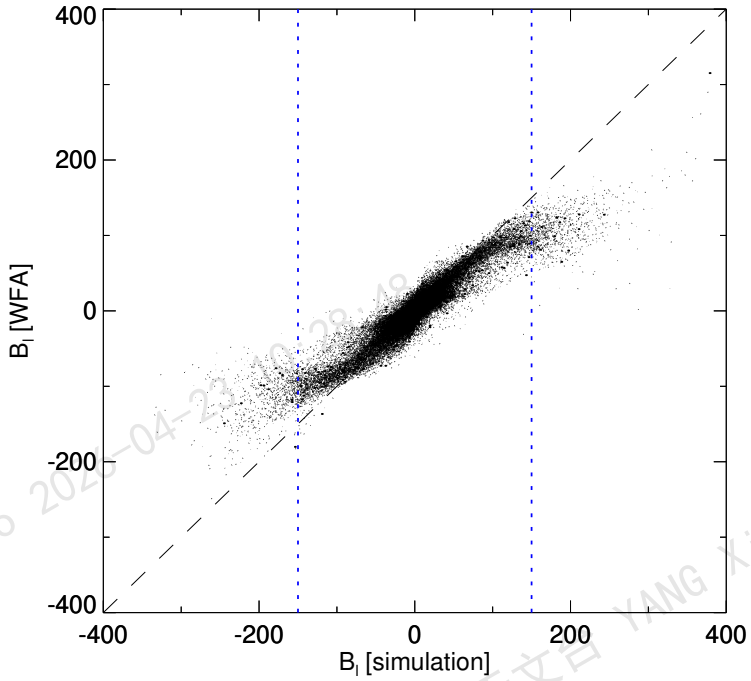

Figure 4-7 B_l as inferred from the WFA versus the actual values in the MHD simulation model. Vertical dotted blue lines demarcate the region of validity of the WFA.

In general, the approach of wavelength-integrated method and the WFA offers estimates for weak magnetic fields, assuming that these fields are completely resolved (i.e., with a filling factor $f = 1$). Consequently, the resultant values of magnetic field strength should be viewed as approximations. For precise measurements of field strengths, particularly in areas where the WFA is ineffective, it becomes imperative to employ Stokes inversion algorithms that consider line formation under conditions of non-local thermodynamic equilibrium, such as NICOLE (Socas-Navarro et al., 2015), STIC (de la Cruz Rodríguez

et al., 2019), and DeSIRe (Ruiz Cobo et al., 2022). This particular aspect of the research will be elaborated upon in chapter 5.

4.7 Effect of the spatial resolution

In observations, the size of a telescope's aperture is constrained. The primary solar telescope in China used for regular observations measures 1 m in aperture, while the largest solar telescope worldwide, the *Daniel K. Inouye* Solar Telescope (DKIST), boasts a 4 m aperture (Rimmele et al., 2020). Consequently, the spatial resolution of current solar telescopes is restricted. Given that the Mg I 12.32 μm wavelength falls within the mid-infrared spectrum, the diffraction limit resolution is notably lower compared to that for visible wavelengths. Within the simulation, each pixel corresponds to 48 km (equivalent to $0''.066$), thereby indicating a spatial resolution of $0''.13$.

The Rayleigh criterion, a fundamental concept in optics, is commonly employed in defining the Full Width at Half Maximum (FWHM) for telescopes. This criterion helps astronomers and optical engineers understand the resolving power of a telescope, which directly affects its ability to distinguish fine details and resolve closely spaced objects in the sky. Moreover, the FWHM of a telescope is determined by the angle subtended by the first minimum of the diffraction pattern produced by a point source of light. In simpler terms, it is the angular separation between two point sources at which the central peak of one diffraction pattern coincides with the first minimum of the other diffraction pattern. By utilizing the Rayleigh criterion to determine the FWHM of a telescope FWHM$= 1.22\lambda/D$, so we can expressed the diameter of telescope's aperture as:

$$D = 1.22\frac{\lambda}{(FWHM)} \times 206265 \tag{4-5}$$

where D is the aperture diameter expressed in meters, λ is the wavelength in meters, and the FWHM is in arcseconds.

To investigate the impact of spatial resolution, we convolved the synthetic Stokes profile maps with Gaussian functions of varying FWHM to replicate the Point Spread Function (PSF) of a telescope. The PSF was primarily guided by the apertures of three solar telescopes: the 1 m AIMS infrared system (Deng et al., 2016), the 4 m DKIST

(Rimmele et al., 2020), and the proposed 8 m Chinese Giant Solar Telescope (CGST; Liu et al., 2012). These telescopes possess spatial resolutions of $3''.1$, $0''.78$, and $0''.39$, respectively. Figure 4-8 show the MCPD and MLPD maps derived from the spatially degraded Stokes profiles, accounting for the distinct telescope diffraction limits. A

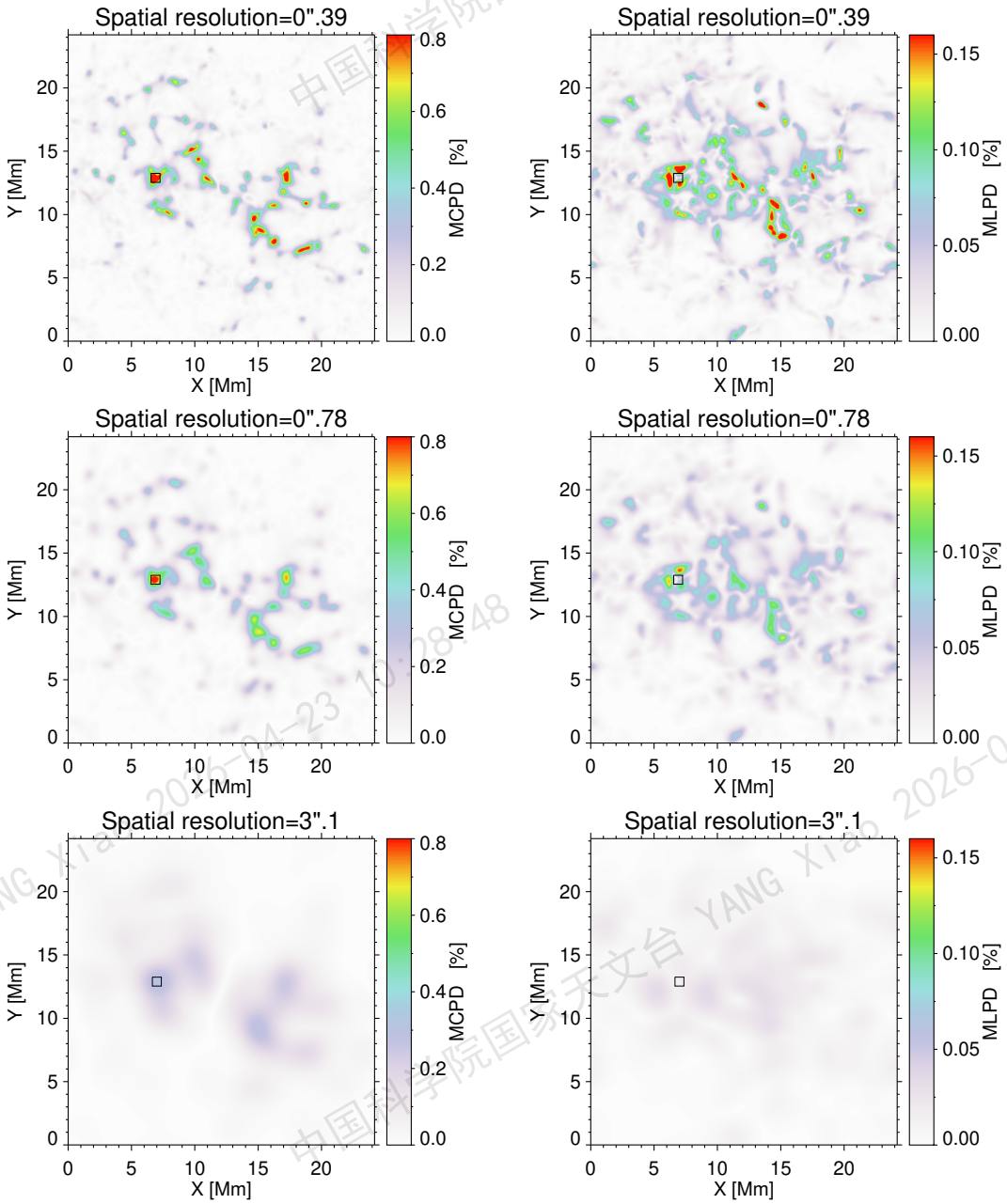

Figure 4-8 Maps of MCPD (first row) and MLPD (second row) for the degraded profiles of the Mg I 12.32 μm line at spatial resolutions of $0''.39$, $0''.78$, and $3''.1$, respectively, from top to bottom.

comparison between Figures 4-4 and 4-8 illustrates that as the resolution decreases, the magnitudes of the MCPD and MLPD decrease. At spatial resolutions of $0''.13$, $0''.39$, $0''.78$, and $3''.1$, the peak magnitudes of the MCPD (MLPD) are 4.6 (0.56), 1.2 (0.25),

0.9 (0.16), and 0.3 (0.03), respectively. Moreover, the maps exhibit increased blurring, with a growing number of fine atmospheric structures disappearing due to the reduced resolution associated with a broader Point Spread Function.

To understand how spatial resolution affects our ability to observe magnetic fields, we examined a pixel located at the center of a strong magnetic flux concentration. We analyzed the Stokes I and V profiles of this pixel at the original simulation resolution and three progressively coarser resolutions, as shown in Figure 4-9.

At the highest resolution $0''.13$, the Stokes I profile clearly reveals Zeeman splitting in the emission peak, characterized by wide absorption troughs and a large line width. This splitting arises from the interaction of polarized light with the magnetic field. The Stokes V profile, which measures the circular polarization of the light, exhibits a complex shape with four distinct lobes. As we degrade the spatial resolution, the Zeeman splitting in the Stokes I profile becomes less pronounced, with the two σ components (representing the splitting due to the magnetic field) moving closer together. Simultaneously, the amplitudes of the Stokes V lobes decrease, and the splitting between them becomes less distinct.

At a spatial resolution of $3''.1$, the Zeeman splitting in the Stokes I profile is no longer discernible, and the absorption trough feature disappears entirely. The Stokes V profile simplifies to a more typical shape with two lobes, accompanied by two broader features at the edges. These observations demonstrate that spatial resolution plays a critical role in resolving magnetic field signatures in spectral profiles. As resolution decreases, the ability to detect and quantify Zeeman splitting diminishes, leading to a loss of detail in the magnetic field structure. This highlights the importance of high-resolution observations for accurate magnetic field diagnostics.

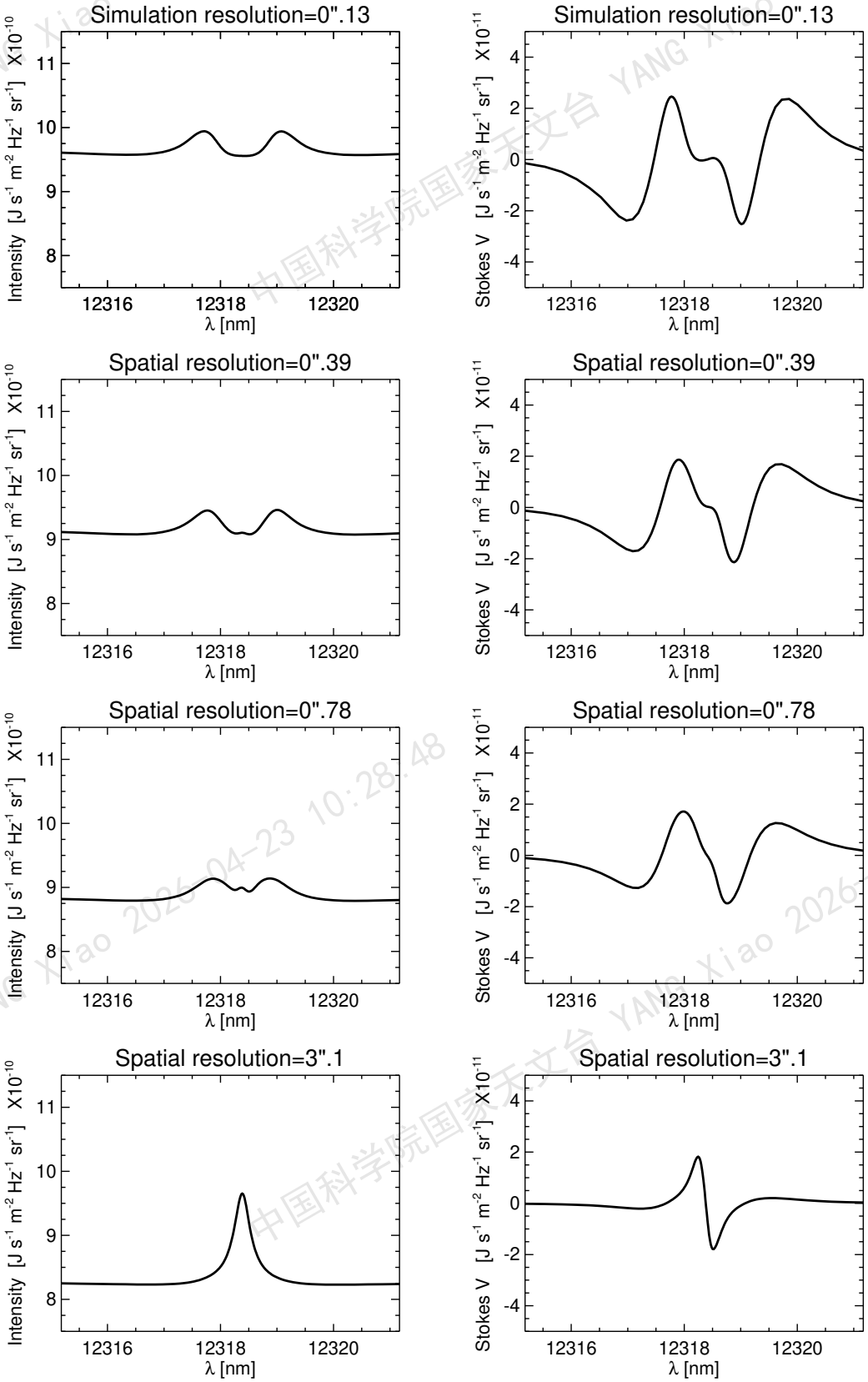

Figure 4-9 The synthetic Stokes I (left column) and Stokes V (right column) profiles, corresponding to a simulation resolution of $0''.13$**, and three different degraded resolutions (**$0''.38$**,** $0''.78$ **and** $3''.1$**), respectively, from top to bottom.**

To determine the necessary spatial resolution for observing Zeeman splitting in the Mg I 12.32 μm line, we analyzed a set of 504x504 synthetic Stokes I profiles generated from the Bifrost simulation. Our analysis revealed that a significant fraction (2.4%) of these synthetic Stokes I profiles (i.e., 6027 pixels) exhibited distinct Zeeman splitting, indicating the presence of strong magnetic fields in the corresponding regions of the solar atmosphere. Figure 4-10 illustrates the relationship between spatial resolution and the percentage of Stokes I profiles exhibiting detectable Zeeman splitting. As expected, the percentage of detectable splitting decreases as the spatial resolution of the telescope decreases. This is because lower resolution telescopes are less capable of resolving the fine details of the magnetic field structure.

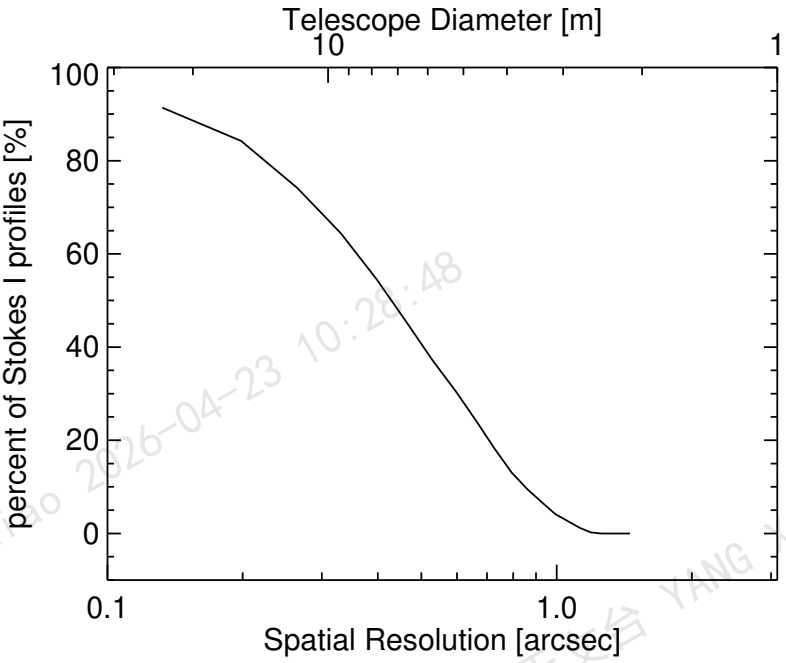

Figure 4-10 The percent of Stokes I profiles with clear Zeeman splitting as a function of the spatial resolution, and the telescope diameter that yields the spatial resolution as indicated in the second x-axis of the plot.

To further quantify the relationship between telescope size and spatial resolution, we used Equation 4-5 to calculate the telescope diameter required to achieve a given spatial resolution. Our results indicate that a telescope with a diameter of 7.2 meters and a spatial resolution of $0''.43$ is capable of detecting 50% of the simulated Stokes I splitting. This means that half of the magnetic field signatures in the simulation would be detectable with this telescope. Furthermore, we found that a telescope with a diameter of 3.2 meters and a spatial resolution of $0''.97$ can detect 5% of the simulated Stokes I

splitting. This resolution represents the minimum required for detecting Zeeman splitting in this particular dataset. These findings have significant implications for the design of future solar telescopes intended for observing the Mg I 12.32 μm line.

4.8 Conclusion

We utilized the RH code to synthesize the Mg I 12.32 μm line based on a 3D MHD simulation model produced from the Bifrost code, representing an enhanced network region. We performed column-by-column computations assuming a plane-parallel atmosphere and under the assumption of CRD. Focusing on a specific slice from the MHD simulation, featuring select magnetic flux concentrations, we determined the formation height of the Mg I 12.32 μm line's core at approximately 450 km above the solar surface, situated in the upper photosphere.

Our investigation extended to polarimetric profiles of the Mg I 12.32 μm line across various features. The Stokes I profiles stemming from both the magnetic flux concentrations and their peripheries revealed distinct Zeeman splitting and broad absorption troughs, with formation heights at 160 km and 340 km, respectively, lower than those of other features. In regions with weak magnetic fields, the Stokes I profiles demonstrated an emission peak, aligning with prior observations of quiet Sun. Additionally, the Stokes V profiles displayed two lobes with expanded features at the edges, while a complicated Stokes V profile with four lobes emerged at the core of strong magnetic flux concentration.

Analyzing the synthesized Stokes profiles, we computed the MCPD and MLPD, revealing strong correlations with B_l, and B_H at the specific height of 450 km in the simulation. These results concur with our analyses concerning the optical depth unity's height for the Mg I 12.32 μm line core. Furthermore, we delved deeper by exploring the practicality of the wavelength-integrated method and WFA as efficient tools for estimating the magnetic field's line-of-sight and perpendicular components via the Stokes profiles. Through the wavelength-integrated method, we observed a direct correlation between B_l and MCPD within the range of $B_l < 300$ G, and between B_H and MLPD across the entire B_H range in the simulation, indicating the method's saturation point. Additionally, our findings demonstrate the WFA's effectiveness in extracting the B_l component of magnetic field from synthetic profiles, particularly in cases of weak magnetic fields (i.e., B_l below 150 G).

We degraded the synthetic Stokes maps based on the apertures of AIMS, DKIST, and CGST to assess spatial resolution. At the resolutions of DKIST and CGST, certain Stokes I profiles still manifested Zeeman splitting, with the two σ components converging as resolution decreased. However,, at the AIMS resolution, no Zeeman splitting was discernible in the Stokes I profiles for the particular snapshot used. Our observations indicate that a resolution of $0''.97$, equivalent to a telescope with a 3.2-meter diameter, was essential for detecting Zeeman splitting within magnetic concentration regions or bright points in the quiet-Sun areas.

Chapter 5 Non-Local thermodynamic equilibrium inversions of the Mg I 12.32 μm line

5.1 Introduction

The mid-infrared Mg I 12.32 μm spectral line has a significant ratio of Zeeman splitting to Doppler broadening, which enables the observation of pronounced Zeeman splitting even in the presence of relatively weak magnetic fields. This characteristic is particularly advantageous for accurately assessing magnetic field strength, as it allows for precise measurements based on the separation of the Stokes I Zeeman components (Landi Degl'Innocenti et al., 2004).

In Chapter 4, we explored situations where the Zeeman components were not fully resolved. In such cases, both the weak field approximation (WFA) and wavelength-integrated methods can be effectively utilized to extract the magnetic field components, specifically the longitudinal component (B_L) and the horizontal component (B_H) (Lites et al., 2008; Martínez González et al., 2009). Our results indicate that the wavelength-integrated method reveals some limitations. Calibration curves derived from the Stokes profiles of the Mg I 12.32 μm line exhibit a nonlinear relationship for magnetic fields exceeding B_L >300 G and B_H >500 G (Li et al., 2021). Conversely, the WFA proves effective primarily for diagnosing magnetic fields within a narrower scope, specifically when B_L is below 150 G (Sedik et al., 2024). This discrepancy highlights a critical gap in the current diagnostic capabilities, underscoring the necessity for the development of additional tools and methodologies. Such advancements are essential for accurately measuring magnetic fields across a broader range of strengths, thereby enhancing our understanding of magnetic phenomena in various astrophysical contexts.

Non-local thermodynamic equilibrium (non-LTE) inversion codes are essential tools for interpreting spectropolarimetric observations and accurately measuring solar magnetic fields. These sophisticated codes excel in modeling the intricate radiative transfer processes occurring in the solar atmosphere, allowing for a more nuanced understanding of solar phenomena. Through the analysis of spectral lines, these codes can extract valuable information regarding various plasma parameters, including temperature, velocity fields, and magnetic field strengths.

The primary function of non-LTE inversion codes is to construct a best-fit atmospheric model that aligns closely with the observational data. This is achieved by solving the non-LTE radiative transfer equation using a nonlinear least-squares minimization approach, which optimizes the fit between the observed and predicted spectral profiles (Socas-Navarro et al., 1997, 2000). The precision with which these codes operate significantly enhances our ability to decode the complex interplay of physical conditions within the solar atmosphere. For a more comprehensive understanding of these advanced inversion techniques and their applications, interested readers are encouraged to consult the extensive reviews by del Toro Iniesta et al. (2016); de la Cruz Rodríguez et al. (2016). These reviews provide in-depth insights into the methodologies and advancements in the field, highlighting the importance of non-LTE inversion codes in contemporary solar physics research.

In this chapter, we employed the Stockholm Inversion Code (STiC; de la Cruz Rodríguez et al., 2016, 2019) to synthesize and invert the Stokes profiles of the Mg I 12.32 μm line, utilizing data derived from a three-dimensional magnetohydrodynamic (MHD) simulation. The STiC code integrates the capabilities of the RH code (Uitenbroek, 2001) to effectively address the non-LTE radiative transfer problem. Previous research has established that synthetic profiles generated from MHD simulations of various spectral lines can be instrumental in assessing the influence of noise and other instrumental variables on the precision of atmospheric parameters inferred from inversions (see, for instance, de la Cruz Rodríguez et al., 2012; da Silva Santos et al., 2018; Beck et al., 2019).

The primary objective of our investigation is to evaluate the effectiveness of retrieving accurate atmospheric parameters from the inversion of synthetic Stokes profiles corresponding to the Mg I 12.32 μm line. Furthermore, we explore how different levels of noise affect the accuracy of these retrieved parameters. This analysis is particularly significant for understanding the limitations imposed by noise when examining weak magnetic features, especially in the context of interpreting upcoming observations from the Accurate Infrared Magnetic Field Measurements of the Sun (AIMS; Deng et al., 2016). However, it is important to note that our study does not address the impact of restricted spatial and spectral resolution on the inversion results.

5.2 Model atmosphere

We employed a snapshot from a 3D MHD simulation of an enhanced network, specifically at a simulation time of $t = 3850$ seconds, as descried by Carlsson et al. (2016). For further information regarding the characteristics of this simulation, please refer to Section 4.2.

To facilitate our analysis, we transformed the original vertical geometrical grid of the simulation into a new grid that corresponds to the continuum optical depth at 500 nm (log τ_{500}). This transformation allows for a more accurate representation of the atmospheric conditions under investigation. In Figure 5-1, we present the maps illustrating the longitudinal magnetic field component (B_L) and the horizontal magnetic field component (B_H) at an optical depth of log $\tau_{500} = 0$.

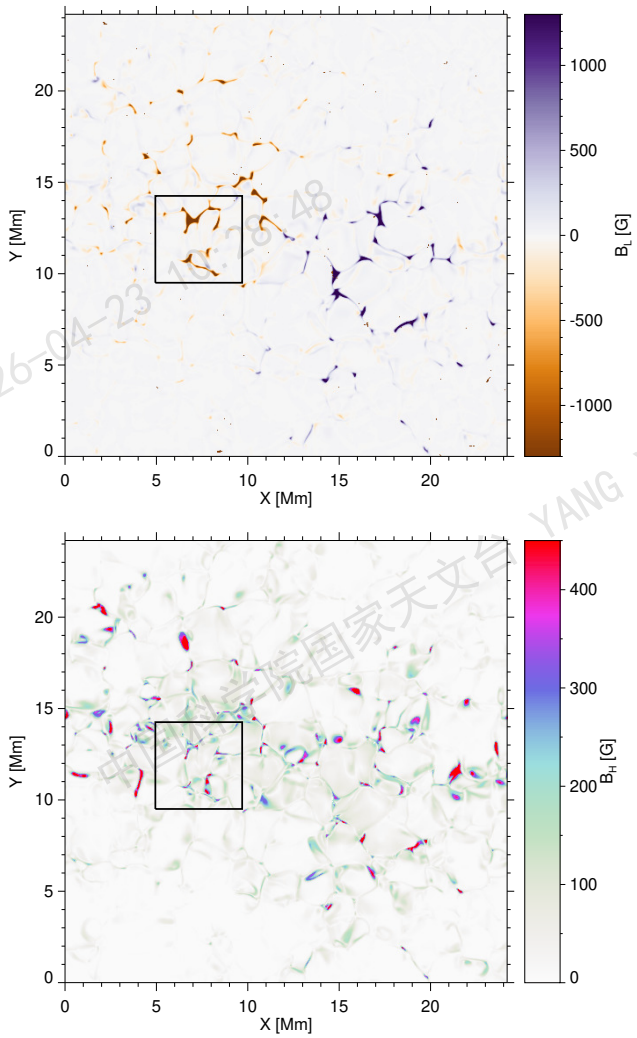

Figure 5-1 The horizontal distributions of the longitudinal (B_L; top panel) and horizontal (B_H; bottom panel) components of the magnetic field at optical depth of log $\tau_{500} = 0$. The black square remark the region which used in this study.

This figure clearly demonstrates that the magnetic field structure within the selected area is bipolar in nature, characterized by two opposing polarities that possess comparable magnetic field strengths. To enhance the efficiency of our computational analysis, we focused on a smaller region comprising 100×100 pixels, as delineated by the black square in Figure 5-1. This chosen area contains a blend of both strong and weak magnetic features, which provides an excellent opportunity to investigate the inversion of Stokes profiles across a wide range of magnetic field strengths.

By doing so, we can analyze a diverse range of spectropolarimetric signal amplitudes, which is crucial for understanding the varying impacts of magnetic fields on these signals. This approach not only facilitates a comprehensive analysis of the magnetic field characteristics but also allows us to explore the complexities associated with the inversion process, ultimately contributing to a deeper understanding of the magnetic dynamics present in the solar atmosphere.

5.3 Effect of photon noise on Stokes profiles

We utilized the STiC code to synthesize the Stokes spectra of the Mg I 12.32 μm line from our 3D MHD simulation. The spectral synthesis was conducted with a resolution of 0.05 nm over the wavelength range of 12315.16 nm to 12321.56 nm. This synthesis specifically focused on a designated region within the simulation, as highlighted by the black square in Figure 5-1.

The STiC code operates on the premise of a plane-parallel geometry, executing calculations on a column-by-column basis throughout the simulation model. This approach allows for detailed insights into the physical conditions present in each column of the solar atmosphere. Additionally, the synthesis was performed under complete frequency redistribution (CRD) conditions, which is pertinent for observations made at the solar disk center (i.e., when $\mu = 1$, where μ is defined as the cosine of the heliocentric angle θ).

The atomic parameters used in this synthesis are sourced from the modified model atom designated as MgI_66.atom, as elaborated by Sedik et al. (2024). This model atom incorporates critical atomic data necessary for accurately representing the interaction of light with the Mg I 12.32 μm line, thus enhancing the fidelity of our synthesized Stokes profiles. By employing these methodologies, we aim to achieve a precise characterization

of the magnetic field and plasma conditions in the solar atmosphere, contributing to a deeper understanding of solar magnetic phenomena.

In our investigation, we examined the influence of noise on the Stokes profiles of the Mg I 12.32 μm line by introducing random Gaussian noise at four different levels (σ), specifically 5×10^{-4}, 1×10^{-3}, 5×10^{-3} and 1×10^{-2} relative to the continuum intensity (I_c). To effectively illustrate the effects of this added noise, Figure 5-2 presents filtergrams of the Stokes parameters Q, U, and V at a wavelength offset of $\Delta\lambda = -0.2$ nm from the line center. These maps facilitate a direct comparison between the profiles devoid of noise and those affected by the various specified noise levels. Interestingly, we observed that a substantial portion of the polarization signals exhibited amplitudes exceeding 1×10^{-2} of I_c, as depicted in the first row of the figure 5-2. This observation underscores the potential significance of noise in the interpretation of spectropolarimetric data. It is important to note that we did not include any spectral degradation in our analysis; as a result, the synthetic Stokes profiles for the Mg I 12.32 μm line appear somewhat stronger than those typically observed in actual measurements.

In the left and middle columns of Figure 5-2, the linear polarization signals, Q and U, are predominantly observed at the borders of regions with strong magnetic field concentrations. This phenomenon can be attributed to the horizontal expansion of magnetic field lines with increasing height in the solar atmosphere. At the lower noise levels of $\sigma = 5 \times 10^{-4}$ and 1×10^{-3} of I_c, a clear delineation of both strong and weak magnetic features is evident, allowing for a comprehensive analysis of the underlying magnetic structures. However, as the noise levels increase, particularly at $\sigma = 1 \times 10^{-2}$ of I_c, many of the weaker polarization signals become increasingly obscured by the noise, especially in the spatial region defined by coordinates [3.5,3] Mm. Despite this degradation in signal clarity, several regions exhibiting strong polarization signals remain detectable, illustrating the resilience of robust magnetic features even in noisy conditions.

Conversely, the Stokes V signals maintain their prominence across all noise levels, serving as a reliable indicator of magnetic activity. The only exceptions to this trend occur in two specific areas with weaker signals located around [3.0,2.5] Mm and [4.5,2.7] Mm, as illustrated in the right column of Figure 5-2. The strong Stokes V signals are primarily concentrated at the centers of intense magnetic field concentrations, where the

magnetic field lines are oriented nearly vertically. This vertical alignment enhances the polarization signals, making them more discernible over varying levels of noise.

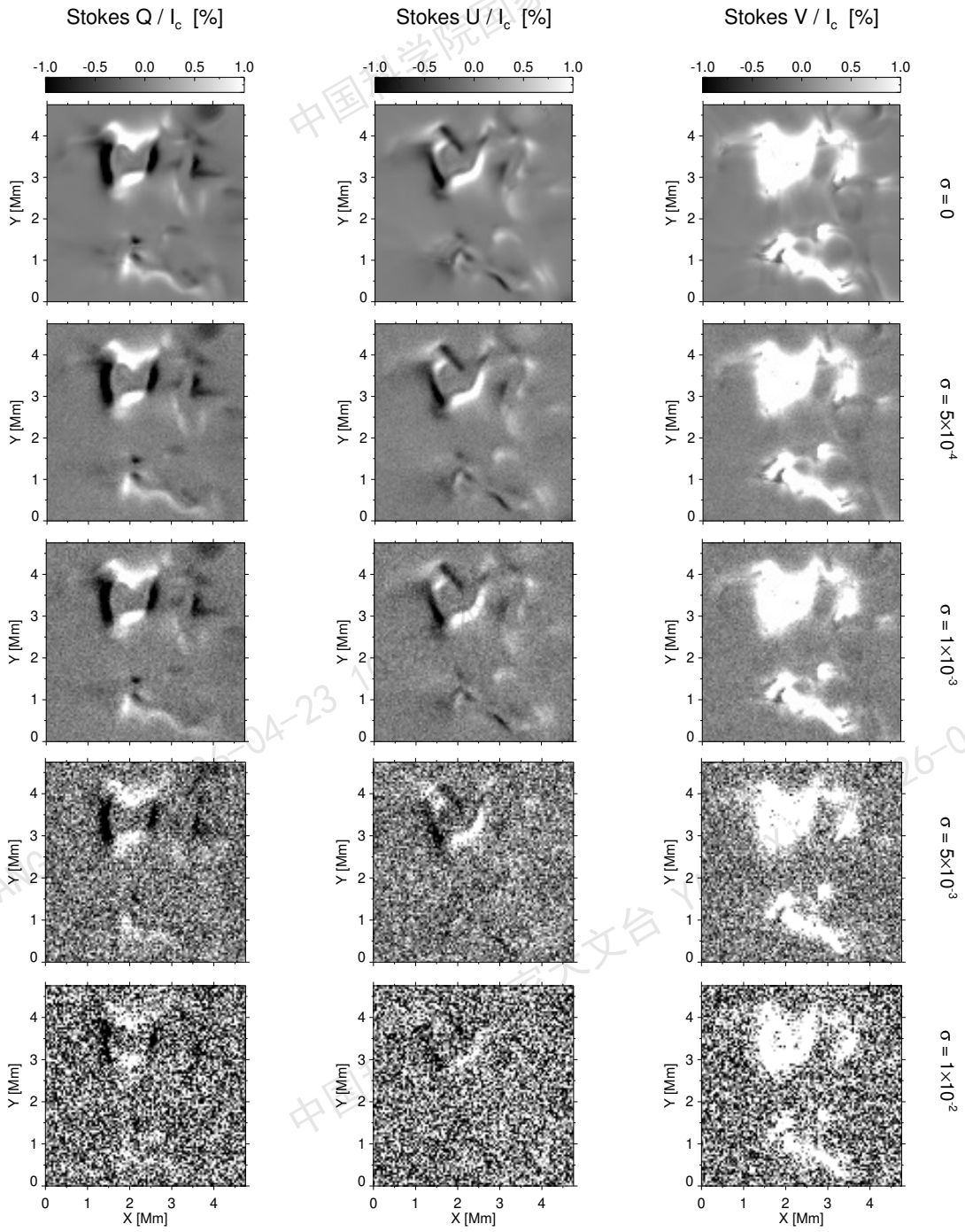

Figure 5-2 filtergrams of Stokes Q (left column), U (middle column) and V (right column) at a wavelength $\Delta\lambda = -0.2$ nm from the line center of the Mg I 12.32 μm line. From top to bottom: the stokes profiles with a random Gaussian noise of amplitudes 5×10^{-4}, 1×10^{-3}, 5×10^{-3} and 1×10^{-2} relative to the mean continuum intensity I_c, respectively.

5.4 Inversion of the Mg I 12.32 μm spectra

The inversions were carried out using the STiC code for the synthetic Stokes profiles derived from the specified region of the Bifrost simulation, as indicated by the black square in Figure 5-1. We performed inversions on both the original profiles and those subjected to four different levels of noise. The inversion configuration was designed with five nodes for temperature, four nodes for line-of-sight (LOS) velocity, and three nodes each for the longitudinal and horizontal components of the magnetic field, along with a single node representing the field azimuth. Notably, we did not incorporate a microturbulence velocity parameter in our inversions, as this aspect was not present in the Bifrost simulation.

To ensure optimal fitting of the Stokes profiles, the inversion processes require initialization with various guess model atmospheres, which assist the code in converging toward the global χ^2 minimum. For simplicity, we opted for single-cycle inversions initialized with a single guess atmosphere. This initial atmospheric model was adapted from the FALC model (Fontenla et al., 1993) and modified to include constant values for both longitudinal and horizontal magnetic field components, alongside constant LOS velocity and field azimuth. Moreover, we executed the inversions on a pixel-by-pixel basis, treating each spatial point independently to capture the local variations in the magnetic and thermal properties of the solar atmosphere.

5.4.1 Inversions of original spectra

We initially conducted an inversion analysis for the synthetic Stokes profiles without introducing any noise to assess the efficacy of the inversion process. To quantify the performance, we calculated the mean differences between the inferred atmospheric parameters and those of the original simulation atmosphere, as depicted in Figure 5-3. For temperature, the mean difference remains small across the hight range of $\log(\tau_{500}) = [-1.0, -3.0]$. In contrast, for other atmospherics parameters, the mean difference is observed within the range of $\log(\tau_{500}) = [-2.0, -4.0]$. Interestingly, we observed that the minimum differences among the atmospheric parameters occurred at an optical depth of $\log(\tau_{500}) = -2.7$. This particular optical depth corresponds to an average geometrical height of approximately 422 km within the Bifrost simulation, aligning well

with the sensitivity height of the Mg I 12.32 μm line, as reported by Li et al. (2021).

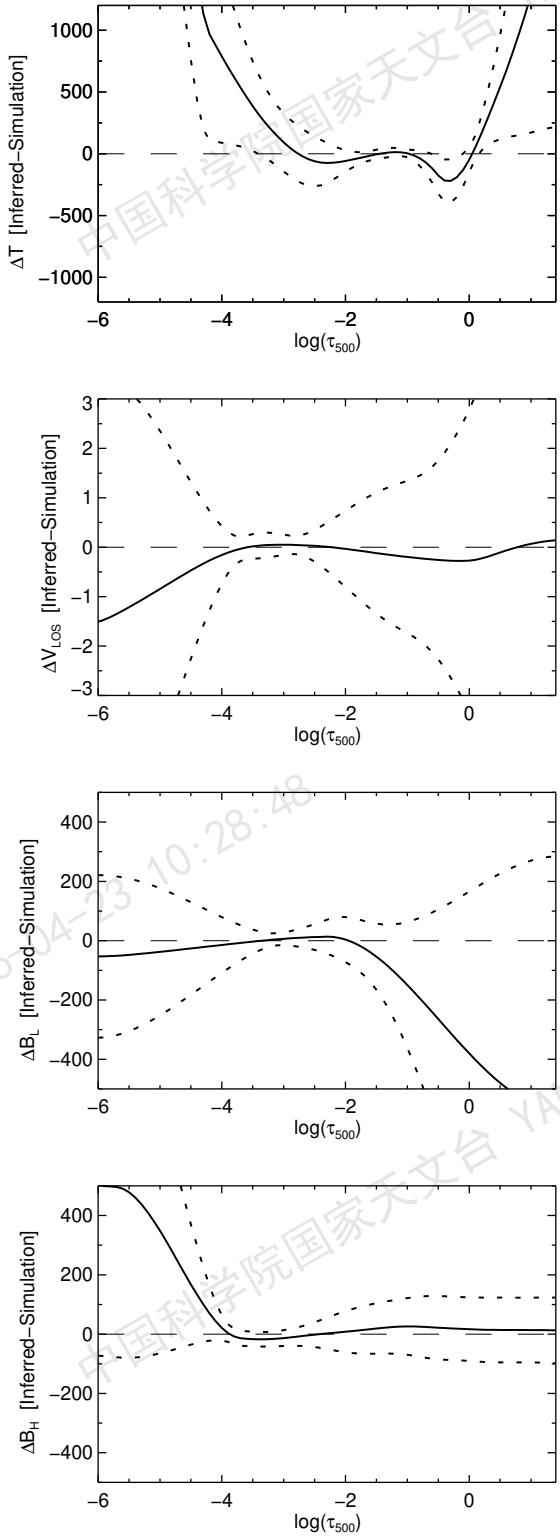

Figure 5-3 Mean differences between the inferred atmospheric parameters and those of the simulation as a function of the optical depth log (τ_{500}). From top to bottom: temperature, LOS velocity, longitudinal and horizontal components of magnetic field. Dotted line represents the standard deviation.

Figure 5-4 presents maps of the inferred atmospheric parameters obtained from the inversion analysis, compared with the original simulation atmosphere at an optical depth of $\log(\tau_{500}) = -2.7$. The first row of the figure showcases a comparison of temperature distributions, revealing a strong correlation between the inferred temperatures and the simulated values, reflected by a Pearson correlation coefficient of $r = 0.81$. This high degree of agreement indicates that the inversion process effectively captures the thermal structure of the atmosphere.

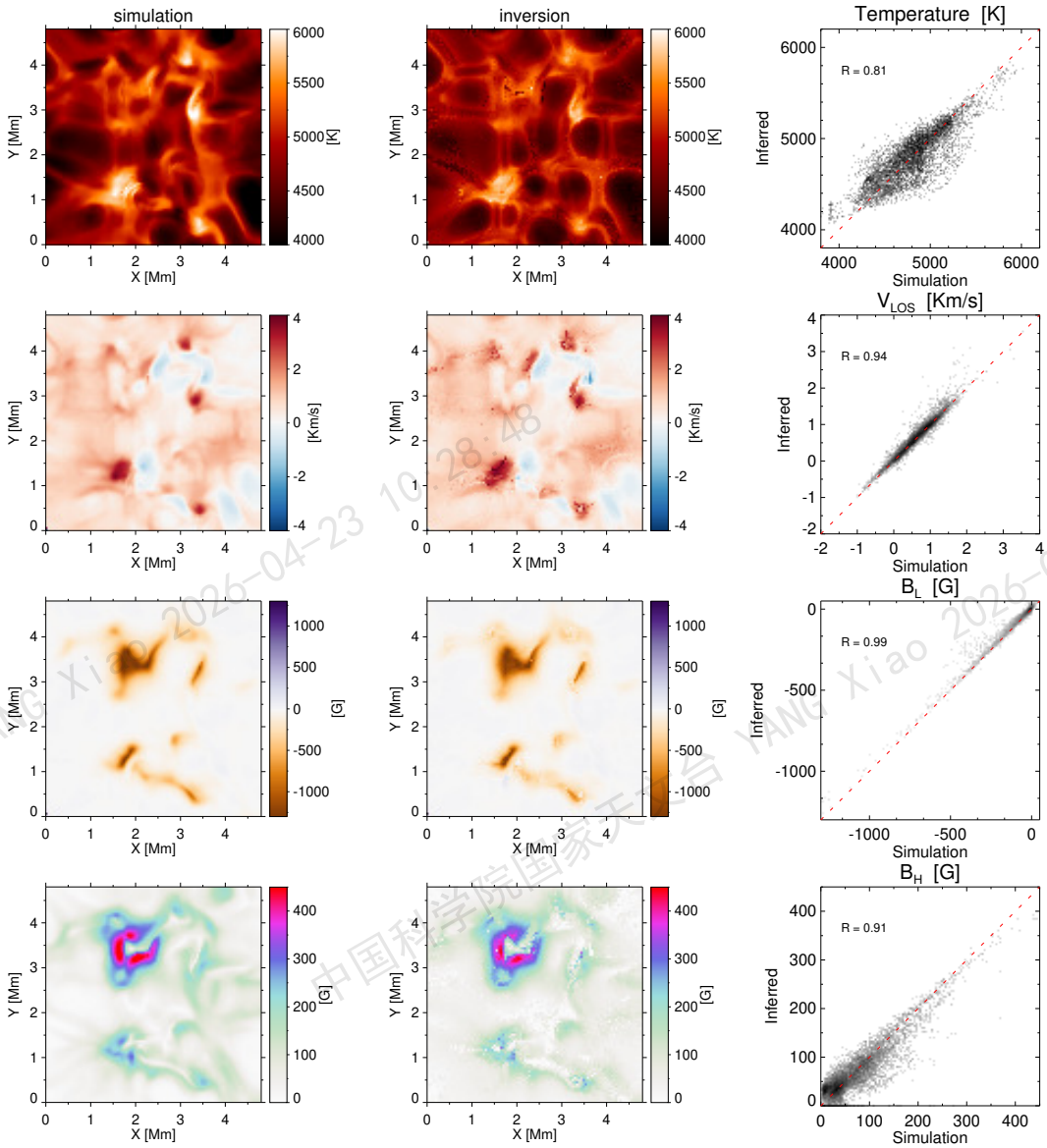

Figure 5-4 The horizontal distributions of, from top to bottom, temperature, LOS velocity, longitudinal and horizontal magnetic field from the simulation (left column) and inversion (middle column) at optical depth of $\log(\tau_{500}) = -2.7$. The scatter plots of each physical quantity are presented in the right column, with the Pearson correlation coefficient (r) at the top left and the red dashed lines represent one-to-one correspondences.

In the second row, we examine the LOS velocity comparison, where the inversion results align remarkably well with the simulation data, achieving an impre- ssive Pearson correlation coefficient of $r = 0.94$. This close alignment underscores the inversion's ability to accurately retrieve kinematic information within the atmospheric model.

The third row of Figure 5-4 displays the inversion results for the longitudinal magnetic field component, which also demonstrate a high degree of concordance with the original atmosphere, indicated by a Pearson correlation coefficient of $r = 0.99$. In the bottom row, the inferred values for the horizontal magnetic field component are generally consistent with the original atmospheric values, yielding a correlation coefficient of $r = 0.91$. However, it is important to note that there are noticeable discrepancies in some areas. The inversion process struggled to accurately reproduce certain weak magnetic features, a limitation attributed to the inherent complexity of the original atmosphere, where rapid changes in field inclination are manifested in a canopy-like structure.

5.4.2 Inversions of noisy spectra

We analyzed photon noise impacts on atmospheric parameter retrieval through the inversions of synthetic Stokes profiles contaminated with four distinct noise amplitudes: 5×10^{-4}, 1×10^{-3}, 5×10^{-3} and 1×10^{-2} relative to I_c. As shown in Figure 5-5, temperature reconstructions (left panels) demonstrate exceptional fidelity compared to the original MHD simulation atmosphere, maintaining diagnostic capability even under extreme noise conditions (1×10^{-2} of I_c).

The second and third columns of Figure 5-5 illustrate the inferred LOS velocity and the longitudinal component of the magnetic field, respectively. Both of these atmospheric parameters demonstrate a robust correlation with the corresponding values from the simulation data, indicating a high level of accuracy in the inversion process. Notably, while the inferred values for these parameters exhibit only minor fluctuations at noise levels exceeding 1×10^{-3} of I_c, the strong features associated with the longitudinal magnetic field remain reliably reconstructed even at a noise level of 1×10^{-2} of I_c. This resilience in recovering significant longitudinal field characteristics under higher noise conditions highlights the effectiveness of the inversion methodology in discerning vital magnetic information, even in the presence of increased observational uncertainty.

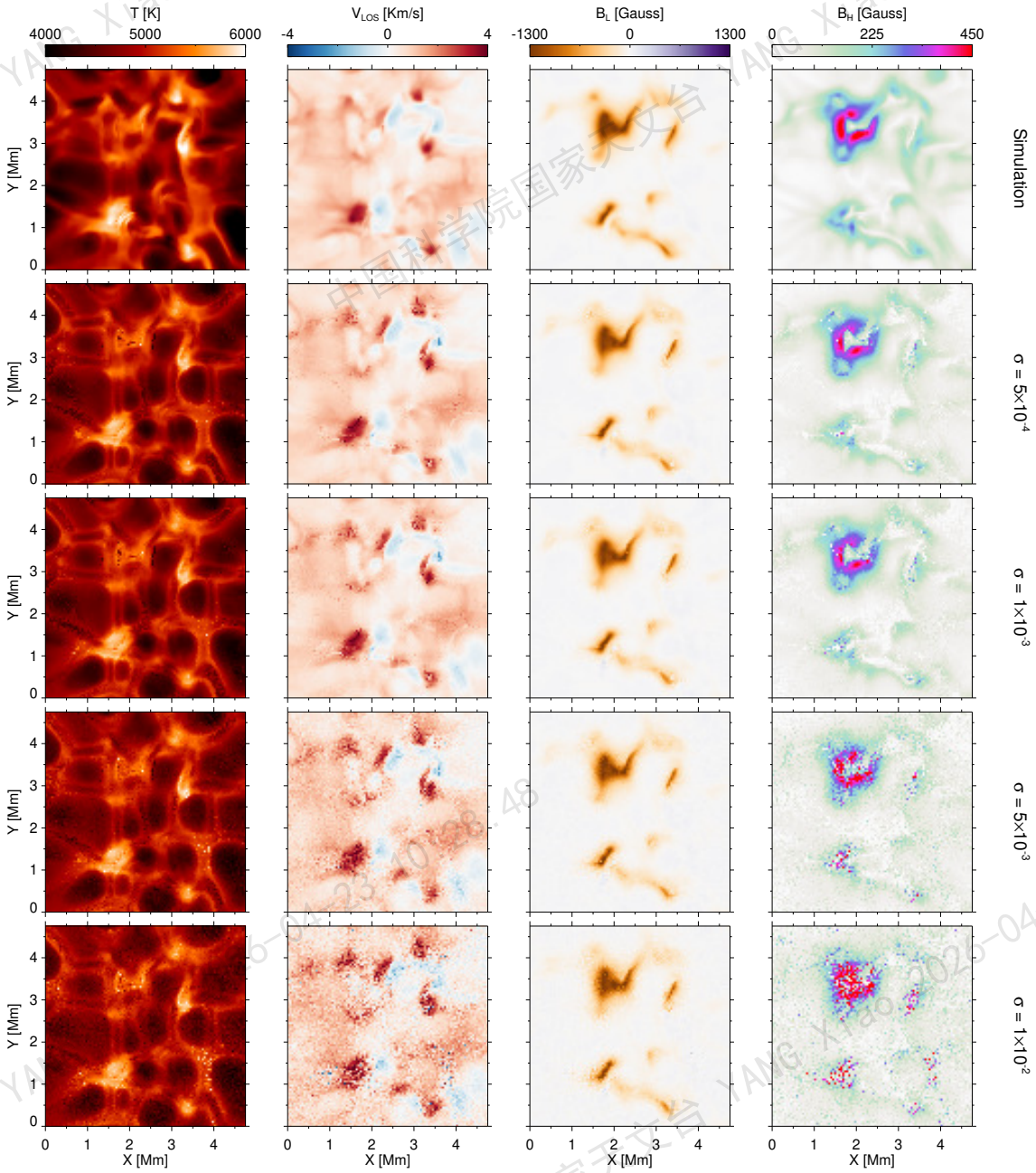

Figure 5-5 Maps of the inferred atmospheric parameters from the inversions of Stokes profiles with four different noise levels. from top to bottom: the original atmosphere, inversions results for noise levels of 5×10^{-4}, 1×10^{-3}, 5×10^{-3} and 1×10^{-2} of I_c. Columns display, from left to right, temperature, LOS velocity, longitudinal and horizontal components of the magnetic field.

In the analysis of the horizontal component of the magnetic field, presented in the right column of Figure 5-5, the inferred values closely align with the original simulation data at noise levels up to 1×10^{-3} of I_c. This strong correspondence illustrates the efficacy of the inversion process in accurately retrieving horizontal magnetic field characteristics under relatively low noise conditions. However, as the noise levels increase

beyond this threshold, the discrepancies between the inferred values and the original data become significantly pronounced. At noise levels reaching 5×10^{-3} of I_c, the inversion method is primarily able to identify regions exhibiting strong horizontal magnetic fields, where the differences between the inferred and original values remain minimal. This suggests that while the inversion is capable of preserving the integrity of strong magnetic features, its ability to accurately reconstruct weaker horizontal field components diminishes with increasing noise. Such findings highlight the challenges posed by observational noise in the study of solar magnetic fields, emphasizing the need for careful consideration of noise levels when interpreting inversion results.

For comprehensive analysis, we present histograms comparing the differences between the inferred atmospheric parameters and those obtained from the simulation, as shown in Figure 5-6. The distribution of temperature differences reveals a pronounced peak at zero for inversion results derived from the original spectra, which were analyzed without any added noise ($\sigma = 0$). As noise levels increase, the distributions retain a consistent shape and width; however, the peaks slightly decrease at noise levels of 5×10^{-3} and 1×10^{-2} of I_c.

In contrast, the histograms for other atmospheric parameters, including V_{LOS}, B_L and B_H, exhibit narrow distributions with peaks centered at zero for the inversion results based on the original spectra. Interestingly, some pixels reflect inferred magnetic field components that are weaker than those present in the original atmospheric model, leading to broader tails on the right side of the ΔB_L distribution and the left side of the ΔB_H distribution.

For noise levels up to 1×10^{-3} of I_c, the difference distributions remain largely consistent. However, as noise levels increase, the discrepancies become increasingly pronounced. The peaks of these distributions decline rapidly and broaden, indicating a significant deterioration in the accuracy of the inferred atmospheric parameters under elevated noise conditions.

Overall, this analysis underscores the capability of inferring atmospheric parameters from the inversion of Stokes profiles of the Mg I 12.32 μm line. Based on the Bifrost simulation, we conclude that the inversion method can accurately retrieve the atmospheric parameters for observations with noise levels up to 1×10^{-3} of I_c.

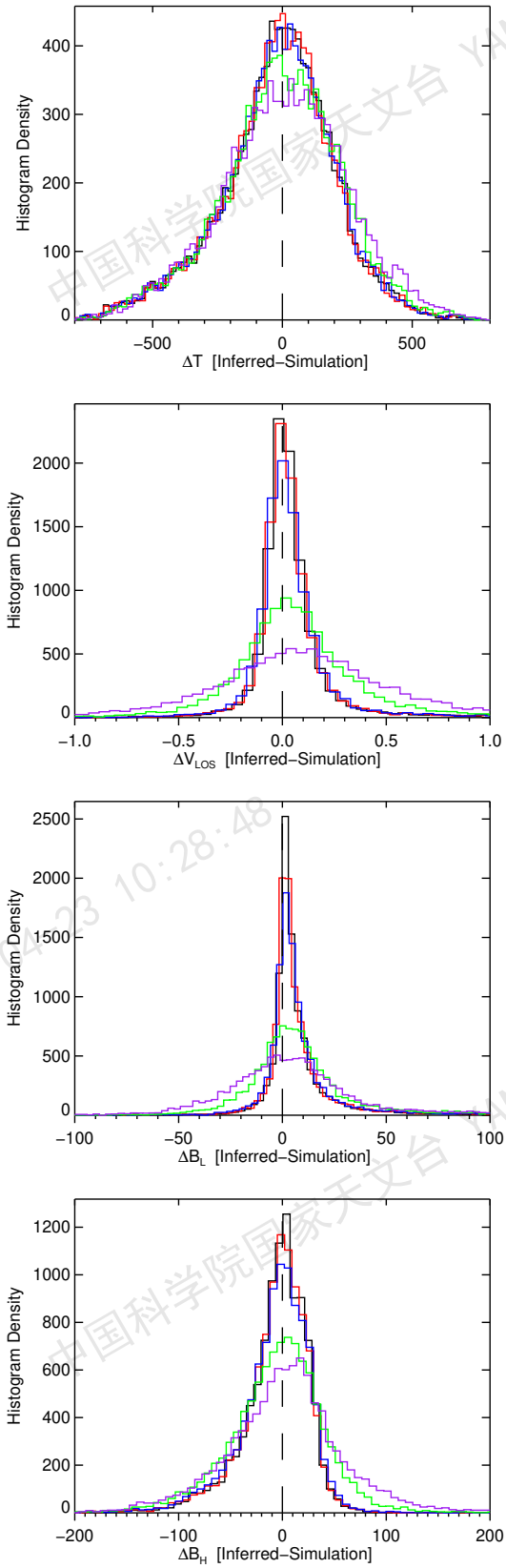

Figure 5-6 Histograms of the differences between the inferred atmospheric parameters from the inversions and those of the Bifrost simulation. The line colors of black, red, blue, green and purple are corresponding to the inversion results of Stoke profiles without any noise and those with noise levels of 5×10^{-4}, 1×10^{-3}, 5×10^{-3} and 1×10^{-2} of I_c, respectively.

5.5 Conclusion

In this chapter, we explored the non-local thermodynamic equilibrium inversions of the Mg I 12.32 μm line, focusing on the retrieval of atmospheric parameters from synthetic Stokes profiles generated by a 3D magnetohydrodynamic simulation. The effectiveness of the STiC inversion code was evaluated, particularly in the context of varying noise levels and their impact on the accuracy of inferred parameters.

Our findings demonstrate that the inversion process can accurately retrieve the atmospheric parameters, such as temperature, line-of-sight velocity, and magnetic field components, even under conditions of significant photon noise. Notably, the inversion yielded a strong correlation between the inferred values and the original simulation data, with Pearson correlation coefficients exceeding 0.9 for most parameters at low noise levels.

The analysis revealed that temperature differences remained small across a wide range of optical depths, while the inversion's ability to recover magnetic field components was subject to limitations, particularly in the presence of noise. As noise levels increased beyond 1×10^{-3} of the continuum intensity, the accuracy of the inferred parameters began to decline, highlighting the challenges posed by observational noise in the study of solar magnetic fields for quiet Sun regions.

Furthermore, the histograms of the differences between inferred and simulated parameters illustrated that while the inversion method retains robustness against low noise levels, the degradation in accuracy becomes pronounced as noise increases. This underscores the necessity for careful consideration of noise factors when interpreting spectro-polarimetric data.

Finally, our analysis emphasizes the potential of non-LTE inversion techniques, particularly with the Mg I 12.32 μm line, to enhance our understanding of solar magnetic phenomena. Future research should focus on investigations into the impacts of spatial and spectral resolution on inversion results will be crucial for advancing our capabilities in solar observational studies.

Chapter 6 Summary and Prospective studies

The thesis presents a detailed investigation into the magnetic fields of the quiet Sun using high-resolution spectropolarimetric data from Hinode SOT/SP and synthetic observations derived from 3D MHD simulations. In Chapter 3, the analysis of Hinode data revealed significant linear polarization signals in 27% and 56% of pixels for 1.1-minute and 6.1-minute integrated datasets, respectively. The SIR inversion technique successfully reproduced asymmetries in Stokes V profiles, providing insights into the stratification of atmospheric parameters. The magnetic field distributions showed a peak in the hecto-Gauss range, with quasi-isotropic inclinations at the solar surface and predominantly horizontal fields in the upper layers. Longitudinal and transverse flux densities were consistent with previous studies, supporting the presence of substantial magnetic fields in the upper photosphere.

Chapter 4 focused on synthesizing the Mg I 12.32 μm line using the RH code, revealing its formation height at approximately 450 km in the upper photosphere. Distinct polarimetric profiles were observed in magnetic flux concentrations, with Zeeman splitting detectable at resolutions achievable by telescopes like AIMS, DKIST, and CGST. The wavelength-integrated method and Weak Field Approximation (WFA) proved effective for estimating magnetic field components, though with limitations at higher field strengths. The study emphasized the need for high-resolution observations to resolve fine magnetic structures in the quiet Sun.

In Chapter 5, non-LTE inversions using the STiC code demonstrated high accuracy in retrieving atmospheric parameters such as temperature, velocity, and magnetic field components from synthetic profiles, particularly at low noise levels. However, noise levels above 1×10^{-3} significantly degraded the inversion accuracy, underscoring the importance of high signal-to-noise data for reliable results. The study highlighted the potential of the Mg I 12.32 μm line for probing solar magnetic phenomena and the robustness of non-LTE inversion techniques under optimal conditions.

Future research should leverage next-generation telescopes like CGST, DKIST and EST to achieve higher spatial resolution and lower noise levels, improving magnetic

field measurements in quiet Sun internetwork and network regions through using SIR inversion code. Additionally, Combining Hinode observations with these data could provide deeper insights into magnetic field evolution and its relationship with solar dynamics.

We suggest in future work to expanding the analysis of the Mg I 12.32 μm line to other solar features, such as sunspots and plages, using 3D MHD simulations could further validate its diagnostic capabilities. Furthermore, investigating non-LTE inversion robustness under varying spatial and spectral resolutions.

References

Abdelkawy A G A, Shaltout A M K. Analysis of photospheric magnetic fields in AR 12546: a case study [J/OL]. Ap&SS, 2023, 368(8): 65. DOI: 10.1007/s10509-023-04220-3.

Asensio Ramos A. Evidence for Quasi-Isotropic Magnetic Fields from Hinode Quiet-Sun Observations [J/OL]. ApJ, 2009, 701(2): 1032-1043. DOI: 10.1088/0004-637X/701/2/1032.

Asensio Ramos A, Martínez González M J. Hierarchical analysis of the quiet-Sun magnetism [J/OL]. A&A, 2014, 572: A98. DOI: 10.1051/0004-6361/201423860.

Asplund M, Grevesse N, Sauval A J, et al. The Chemical Composition of the Sun [J/OL]. Ann. Rev. Astron. Astrophys., 2009, 47(1): 481-522. DOI: 10.1146/annurev.astro.46.060407.145222.

Auer L H, Heasley J N, House L L. The determination of vector magnetic fields from Stokes profiles. [J/OL]. Sol. Phys., 1977, 55(1): 47-61. DOI: 10.1007/BF00150873.

Beck C, Rezaei R. The magnetic flux of the quiet Sun internetwork as observed with the Tenerife infrared polarimeter [J/OL]. A&A, 2009, 502(3): 969-979. DOI: 10.1051/0004-6361/200911727.

Beck C, Gosain S, Kiessner C. Fast Inversion of Solar Ca II Spectra in Non-local Thermodynamic Equilibrium [J/OL]. ApJ, 2019, 878(1): 60. DOI: 10.3847/1538-4357/ab1d4c.

Bellot Rubio L R, Orozco Suárez D. Pervasive Linear Polarization Signals in the Quiet Sun [J/OL]. ApJ, 2012, 757(1): 19. DOI: 10.1088/0004-637X/757/1/19.

Bianda M, Stenflo J O, Solanki S K. Hanle effect observations with the CA BT I 4227 Å line [J]. A&A, 1999, 350: 1060-1070.

Borrero J M, Kobel P. Inferring the magnetic field vector in the quiet Sun. I. Photon noise and selection criteria [J/OL]. A&A, 2011b, 527: A29. DOI: 10.1051/0004-6361/201015634.

Borrero J M, Solanki S K, Bellot Rubio L R, et al. On the fine structure of sunspot penumbrae. I. A quantitative comparison of two semiempirical models with implications for the Evershed effect [J/OL]. A&A, 2004, 422: 1093-1104. DOI: 10.1051/0004-6361:20041001.

Borrero J M, Tomczyk S, Kubo M, et al. VFISV: Very Fast Inversion of the Stokes Vector for the Helioseismic and Magnetic Imager [J/OL]. Sol. Phy., 2011a, 273(1): 267-293. DOI: 10.1007/s11207-010-9515-6.

Brault J, Noyes R. Solar emission lines near 12 microns [J/OL]. ApJL, 1983, 269: L61-L66. DOI: 10.1086/184056.

Bruls J H M J, Solanki S K, Rutten R J, et al. Infrared lines as probes of solar magnetic features. VIII. MgI 12μm diagnostics of sunspots. [J]. A&A, 1995, 293: 225-239.

Cao W, Gorceix N, Coulter R, et al. Scientific instrumentation for the 1.6 m New Solar Telescope in Big Bear [J/OL]. Astron. Nachr., 2010, 331(6): 636. DOI: 10.1002/asna.201011390.

Carlsson M, Rutten R J. Solar hydrogen lines in the infrared [J]. A&A, 1992, 259(2): L53-L56.

Carlsson M, Hansteen V H, Gudiksen B V, et al. A publicly available simulation of an enhanced network region of the Sun [J/OL]. A&A, 2016, 585: A4. DOI: 10.1051/0004-6361/201527226.

Cattaneo F. On the origin of magnetic fields in the quiet photosphere [J/OL]. ApJ, 1999, 515(1): L39. https://dx.doi.org/10.1086/311962.

Centeno R, Socas-Navarro H, Lites B, et al. Emergence of Small-Scale Magnetic Loops in the Quiet-Sun Internetwork [J/OL]. ApJL, 2007, 666(2): L137-L140. DOI: 10.1086/521726.

Chang E S, Noyes R W. Identification of the solar emission lines near 12 microns [J/OL]. ApJ, 1983, 275: L11-L13. DOI: 10.1086/184161.

Chang E S. Solar emission lines revisited: extended study of magnesium. [J/OL]. Phys. Scr., 1987, 35(6): 792-797. DOI: 10.1088/0031-8949/35/6/006.

Cheung M C M, Schüssler M, Moreno-Insertis F. Magnetic flux emergence in granular convection: radiative MHD simulations and observational signatures [J/OL]. A&A, 2007, 467(2): 703-719. DOI: 10.1051/0004-6361:20077048.

da Silva Santos J M, de la Cruz Rodríguez J, Leenaarts J. Temperature constraints from inversions of synthetic solar optical, UV, and radio spectra [J/OL]. A&A, 2018, 620: A124. DOI: 10.1051/0004-6361/201833664.

Danilovic S, Beeck B, Pietarila A, et al. Transverse Component of the Magnetic Field in the Solar Photosphere Observed by SUNRISE [J/OL]. ApJL, 2010, 723(2): L149-L153. DOI: 10.1088/2041-8205/723/2/L149.

Danilovic S, van Noort M, Rempel M. Internetwork magnetic field as revealed by two-dimensional inversions [J/OL]. A&A, 2016, 593: A93. DOI: 10.1051/0004-6361/201527842.

de la Cruz Rodríguez J, Socas-Navarro H, Carlsson M, et al. Non-local thermodynamic equilibrium inversions from a 3D magnetohydrodynamic chromospheric model [J/OL]. A&A, 2012, 543: A34. DOI: 10.1051/0004-6361/201218825.

de la Cruz Rodríguez J, Leenaarts J, Danilovic S, et al. STiC: A multiatom non-LTE PRD inversion code for full-Stokes solar observations [J/OL]. A&A, 2019, 623: A74. DOI: 10.1051/0004-6361/201834464.

de la Cruz Rodríguez J, Leenaarts J, Asensio Ramos A. Non-LTE Inversions of the Mg II h & k and UV Triplet Lines [J/OL]. ApJL, 2016, 830(2): L30. DOI: 10.3847/2041-8205/830/2/L30.

De Pontieu B. High-Resolution Observations of Small-Scale Emerging Flux in the Photosphere [J/OL]. ApJ, 2002, 569(1): 474-486. DOI: 10.1086/339231.

del Pino Alemán T, Trujillo Bueno J, Štěpán J, et al. A Novel Investigation of the Small-scale Magnetic Activity of the Quiet Sun via the Hanle Effect in the Sr I 4607 Å Line [J/OL]. ApJ, 2018, 863(2): 164. DOI: 10.3847/1538-4357/aaceab.

Del Toro Iniesta J C, Ruiz Cobo B. Stokes Profiles Inversion Techniques [J/OL]. Sol. Phys., 1996, 164(1-2): 169-182. DOI: 10.1007/BF00146631.

del Toro Iniesta J C. Introduction to spectropolarimetry [M/OL]. Cambridge University Press, 2003. DOI: 10.1017/CBO9780511536250.

del Toro Iniesta J C, Ruiz Cobo B. Inversion of the radiative transfer equation for polarized light [J/OL]. Living Reviews in Solar Physics, 2016, 13(1): 4. DOI: 10.1007/s41116-016-0005-2.

Deng Y, Liu Z, Qu Z, et al. The Chinese Giant Solar Telescope [C]//Dorotovic I, Fischer C E, Temmer M. Astronomical Society of the Pacific Conference Series: volume 504 Coimbra Solar Physics Meeting: Ground-based Solar Observations in the Space Instrumentation Era. 2016: 293.

Fontenla J M, Avrett E H, Loeser R. Energy Balance in the Solar Transition Region. III. Helium Emission in Hydrostatic, Constant-Abundance Models with Diffusion [J/OL]. ApJ, 1993, 406: 319. DOI: 10.1086/172443.

Gingerich O, Noyes R W, Kalkofen W, et al. The Harvard-Smithsonian reference atmosphere [J/OL]. Sol. Phys., 1971, 18(3): 347-365. DOI: 10.1007/BF00149057.

Gömöry P, Beck C, Balthasar H, et al. Magnetic loop emergence within a granule [J/OL]. A&A, 2010, 511: A14. DOI: 10.1051/0004-6361/200912807.

Gošić M, Bellot Rubio L R, Orozco Suárez D, et al. The Solar Internetwork. I. Contribution to the Network Magnetic Flux [J/OL]. ApJ, 2014, 797(1): 49. DOI: 10.1088/0004-637X/797/1/49.

Gudiksen B V, Carlsson M, Hansteen V H, et al. The stellar atmosphere simulation code Bifrost. Code description and validation [J/OL]. A&A, 2011, 531: A154. DOI: 10.1051/0004-6361/201116520.

Hansen P C, O' Leary D P. The use of the l-curve in the regularization of discrete ill-posed problems [J]. SIAM J. Sci. Comput., 1993, 14(6): 1487-1503.

Harvey J W, Branston D, Henney C J, et al. Seething Horizontal Magnetic Fields in the Quiet Solar Photosphere [J/OL]. ApJL, 2007, 659(2): L177-L180. DOI: 10.1086/518036.

Hasegawa T, Noda C Q, Shimizu T, et al. On the Formation of Lyman β and the O I 1027 and 1028 Å Spectral Lines [J/OL]. ApJ, 2020, 900(1): 34. DOI: 10.3847/1538-4357/aba95c.

Hayek W, Asplund M, Carlsson M, et al. Radiative transfer with scattering for domain-decomposed 3D MHD simulations of cool stellar atmospheres. Numerical methods and application to the quiet, non-magnetic, surface of a solar-type star [J/OL]. A&A, 2010, 517: A49. DOI: 10.1051/0004-6361/201014210.

Hecht E. Optics [M]. 4th ed. Addison-Wesley, 1998.

Hewagama T, Deming D, Jennings D E, et al. Solar Magnetic Field Studies Using the 12 Micron Emission Lines. II. Stokes Profiles and Vector Field Samples in Sunspots [J/OL]. ApJS, 1993, 86: 313. DOI: 10.1086/191781.

Hong J, Bai X, Li Y, et al. Non-LTE Calculations of the Mg I 12.32 μm Line in a Flaring Atmosphere [J/OL]. ApJ, 2020, 898(2): 134. DOI: 10.3847/1538-4357/ab9c21.

Ichimoto K, Lites B, Elmore D, et al. Polarization Calibration of the Solar Optical Telescope onboard Hinode [J/OL]. Sol. Phys., 2008, 249(2): 233-261. DOI: 10.1007/s11207-008-9169-9.

Ishikawa R, Tsuneta S. Comparison of transient horizontal magnetic fields in a plage region and in the quiet Sun [J/OL]. A&A, 2009, 495(2): 607-612. DOI: 10.1051/0004-6361:200810636.

Ishikawa R, Tsuneta S. The Relationship between Vertical and Horizontal Magnetic Fields in the Quiet Sun [J/OL]. ApJ, 2011, 735(2): 74. DOI: 10.1088/0004-637X/735/2/74.

Ishikawa R, Tsuneta S, Jurčák J. Three-Dimensional View of Transient Horizontal Magnetic Fields in the Photosphere [J/OL]. ApJ, 2010, 713(2): 1310-1321. DOI: 10.1088/0004-637X/713/2/1310.

Jefferies J, Lites B W, Skumanich A. Transfer of Line Radiation in a Magnetic Field [J/OL]. ApJ, 1989, 343: 920. DOI: 10.1086/167762.

Jennings D E, Deming D, McCabe G, et al. Solar Magnetic Field Studies Using the 12 Micron Emission Lines. IV. Observations of a Delta Region Solar Flare [J/OL]. ApJ, 2002, 568(2): 1043-1048. DOI: 10.1086/339159.

Jin C, Wang J, Zhao M. Vector Magnetic Fields of Solar Granulation [J/OL]. ApJ, 2009, 690(1): 279-287. DOI: 10.1088/0004-637X/690/1/279.

Kaufman V, Martin W C. Wavelengths and Energy Level Classifications of Magnesium Spectra for All Stages of Ionization (Mg I through Mg XII) [J/OL]. Journal of Physical and Chemical Reference Data, 1991, 20(1): 83-152. DOI: 10.1063/1.555879.

Keller C U, Deubner F L, Egger U, et al. On the strength of solar intra-network fields. [J]. A&A, 1994, 286: 626-634.

Khomenko E V, Collados M, Solanki S K, et al. Quiet-Sun inter-network magnetic fields observed in the infrared [J/OL]. A&A, 2003, 408: 1115-1135. DOI: 10.1051/0004-6361:20030604.

Khomenko E V, Shelyag S, Solanki S K, et al. Stokes diagnostics of simulations of magnetoconvection of mixed-polarity quiet-Sun regions [J/OL]. A&A, 2005, 442(3): 1059-1078. DOI: 10.1051/0004-6361:20052958.

Kiess C, Borrero J M, Schmidt W. Three-lobed near-infrared Stokes V profiles in the quiet Sun [J/OL]. A&A, 2018, 616: A109. DOI: 10.1051/0004-6361/201732267.

Kochukhov O. Doppler imaging of chemical spots on magnetic Ap/Bp stars. Numerical tests and assessment of systematic errors [J/OL]. A&A, 2017, 597: A58. DOI: 10.1051/0004-6361/201629768.

Kosugi T, Matsuzaki K, Sakao T, et al. The Hinode (Solar-B) Mission: An Overview [J/OL]. Sol. Phys., 2007, 243(1): 3-17. DOI: 10.1007/s11207-007-9014-6.

Landi Degl'Innocenti E. E., 1992 in solar observations: Techniques and interpretation, ed. f. sánchez, m. collados, & m. vázquez [M]. Cambridge: Cambridge University Press, 1992.

Landi Degl'Innocenti E, Landi Degl'Innocenti M. On the solution of the radiative transfer equations for polarized radiation [J/OL]. Sol. Phys., 1985, 97: 239-250. DOI: 10.1007/BF00165988.

Landi Degl'Innocenti E, Landolfi M. Polarization in Spectral Lines: volume 307 [M/OL]. Astrophysics and Space Science Library, 2004. DOI: 10.1007/978-1-4020-2415-3.

Leenaarts J, Pereira T, Uitenbroek H. Fast approximation of angle-dependent partial redistribution in moving atmospheres [J/OL]. A&A, 2012, 543: A109. DOI: 10.1051/0004-6361/201219394.

Leenaarts J, Pereira T M D, Carlsson M, et al. The Formation of IRIS Diagnostics. II. The Formation of the Mg II h&k Lines in the Solar Atmosphere [J/OL]. ApJ, 2013, 772(2): 90. DOI: 10.1088/0004-637X/772/2/90.

Lemoine B, Demuynck C, Destombes J L. Rydberg transitions of neutral magnesium in the infrared - Frequency measurements and Zeeman effect [J]. A&A, 1988, 191(1): L4-L6.

Li X, Song Y, Uitenbroek H, et al. Infrared diagnostics of the solar magnetic field with Mg I 12 μm lines: forward-model results [J/OL]. A&A, 2021, 646: A79. DOI: 10.1051/0004-6361/202039365.

Lites B W, Leka K D, Skumanich A, et al. Small-Scale Horizontal Magnetic Fields in the Solar Photosphere [J/OL]. ApJ, 1996, 460: 1019. DOI: 10.1086/177028.

Lites B W, Kubo M, Socas-Navarro H, et al. The Horizontal Magnetic Flux of the Quiet-Sun Internetwork as Observed with the Hinode Spectro-Polarimeter [J/OL]. ApJ, 2008, 672(2): 1237-1253. DOI: 10.1086/522922.

Lites B W, Akin D L, Card G, et al. The Hinode Spectro-Polarimeter [J/OL]. Sol. Phys., 2013, 283 (2): 579-599. DOI: 10.1007/s11207-012-0206-3.

Lites B W, Rempel M, Borrero J M, et al. Are Internetwork Magnetic Fields in the Solar Photosphere Horizontal or Vertical? [J/OL]. ApJ, 2017, 835(1): 14. DOI: 10.3847/1538-4357/835/1/14.

Lites B, Socas-Navarro H, Kubo M, et al. Hinode Observations of Horizontal Quiet Sun Magnetic Flux and the “Hidden Turbulent Magnetic Flux” [J/OL]. PASJ, 2007, 59: S571. DOI: 10.1093/pasj/59.sp3.S571.

Liu Z, Deng Y, Jin Z, et al. Introduction to the Chinese Giant Solar Telescope [C/OL]//Stepp L M, Gilmozzi R, Hall H J. Society of Photo-Optical Instrumentation Engineers (SPIE) Conference Series: volume 8444 Ground-based and Airborne Telescopes IV. 2012: 844405. DOI: 10.1117/12.926033.

Livingston W C, Harvey J. A New Component of Solar Magnetism - The Inner Network Fields [C]// Bulletin of the American Astronomical Society: volume 7. 1975: 346.

López Ariste A, Sainz Dalda A. Scales of the magnetic fields in the quiet Sun [J/OL]. A&A, 2012, 540: A66. DOI: 10.1051/0004-6361/201118191.

Martínez González M J, Bellot Rubio L R. Emergence of Small-scale Magnetic Loops Through the Quiet Solar Atmosphere [J/OL]. ApJ, 2009, 700(2): 1391-1403. DOI: 10.1088/0004-637X/700/2/1391.

Martínez González M J, Collados M, Ruiz Cobo B, et al. Low-lying magnetic loops in the solar internetwork [J/OL]. ApJ, 2007, 469(3): L39-L42. DOI: 10.1051/0004-6361:20077505.

Martínez González M J, Pastor Yabar A, Lagg A, et al. Inference of magnetic fields in the very quiet Sun [J/OL]. A&A, 2016, 596: A5. DOI: 10.1051/0004-6361/201628449.

Moran T, Deming D, Jennings D E, et al. Solar Magnetic Field Studies Using the 12 Micron Emission Lines. III. Simultaneous Measurements at 12 and 1.6 Microns [J/OL]. ApJ, 2000, 533(2): 1035-1042. DOI: 10.1086/308711.

Moran T G, Jennings D E, Deming L D, et al. Solar Magnetograms at 12 μm Using the Celeste Spectrograph [J/OL]. Sol. Phys., 2007, 241(2): 213-222. DOI: 10.1007/s11207-007-0271-1.

Murcray F J, Goldman A, Murcray F H, et al. Observation of new emission lines in the infrared solar spectrum near 12.33, 12.22, and 7.38 microns [J/OL]. ApJL, 1981, 247: L97-L99. DOI: 10.1086/183598.

Nordlund A. Numerical simulations of the solar granulation. I. Basic equations and methods. [J]. A&A, 1982, 107: 1-10.

Orozco Suárez D, Bellot Rubio L R. Analysis of Quiet-Sun Internetwork Magnetic Fields Based on Linear Polarization Signals [J/OL]. ApJ, 2012a, 751(1): 2. DOI: 10.1088/0004-637X/751/1/2.

Orozco Suárez D, Katsukawa Y. On the Distribution of Quiet-Sun Magnetic Fields at Different Heliocentric Angles [J/OL]. ApJ, 2012b, 746(2): 182. DOI: 10.1088/0004-637X/746/2/182.

Orozco Suárez D, Bellot Rubio L R, del Toro Iniesta J C, et al. Quiet-Sun Internetwork Magnetic Fields from the Inversion of Hinode Measurements [J/OL]. ApJL, 2007b, 670(1): L61-L64. DOI: 10.1086/524139.

Orozco Suárez D, Bellot Rubio L R, Del Toro Iniesta J C. Milne-Eddington inversion of the Fe I line pair at 630 nm [J/OL]. A&A, 2010, 518: A3. DOI: 10.1051/0004-6361/201014374.

Orozco Suárez D, Bellot Rubio L R, Del Toro Iniesta J C, et al. Strategy for the Inversion of Hinode Spectropolarimetric Measurements in the Quiet Sun [J/OL]. PASJ, 2007a, 59: S837. DOI: 10.1093/pasj/59.sp3.S837.

Pereira T M D, Uitenbroek H. RH 1.5D: a massively parallel code for multi-level radiative transfer with partial frequency redistribution and Zeeman polarisation [J/OL]. A&A, 2015, 574: A3. DOI: 10.1051/0004-6361/201424785.

Piskunov N, Valenti J A. Spectroscopy Made Easy: Evolution [J/OL]. A&A, 2017, 597: A16. DOI: 10.1051/0004-6361/201629124.

Press W H, Flannery B P, Teukolsky S A. Numerical recipes. The art of scientific computing [M]. Cambridge University Press, 1986.

Quintero Noda C, Shimizu T, de la Cruz Rodríguez J, et al. Spectropolarimetric capabilities of Ca II 8542 Å line [J/OL]. MNRAS, 2016, 459(3): 3363-3376. DOI: 10.1093/mnras/stw867.

Rachkovsky D N. Magnetic rotation effects in spectral lines [J]. Izvestiya Ordena Trudovogo Krasnogo Znameni Krymskoj Astrofizicheskoj Observatorii, 1962, 28: 259-270.

Rempel M. Numerical Simulations of Quiet Sun Magnetism: On the Contribution from a Small-scale Dynamo [J/OL]. ApJ, 2014, 789(2): 132. DOI: 10.1088/0004-637X/789/2/132.

Rimmele T R, Warner M, Keil S L, et al. The Daniel K. Inouye Solar Telescope - Observatory Overview [J/OL]. Sol. Phys., 2020, 295(12): 172. DOI: 10.1007/s11207-020-01736-7.

Ruiz Cobo B, del Toro Iniesta J C. Inversion of Stokes Profiles [J/OL]. ApJ, 1992, 398: 375. DOI: 10.1086/171862.

Ruiz Cobo B, del Toro Iniesta J C. On the sensitivity of Stokes profiles to physical quantities. [J]. A&A, 1994, 283: 129-143.

Ruiz Cobo B, Quintero Noda C, Gafeira R, et al. DeSIRe: Departure coefficient aided Stokes Inversion based on Response functions [J/OL]. A&A, 2022, 660: A37. DOI: 10.1051/0004-6361/202140877.

Sainz Dalda A, Martínez-Sykora J, Bellot Rubio L, et al. Study of Single-lobed Circular Polarization Profiles in the Quiet Sun [J/OL]. ApJ, 2012, 748(1): 38. DOI: 10.1088/0004-637X/748/1/38.

Sanchez Almeida J, Martinez Pillet V. The Inclination of Network Magnetic Fields [J/OL]. ApJ, 1994, 424: 1014. DOI: 10.1086/173952.

Sedik M, Bai X, Li W, et al. Forward modeling of the Mg I 12.32 μm line from a 3D magnetohydrodynamic model of an enhanced network [J/OL]. A&A, 2024, 686: A278. DOI: 10.1051/0004-6361/202449157.

Shchukina N, Trujillo Bueno J. Determining the Magnetization of the Quiet Sun Photosphere from the Hanle Effect and Surface Dynamo Simulations [J/OL]. ApJL, 2011, 731(1): L21. DOI: 10.1088/2041-8205/731/1/L21.

Sheeley J, N. R. Observations of Small-Scale Solar Magnetic Fields [J/OL]. Sol. Phys., 1967, 1(2): 171-179. DOI: 10.1007/BF00150852.

Shimizu T, Nagata S, Tsuneta S, et al. Image Stabilization System for Hinode (Solar-B) Solar Optical Telescope [J/OL]. Sol. Phys., 2008, 249(2): 221-232. DOI: 10.1007/s11207-007-9053-z.

Skartlien R. A Multigroup Method for Radiation with Scattering in Three-Dimensional Hydrodynamic Simulations [J/OL]. ApJ, 2000, 536(1): 465-480. DOI: 10.1086/308934.

Skumanich A, Lites B W. Stokes Profile Analysis and Vector Magnetic Fields. I. Inversion of Photospheric Lines [J/OL]. ApJ, 1987, 322: 473. DOI: 10.1086/165743.

Socas-Navarro H. Stokes Inversion Techniques: Recent Achievements and Future Horizons [C]// Sigwarth M. Astronomical Society of the Pacific Conference Series: volume 236 Advanced Solar Polarimetry – Theory, Observation, and Instrumentation. 2001: 487.

Socas-Navarro H, Sánchez Almeida J. Magnetic Properties of Photospheric Regions with Very Low Magnetic Flux [J/OL]. ApJ, 2002, 565(2): 1323-1334. DOI: 10.1086/324688.

Socas-Navarro H, Trujillo Bueno J. Linearization versus Preconditioning: Which Approach Is Best for Solving Multilevel Transfer Problems? [J/OL]. ApJ, 1997, 490(1): 383-392. DOI: 10.1086/304873.

Socas-Navarro H, Trujillo Bueno J, Ruiz Cobo B. Non-LTE Inversion of Stokes Profiles Induced by the Zeeman Effect [J/OL]. ApJ, 2000, 530(2): 977-993. DOI: 10.1086/308414.

Socas-Navarro H, de la Cruz Rodríguez J, Asensio Ramos A, et al. An open-source, massively parallel code for non-LTE synthesis and inversion of spectral lines and Zeeman-induced Stokes profiles [J/OL]. A&A, 2015, 577: A7. DOI: 10.1051/0004-6361/201424860.

Solanki S K, Keller C, Stenflo J O. Properties of solar magnetic fluxtubes from only two spectral lines [J]. A&A, 1987, 188(1): 183-197.

Stenflo J O. Magnetic-Field Structure of the Photospheric Network [J/OL]. Sol. Phys., 1973, 32(1): 41-63. DOI: 10.1007/BF00152728.

Stenflo J O. The Hanle Effect and the Diagnostics of Turbulent Magnetic Fields in the Solar Atmosphere [J/OL]. Sol. Phys., 1982, 80(2): 209-226. DOI: 10.1007/BF00147969.

Stenflo J O. Horizontal or vertical magnetic fields on the quiet Sun. Angular distributions and their height variations [J/OL]. A&A, 2013, 555: A132. DOI: 10.1051/0004-6361/201321608.

Suematsu Y, Tsuneta S, Ichimoto K, et al. The Solar Optical Telescope of Solar-B (Hinode): The Optical Telescope Assembly [J/OL]. Sol. Phys., 2008, 249(2): 197-220. DOI: 10.1007/s11207-008-9129-4.

Trujillo Bueno J, Shchukina N, Asensio Ramos A. A substantial amount of hidden magnetic energy in the quiet Sun [J/OL]. Nature, 2004, 430(6997): 326-329. DOI: 10.1038/nature02669.

Tsuneta S, Ichimoto K, Katsukawa Y, et al. The Solar Optical Telescope for the Hinode Mission: An Overview [J/OL]. Sol. Phys., 2008, 249(2): 167-196. DOI: 10.1007/s11207-008-9174-z.

Uitenbroek H. Multilevel Radiative Transfer with Partial Frequency Redistribution [J/OL]. ApJ, 2001, 557(1): 389-398. DOI: 10.1086/321659.

Unno W. Line Formation of a Normal Zeeman Triplet [J]. PASJ, 1956, 8: 108.

Viticchié B, Sánchez Almeida J. Asymmetries of the Stokes V profiles observed by HINODE SOT/SP in the quiet Sun [J/OL]. A&A, 2011, 530: A14. DOI: 10.1051/0004-6361/201016096.

Vögler A. [J]. PhD thesis, 2003, Georg-August-Universität: Göttingen.

Woeger F. The DKIST Instrumentation Suite [C]//AAS/Solar Physics Division Meeting: volume 47 AAS/Solar Physics Division Abstracts #47. 2016: 201.02.

Zeeman P. On the Influence of Magnetism on the Nature of the Light Emitted by a Substance. [J/OL]. ApJ, 1897, 5: 332. DOI: 10.1086/140355.

Zhao G, Butler K, Gehren T. Non-LTE analysis of neutral magnesium in the solar atmosphere [J]. A&A, 1998, 333: 219-230.

Zhou G, Wang J, Jin C. Solar Intranetwork Magnetic Elements: Flux Distributions [J/OL]. Sol. Phys., 2013, 283(2): 273-282. DOI: 10.1007/s11207-013-0229-4.

Zirin H, Popp B. Observations of the 12 Micron MG i Lines in Various Solar Features [J/OL]. ApJ, 1989, 340: 571. DOI: 10.1086/167418.

Zwaan C. Elements and patterns in the solar magnetic field. [J/OL]. Ann. Rev. Astron. Astrophys., 1987, 25: 83-111. DOI: 10.1146/annurev.aa.25.090187.000503.

Acknowledgments

Completing this doctoral thesis has been a journey filled with challenges, growth, and invaluable support from numerous individuals and institutions. I would like to take this opportunity to express my deepest gratitude to everyone who contributed to this work.

First and foremost, I would like to thank my supervisor, Yuanyong Deng, for his unwavering guidance, patience, and encouragement throughout this process. His expertise, insightful feedback, and dedication to my academic development have been instrumental in shaping this thesis. I am deeply grateful for the countless hours they spent discussing ideas, reviewing drafts, and helping me navigate the complexities of my research.

I am also immensely thankful to my co-supervisor, Xianyong Bai, for his invaluable contributions, constructive criticism, and support. His unique perspective and expertise greatly enriched my work and broadened my understanding of the field. My gratitude goes to my colleagues and fellow researchers at National Astronomical Observatories for creating a stimulating and collaborative environment. Special thanks to prof. Wenxian Li for her camaraderie, support, and countless discussions that inspired new ideas and solutions.

On a personal note, I owe an immeasurable debt of gratitude to my family and friends for their unconditional love, encouragement, and patience. To my parents, thank you for instilling in me the values of perseverance and curiosity. To my partner, thank you for standing by me through the highs and lows of this journey, offering unwavering support and understanding.

Resume and Academic Achievements during the Author's Degree Study

Resume:

- December 2013 to December 2016: M.Sc. in Mathematical Astronomy, Faculty of Science, Cairo University, Egypt.
- September 2012 to June 2013: Pre-master in Mathematical Astronomy, Faculty of Science, Cairo University, Egypt.
- September 2001 to May 2005: B.Sc. in Physics and Astronomy, Faculty of Science, Cairo University, Egypt.

Work experience:

- 2017 to present: Assistant Researcher at National Research Institute of Astronomy and Geophysics (NRIAG), Egypt.
- 2010 to 2016: Research technician at National Research Institute of Astronomy and Geophysics (NRIAG), Egypt.

Published academic papers:

(1)

Sedik M, Shaltout A M K, Deng Y, et al. Investigating the magnetic field of the quiet Sun internetwork [J/OL]. PASJ, 2023. DOI: 10.1093/pasj/psad067.

(2)

Sedik M, Bai X, Li W, et al. Forward modeling of the Mg I 12.32 μm line from a 3D magnetohydrodynamic model of an enhanced network [J/OL]. A&A, 2024, 686: A278. DOI: 10.1051/0004-6361/202449157.